UCGE Reports

Number 20358

Department of Geomatics Engineering

Ultra-tightly Coupled High Sensitivity GPS Receiver for On-Road Vehicle Applications

(URL: http://www.geomatics.ucalgary.ca/graduatetheses)

by

Tao Li

September, 2012

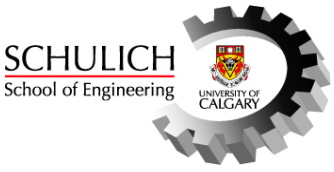

UNIVERSITY OF CALGARY

Ultra-Tightly Coupled High Sensitivity GPS Receiver for On-Road Vehicular Applications

by

Tao Li

A THESIS

SUBMITTED TO THE FACULTY OF GRADUATE STUDIES

IN PARTIAL FULFILMENT OF THE REQUIREMENTS FOR THE

DEGREE OF DOCTOR OF PHILOSOPHY

DEPARTMENT OF GEOMATICS ENGINEERING

CALGARY, ALBERTA

SEPTEMBER, 2012

ABSTRACT

For on-road vehicular navigation applications, High Sensitivity GPS (HSGPS) receivers are usually preferable to improve signal acquisition and tracking capabilities in comparison to conventional GPS receivers that suffer degraded performance or may completely fail to operate. Vehicle sensors can provide aiding information to bridge the gaps and thus improve the continuity and reliability of the navigation system. Therefore, this thesis focuses on ultra-tightly coupling of HSGPS receivers and vehicle sensors for improved navigation performance.

A block estimator based HSGPS receiver is developed with improved tracking sensitivity. The receiver uses a block of correlators for GPS signal parameter estimation and a vector based tracking strategy. Up to 100 ms coherent integration time is used in the receiver to improve the sensitivity with external data bit aiding. The performance of the receiver is analyzed in both the positioning and tracking domain, which provides the basis for the design of an innovative ultra-tightly coupled GPS receiver.

To integrate vehicle sensors, improved dead reckoning (DR) based integration algorithms are proposed in this research to provide better navigation performance. Vehicle sideslips, pitch and roll dynamics, usually ignored in previous research are also taken into consideration in this work. Field test results show that the accuracy of 2.4% of travelled distance can be obtained using the proposed algorithm. The performance of the integrated system with various sensor configurations is also analyzed in different environments. Furthermore, a novel DR based in-motion alignment algorithm is proposed to initialize low cost reduced Inertial Measurement Units (IMUs). The new in-motion alignment algorithm

features five-degree alignment accuracy within 20 seconds, without initial knowledge of the attitude.

Finally a new ultra-tightly coupled GPS receiver based on the block estimator and DR integration algorithms is proposed and developed. The performance of the receiver is comprehensively analyzed in different environments. The field test results shows that the receiver provides within a RMS positioning accuracy within five metres even in deep urban canyon environments, which meets the requirement for most vehicular navigation applications.

ACKNOWLEDGEMENTS

First of all, I would like to thank my supervisor, Dr. Gérard Lachapelle for his guidance, support and continuous encouragement during my studies. Further, I would like to express my gratitude to my co-supervisor, Dr. Mark Petovello. He lead me into the world of GNSS navigation. His knowledge and patient supervision helped me to finish my master degree.

The financial support of General Motors of Canada, the Natural Science and Engineering Research Council of Canada, Alberta Advanced Education and Technology and the Western Economic Diversification Canada is also acknowledged.

I am also grateful to those sensor research engineers Jared Bancroft, Vahid Dehghanian, and graduate students Tao Lin, Peng Xie, Da Wang, Ping Luo, Zhe He, Tiantong Ren, Boxiong Wang in the PLAN Group who helped with my field tests, shared discussions and answered my questions.

Finally, and most importantly, I would like to thank my parents and wife, for their unconditional love, encouragement and understanding through all of my years of study. This work would not have been possible without their support.

Table of Contents

LIST OF TABLES

LIST OF FIGURES

NOTATION

List of Acronyms

1A1G	One forward Accelerometer and One vertical Gyro
2A1G	Two horizontal Accelerometer and One vertical Gyro
2D	Two-Dimensional
3A1G	Three-axis Accelerometers and One vertical Gyro
3D	Three-Dimensional
ADC	Analog to Digital Converter
AGC	Automatic Gain Control
AGPS	Aided GPS
AMLE	Approximate Maximum Likelihood Estimator
BER	Bit Error Rate
C/A	Coarse / Acquisition
C/N_0	Carrier to Noise Density
C3NAVG2™	Combined Code and Carrier Phase for Navigation using GPS
CAN	Controller Area Network
CF	Compact Flash
CG	Center of Gravity
DAQ	Data Acquisition Device
DGPS	Differential GPS
DLL	Delay Lock Loop
DPLL	Digital Phase Lock Loop
DR	Dead Reckoning

EKF	Extended Kalman Filter
FLL	Frequency Lock Loop
GNSS	Global Navigation Satellite System
GPS	Global Positioning System
HSGPS	High Sensitivity Global Positioning System
IF	Intermediate Frequency
ILANA	Aided Inertial Land Navigation System
IMU	Inertial Measurement Unit
INS	Inertial Navigation System
LLF	Local Level Frame
LOS	Line-of-Sight
MEMS	Micro Electro-Mechanical Systems
NI	National Instruments
NCO	Numerically Controlled Oscillator
NLOS	Non Line-of-Sight
PLL	Phase Lock Loop
PRN	Pseudo Random Noise
RHCP	Right Hand Circularly Polarized
RF	Radio Frequency
RMS	Root Mean Square
RWSS	Rear Wheel Speed Sensor
SAS	Steering Angle Sensor
SNR	Signal to Noise Ratio

TTFF	Time TO First Fix
VDLL	Vector Delay Lock Loop
YRS	Yaw Rate Sensor
WSS	Wheel Speed Sensor

List of Symbols

$\delta\mathbf{r}^l$	Position error vector in the local level frame
$\delta\mathbf{v}^l$	Velocity error vector in the local level frame
ct	Receiver clock bias in metres
cdt	receiver clock drift in metres per second
λ_{L1}	L1 carrier wavelength
ψ_l	Left wheel angle
ψ_r	Right wheel angle
e	Half of the wheel track
ψ	Azimuth of the vehicle
$\dot{\psi}$	Yaw rate of the vehicle
V_{rl}	Rear left wheel speed
V_{rr}	Rear right wheel speed
V_{fl}	Front left wheel speed
V_{fr}	Front right wheel speed
V_y^b	Forward speed of the vehicle
R_a^b	Rotation matrix from a frame to b frame
R_1, R_2, R_3	Rotation matrixes about x ,y and z axis respectively
$\delta\psi$	Azimuth error of the vehicle
$\delta\theta$	Pitch error of the vehicle

δa_y^b	Forward acceleration error
$\hat{X}$	Estimated value of X
$\mathbf{H}_{RWSS}$	Design matrix of the rear WSS measurement updates
$\mathbf{R}_{RWSS}$	Measurement noise matrix of RWSS
d_{YRS}	Yaw rate sensor drift
$\tilde{\omega}_{ibz}^b$	Measurements of YRS
$\mathbf{H}_{YRS}$	Design matrix of the YRS measurement updates
$\mathbf{R}_{YRS}$	Measurement noise matrix of YRS
$\lvert g \rvert$	Magnitude of the local gravity in the local level frame
b_y	Longitudinal accelerometer bias
θ_{pseudo}	Pseudo pitch measurements
$\mathbf{H}_\theta$	Design matrix of the pseudo pitch update
$\mathbf{H}_{FWSS}$	Design matrix for the front WSS measurement updates
$\mathbf{R}_{FWSS}$	Measurement noise matrix of front WSS
δa_x^b	Later acceleration error of the vehicle
b_x	Later accelerometer bias
ϕ_{pseudo}	Pseudo roll measurements
$\mathbf{H}_\phi$	Design matrix of the pseudo roll update
S_{WSS}	Scale factors of WSS
M	Meridian radius of the earth curvature

N	Prime vertical radius of the earth curvature
$\boldsymbol{\Omega}_{bc}^{a}$	Skew-symmetric matrix, which indicates the rotation rate of frame ‘c’, relative to frame ‘b’, expressed in frame ‘a’.

CHAPTER ONE: INTRODUCTION

Modern land vehicle navigation systems are often equipped with Global Positioning System (GPS) receivers and vehicle sensors to provide position, velocity and attitude information. For on-road vehicular navigation applications, High Sensitivity GPS (HSGPS) receivers are usually preferred for improved acquisition and tracking capabilities in comparison to conventional GPS receivers in degraded signal environments. However, in urban canyon or dense foliage areas where the signals are severely attenuated, jammed, reflected or completely blocked, even current HSGPS receivers would suffer degraded performance or may completely fail to operate (Kazemi 2010). Vehicle sensors, in this case would provide aiding information to bridge the gaps and thus improve the reliability of the navigation system (Li 2009).

A typical modern vehicle sensor setup is likely to include inertial sensors, Wheel Speed Sensors (WSS) and a Steering Angle Sensor (SAS). Due to the cost-sensitive nature of on-road vehicular navigation applications, the inertial sensors used inside vehicles often consist of reduced order low-cost Micro Electro-Mechanical Systems (MEMS) based Inertial Measurement Units (IMUs) instead of full six degree of freedom IMUs. A reduced IMU often includes two horizontal accelerometers and one vertical gyroscope (2A1G), or three accelerometers and one vertical gyroscope (3A1G). The integration of GPS and vehicle sensors has been shown to provide more accurate positioning information and higher reliability compared to stand alone GPS or vehicle sensor-based Dead Reckoning (DR) navigation system (Li et al 2009, Li 2009, Gao 2007, Niu et al 2007a).

The integration algorithms vary with different vehicle sensor configurations and different navigation purposes. The integration strategies also evolve from loose, tight to ultra-tight or deep integration. Compared with loose and tight integration, ultra-tight integration provides improved signal tracking capabilities and higher navigation performance under weak signals, high vehicle dynamics and signal jamming conditions (Abbott & Lillo 2003, Kim et al 2003, Jovancevic et al 2004, Soloviev et al 2004a & 2004b, Landis et al 2006, Ohlmeyer 2006, Pany et al 2005, Kiesel et al 2007, Petovello et al 2006 & 2008b).

This dissertation is focused on the design and implementation of an advanced on-road vehicular navigation system using ultra-tightly coupled GPS and vehicle sensor integration. The thesis expands on previous research on ultra-tight integration by improving the GPS receiver with a high sensitivity capability. Furthermore, new integration algorithms using the DR approach instead of the more traditional Inertial Navigation System (INS) mechanizations for the GPS and vehicle sensor fusion is proposed and verified to improve navigation performance and system reliability. Finally, the performance of the novel on-road vehicle navigation system is evaluated under various operational environments, especially those previously regarded as GPS denied areas.

1.1 Background

A modern on-road vehicular navigation system usually utilizes a GPS receiver and vehicle sensors to form an integrated navigation system. Therefore the performance of the system mainly depends on three aspects, namely: 1) the performance of the GPS receiver; 2) the vehicle sensor configurations and the sensor quality and 3) the integration algorithm. The

following sections outline the three aspects that characterize the integrated navigation system.

1.1.1 GPS Receiver

As stated above, HSGPS receivers provide improved acquisition and tracking sensitivity compared to conventional GPS receivers, which make HSGPS receivers the most appropriate for meeting the requirements of land vehicle navigation. Therefore, HSGPS is the major focus of the thesis instead of survey grade high precision receivers. This section reviews the major techniques used in HSGPS receivers.

Depending on the environment, the received GPS signals can undergo attenuations in excess of 20 dB from nominal open sky conditions (MacGougan 2003). Accordingly, substantial signal processing gain is required to compensate for the massive signal attenuation to allow for successful GPS signal acquisition (Shanmugam 2008). HSGPS receivers utilize large banks of correlators and digital signal processing for enhanced signal detection under adverse conditions. The use of parallel correlation techniques significantly reduces acquisition time resulting in faster times to first fix (TTFF) under nominal signal power levels. Under weak signal conditions, the extra signal processing power is utilized to apply long coherent or noncoherent integration to detect the signals (Shanmugam 2008). Several detection algorithms have been described in the literature to address the problem of high sensitivity acquisition. These detection schemes can be broadly categorized under coherent, noncoherent, differential detection or combinations of the three (Borio 2008, Shanmugam 2008, Gernot 2011).

When used in degraded signals environments, high sensitivity tracking is also required to continuously track the carrier frequency and code offset and to generate pseudorange and Doppler measurements for computing a user's position and velocity. To improve tracking performance, there are mainly three methods, namely extending the integration time, improving the tracking loop performance and utilizing aiding sensor information.

Extending the coherent integration time is the most beneficial way to improve the signal to noise ratio (SNR). Unfortunately, the maximum coherent integration time in a GPS receiver can be limited by a variety of factors. For instance, the presence of navigation data modulation typically limits the coherent integration time to less than 20 ms for L1 CA code. Navigation bit estimation algorithms can be used to predict and remove the data bits for long coherent integration (Kazemi 2010). However, the performance of these algorithms is limited by the high Bit Error Rate (BER) in weak signal environments. Assisted GPS (AGPS) can be used to solve this problem by sending those navigation bits via wireless links. Another factor that limits the coherent integration time is the stability issue of the Phase Locked Loop (PLL), which requires that the maximum achievable bandwidth multiplied by integration time for a stable loop is limited to 0.4 for rate-only feedback NCOs (Stephens & Thomas 1995). A redesigned Digital PLL (DPLL) proposed by Kazemi (2010) can be used to solve the stability problem. An alternative is to apply an open loop structure or batch processing, which removes the stability issue of a closed loop and improves the signal observability (van Graas et al 2005, Lin et al 2011a). However, the computation load is much higher than that of a conventional closed loop structure.

Noncoherent integration is commonly used for acquiring weak signals. Unlike coherent integration, the noncoherent approach relies on short coherent integration followed by a large number of noncoherent summations. Noncoherent processing applies a nonlinear transformation to the input signal, removing the effects of data transitions and reducing the impact of frequency errors (Ward et al 2006). This nonlinear transformation generally amplifies the noise impact, incurring the so-called squaring loss. Recent work from Borio (2009) applied noncoherent integration for weak signal tracking resulting in the sensitivity around 14 dB-Hz.

A Kalman filter can be used to replace the discriminator and loop filter for the carrier and/or code loop in a GNSS receiver. Instead of weighting all the measurements (from the discriminator) equally, a Kalman filter could vary its gain based on the changing measurement noise statistics and process noise statistics. The measurement noise statistics vary with SNR levels whereas the process noise statistics vary with user dynamics. Improved tracking sensitivity with Kalman filter based tracking has been shown in Petovello et al (2006), Humphreys et al (2005), Ziedan & Carrison (2004), Psiaki & Jung (2002), Psiaki (2001).

The vector based tracking loop which combines the tracking of the different satellite code and carrier signals into a single extended Kalman filter was originally introduced in Spilker (1996). In a vector based tracking loop, the individual tracking loops are eliminated and are replaced by the navigation filter. With the position and velocity of the receiver known, the feedback to the local Numerically Controlled Oscillator (NCO) is obtained from the

computed range and range rate to each satellite. It offers better tracking ability in weak signal or jamming environments because noise is reduced in all channels and information from strong signals can be potentially helpful for weaker signal tracking. In fact, extensive research has been performed to investigate these benefits, see for example Lashley (2006), Lashley & Bevly (2009 & 2006), Pany & Eissfeller (2006), Pany et al (2009), Lin et al (2011a & 2011b) and Soloviev & Dickman (2011).

Recently, the block processing structure has shown excellent potential for the high sensitivity GNSS field. It allows for longer integration time up to several seconds without stability issues in a conventional closed loop structure (van Graas et al 2005, Lin et al 2011a & 2011b). It also provides improved signal observability and tracking robustness. This is because a block processor computes the estimates of signal parameters based on a block of correlator outputs, which contrasts with the traditional loop filter based approach using only three correlators. In addition, the block estimator does not have to follow the user dynamics within the bandwidth of a loop filter thus offering better performance in high dynamic environments. Although the block processing structure results in a higher computation expense, its structure is suitable for parallel processing. A 15 dB-Hz tracking sensitivity was reported in recent work using open loop tracking strategy (Soloviev et al 2007).

A sensor aided GPS receiver not only provides better positioning performance, but also improves the tracking sensitivity. Extensive work has been done on INS aided tracking loop (Sun et al 2010, Gebre-Egziabher et al 2005, Alban et al 2003, Chiou 2005). The user's dynamic information provided by the INS can be used to reduce the tracking loop's

bandwidth, thus improving tracking capability. Furthermore, an ultra-tight or deep integration of GPS and INS which is based on the vector tracking loop, uses the INS derived range and range rate measurements to control the NCO between GPS measurement updates. It further improves the tracking sensitivity compared to vector tracking without INS (Petovello et al 2006 & 2008b, Soloviev & Dickman 2010, Lin et al 2011a).

1.1.2 Vehicle Sensors

Vehicle sensors are now standard devices in most modern vehicles, and are usually integrated with a central control unit to improve the safety and operational stability of vehicles. A typical vehicle sensor setup is likely to include wheel speed sensors, inertial sensors and steering angle sensors.

Wheel speed sensors are located at each of the wheels of the vehicle to provide wheel rotation velocity. For details of operational principles of wheel speed sensors refer to Gillespie & Thomas (1992), Carlson (2003), Gao (2007), Li et al (2010). Wheel speed sensors offer a flexible, small and low cost solution to measure vehicle's speed. However, high accuracy wheel speed outputs can be only obtained when the vehicle is running at a relatively high speed (e.g. above 5 km/h). Thus it is important to properly characterize the measurement noise of wheel speed sensors for sensor integration. Gao (2007) employed a high accuracy GPS receiver to calibrate a wheel speed sensor with the vehicle running at low (20 km/h), medium (50 km/h) and high (80 km/h) constant speeds on a flat road. Kubo et al (1999) also used velocity from a GPS receiver to calibrate the scale-factor of wheel speed sensors.

Inertial sensors offer angular velocity and acceleration information. The on-vehicle inertial sensors often use reduced MEMS IMUs to reduce the cost of the system. Two horizontal accelerometers and one vertical gyroscope (2A1G) and three accelerometers and one vertical gyroscope (3A1G) are the most commonly used sensor configurations. Niu (2007b) and Sun (2008) analyzed the effect of the omitted sensor on the performance of the integrated navigation solution.

The steering angle sensor located on the front wheel axis is used to measure the front tire turning angle with respect to the neutral position (Gillespie & Thomas 1992, Wong 1993). Gao (2007) applied steering angle measurements as external heading updates to the integrated Kalman filter to improve the positioning performance. Sasse et al (2009) included a steering angle sensor for their 2D autonomous vehicle navigation system.

The outputs of vehicle sensors are connected to the central control unit by a Controller–area network bus (CAN-bus) which is a vehicle bus standard designed to allow microcontrollers and devices to communicate with each other within a vehicle without a host computer. With increasing demand for vehicle navigation applications, these vehicle sensors originally designed for vehicle safety can be integrated with GPS to provide more accurate and reliable navigation solutions (Gao 2007, Li et al 2009 & 2010).

1.1.3 Integration Algorithms of Vehicle Sensors

Different algorithms have been proposed by previous researchers for various vehicle sensor configurations and for various navigation purposes (e.g. 2D or 3D). These algorithms can

be approximately classified into two categories, namely the traditional INS mechanizations, and dead reckoning based approaches. The former approach integrates accelerations sensed by accelerometers to obtain the velocities. The velocities are then integrated to obtain the position increments. Therefore, the accuracy of this approach tends to degrade with time (Jekeli 2000). Unlike the INS mechanization based approach, DR algorithms directly make use of wheel speed sensors' information to obtain the vehicle's velocity. Thus, the accuracy of this approach degrades with the travelled distance.

Because of the vehicles' reduced INS sensor configurations, the traditional INS mechanization approach has several variations. Phuyal (2004), who made use of a single gyroscope aligned vertically to measure azimuth rate and an accelerometer to measure vehicle forward linear motion, derived simplified 2D navigation equations. Simulation results were employed to evaluate the errors in position from ignoring the small quantities in navigation equations.

Brandit & Gardner (1998) used non-holonomic constraints on the motion of the land vehicles to derive a set of navigation equations for reduced inertial sensors (3A1G). Non-holonomic constraints use assumptions that the vehicle operates on a flat road and without side slip (Dissanayake et al 2001). In addition, a wheel speed sensor was used to provide auxiliary information about the vehicle's speed. A second accelerometer was also used to provide redundant data that helps to reduce overall system error.

Niu et al (2007b) implemented the pseudo-signal approach for reduced IMU/GPS navigation systems. The main concept of the reduced IMU approach is to replace the unavailable signals by pseudo signals that have constant values plus white noise. Since land vehicles mainly run on relatively flat roads with inclinations typically less than 5 degrees, the output of the vertical accelerometer is composed mainly of the local gravity plus the addition of road vibrations. Similar analysis can be applied to the two horizontal gyros. Then these pseudo signals were fed into the conventional GPS/INS navigation algorithm to obtain the final navigation solution. In his work, non-holonomic constraints were applied with the wheel speed sensor derived velocity to form 3D velocity updates to the navigation filter. Apparent improvement of velocity and attitude accuracy can be obtained when using 3D velocity updates in MEMS based integrated system.

Sun et al (2008) proposed a terrain predictor for reduced IMU integration. The terrain predictor models the pitch and roll induced by the road as a first order Gauss-Markov process. It improved the attitude estimates compared with the pseudo signal approach proposed by Niu et al (2007b).

DR based algorithms have also been widely used for navigation and vary with different sensor configurations. The most commonly used vehicle sensor configuration includes one vertical gyroscope to measure the yaw rate and an odometer or a wheel speed sensor to measure the travelled distance. Umar et al (2008 & 2009), Kazuyuki et al (1994), applied such sensor configuration and used similar DR algorithms in their work. Such form of DR algorithms offers the simplest navigation equations and thus have the lowest computational

load. However, with the exception of the gyroscope, no additional information of the yaw rate is available for this sensor configuration, and the heading error accumulates rapidly without GPS updates for these algorithms.

When two odometers or wheel speed sensors (left and right wheels) are available, the differential odometry or wheel speeds can be used to obtain the yaw rate information. Niedermeier et al (2010), Carlson et al (2003), Stephen & Lachapelle (2001) and Lahrech et al (2004) applied differential odometry or wheel speeds in their work to improve the heading estimates without GPS updates. However, because of the large uncertainty of the front wheel steering angles, the differential odometry and wheel speeds are limited to the rear wheels.

In order to utilize the front wheel speed sensors' information for the velocity and yaw rate estimation, the steering angle sensor should be used. Bonnifait et al (2001) used the steering angle measurements to calculate the front left and right wheel steering angles respectively and separate the forward speeds for each of the front wheels. Therefore, all the four wheel speed sensor measurements can be used to update the navigation equation. Furthermore, the yaw dynamics can be also inferred from the steering angle. Bevly & Parkinson (2007) discussed the use of two cascaded estimators to accurately estimate all the states necessary for accurate dead-reckoning navigation. However, the above mentioned DR algorithms assume that vehicles are running on flat and level roads. Thus, the pitch and roll of the vehicle are neglected according to this assumption and ultimately limit the navigation performance.

Since the pitch and roll dynamics of the vehicle cannot be always safely neglected such as when the vehicle operates on an uneven road or goes up and down hills, the pitch and roll should be taken into consideration. Given the road grade angles have larger variations than the road bank angles, Somieski et al (2010) included the pitch in the system states modeled as a random constant; Sasse et al (2009) modeled the pitch as first order Gauss-Markov process. Using these models, the pitch can be estimated within certain accuracy when GPS measurements are available and better positioning performance can be obtained compared with the cases without the pitch compensation. However, during GPS outages, the pitch state is not observable and thus there is no performance improvement in these conditions.

When horizontal accelerometers are included in the sensor configuration, the pitch and roll estimates can be obtained even without GPS updates. Daum (1994) used one gyroscope and two horizontal accelerometers together with an odometer in their Aided Inertial Land Navigation System (ILANA). Unlike the INS mechanization approach, the accelerometers in this system were used to establish a level plane (i.e., to measure pitch and roll angles), rather than to measure the vehicle acceleration. However, such a sensor arrangement is sensitive to accelerations experienced by the vehicle, yielding large pitch and roll angle errors. Similarly, Bevly (2004) discussed the accuracy of pitch and roll estimates without pitch and roll gyros in his DR algorithm. Furthermore, Fuke (1996) and Tseng (2007) applied wheel speeds derived vehicle longitudinal acceleration to compensate the longitudinal vehicle dynamics sensed by the longitudinal accelerometer and thus improved the pitch estimates.

An alternative DR based vehicle navigation system applies vehicle dynamic models to obtain the key vehicle states including velocity, attitude, sideslip, etc. Compared with above mentioned algorithms which are mostly based on kinematic models, the performance of the vehicle dynamic model based DR system relies highly on the accuracy of the vehicle parameters including weight, moment of inertia, tire stiffness, etc. (Bevly et al 2000 & 2001). Travis & Bevly (2005) discussed the navigation errors induced by the vehicle parameter errors in this type of system. Anderson et al (2004) compared the performance of model based estimator and kinematic based model for the side slip estimation. Simulation results shows that model based estimators show better performance over kinematic Kalman filter based estimators even with 2% scale factor error of gyroscopes.

In terms of integration strategy, the same concept as GPS/INS integration can be adopted for DR-based systems. Therefore, GPS and vehicle integration can be also divided into loosely coupled, tightly coupled and ultra-tight or deeply coupled integration. Most of the works on GPS and vehicle sensor integration apply the loose or tight integration strategy; however, recent work by Li et al (2010) shows improved performance was obtained by ultra-tight integration in degraded signal environments.

1.2 Limitations of Previous Research

Studies involving weak signal tracking have been conducted during the last few years. However, most of the current research has been mainly concentrated on the closed loop architecture. Psiaki (2001), Psiaki & Jung (2002) and Zeidan & Garrison (2004) implemented an extended Kalman filter specially designed for tracking carrier phase in

weak signal environment. In their work, a tracking threshold of 15 dB-Hz under static conditions using an OCXO oscillator is claimed. However, these results remained at the simulation level. The performance of EKF based carrier phase tracking is discussed in Petovello et al (2008b) for real GPS signal under weak signal conditions where a 20 dB attenuation was reported. As that work shows, there are still severe limitations in tracking GPS signals especially for C/N_0 values less than 24 dB-Hz.

Extending coherent integration time has been the most efficient way to improve tracking sensitivity. However, the stability of loop filter and the narrow linear region limits the use of longer coherent integration time for a conventional loop. Recent work by Petovello et al (2008a) shows that there might be performance degradation for higher integration times for EKF based tracking. Kazemi (2009) investigated the stability problem of conventional PLL with long integration time and proposed an optimum DPLL for weak carrier phase tracking. O'Driscoll et al (2010) analyzed the trade-off between tracking sensitivity and loop update rate with integration times longer than 20 ms by investigating the use of Kalman filter based tracking loops. A method to determine an optimum integration time for a given application was given in their work. However, their work requires phase lock for carrier frequency tracking which is not always feasible with weak signals. Besides, carrier phase measurements are not always of interest, especially for cost sensitive land vehicle navigation applications, where the pseudorange and pseudorange rate measurements are often sufficient for positioning. Thus FLL or Kalman filter based FLL may be used in weak signal tracking which offers a few dB sensitivity improvement over PLL.

INS aided tracking loops have been proposed and fully investigated to improve the tracking performance under dynamic environments by reducing the tracking loop bandwidth. Also, ultra-tight integration with vector based tracking loops have been proposed and implemented to improve both tracking and navigation performance in degraded signal environments (Brown et al 2005, Badu & Wang 2006, Petovello et al 2006, Soloviev et al 2007, Li & Wang 2006, Petovello et al 2008). However, the integration time in these implementations was still less than 20 ms, which limited the tracking performance in extreme weak signal environment. The feasibility of using longer integration time for ultra-tight integration, especially with low cost MEMS IMU still needs research.

Recently, the open loop structure for carrier frequency and code phase estimation shows great potential for HSGPS receiver design. The open loop structure is immune to the stability problem encountered with long integration times. Tracking robustness can be also obtained with improved observability in an open loop structure. Van Graas et al (2005) first proposed batch and sequential combined deep integration structure, which employed over 1 second integration time with an open loop technique. However, a complete open loop structure requires high computational capability. Reducing the search uncertainty and determining the search area reliably according to the signal environments and vehicle dynamics is of importance and need to be investigated. Furthermore, the use of vehicle sensors to aid open loop tracking has not been researched yet.

Vector based navigation feedback can be also applied in the open loop tracking (Lin et al 2010 & 2011). The advantages of using navigation solution feedback to determine the

center of the search space for each channel instead of using the estimates from the local block processing estimator are the following: 1) signal parameter uncertainty space can be reduced by using the more accurate signal estimates derived from the position information in a globally optimum sense to setup the center point of the search space; and 2) the uncertainty space can be tuned based on the estimated positioning accuracy. However, a large error in the navigation solution may influence the determination of the center point of the search space for every channel. In the worst case, the navigation solution derived signal parameters are completely biased and thus the true signal values are out of range of the search space. Therefore, determining the search space in this situation still requires further investigation.

Another problem with the block-processing strategy is that both line of sight (LOS) and non-LOS (NLOS) signals may appear as peaks in the correlator grid. This has been observed by Ward et al (2006), Soloviev (2007), Xie & Petovello et al (2010). Some work has been done upon the characterization of multipath (Xie & Petovello 2010). Therefore, how to identify the incorrect peaks and to avoid using measurements induced by these peaks requires further consideration.

In terms of GPS and vehicle sensor integration, extensive works have been conducted with either traditional INS mechanizations or DR based approaches (Phuyal 2004, Brandit & Gardner 1998, Niu et al 2007b, Sun et al 2008, Bevly et al 2000 & 2001). However, previous works on DR solutions normally ignore the pitch and roll information, which would correspondingly degrade the system performance especially on uneven road

conditions. Therefore, taking the pitch and roll into consideration is of importance to obtain improved navigation performance. Furthermore, most previous research applied the loose or tight integration strategy. Li et al (2009 & 2011) employed ultra-tight integration of GPS and vehicle sensors with traditional INS mechanizations. However, given that DR degrades with distance instead of time, it is preferable to utilize DR algorithms for the ultra-tight integration to enhance the system stability. To the best of the author's knowledge, an investigation of applying DR algorithms for ultra-tight integration of GPS and vehicle sensors has not been fully studied.

Furthermore, when using wheel speed sensors, most of the previous research did not consider the vehicle slip angles which are the angles between velocity at the center of gravity of the vehicle and the wheel directions (Li et al 2010 & 2009, Niu et al 2007b, Gao 2007). Ignoring the slip angles would result in performance degradation of the integrated system. Besides, the violation of non-holonomic constraints induced by vehicle side slip during specific vehicle dynamics would also affect navigation performance. Thus how to identify vehicle side slips is important to maintain the system's reliability. Finally, in a multi-senor integrated system, sensor failures would cause fatal problems which would severely influence the system performance. Therefore, using redundant multi-sensor information to detect and isolate sensor failures is still worthy of investigation.

Finally, previous works on the DR solutions require relatively accurate initial heading information. Because of the low cost MEMS gyros used in this work, which do not meet the requirement of the static alignment, they can be only aligned in-motion with the GPS

information. However, previous work on in-motion alignment of INS is mainly focused on the full IMU configuration (Rogers 2007). The alignment of reduced MEMS IMU has not been fully investigated. Furthermore, when using DR based navigation equations, the error models are different from the conventional mechanization-based INS. Thus modification of the conventional in-motion alignment algorithms should be made for the DR based system. To the best of the author's knowledge, no work has been conducted upon the DR based in-motion alignment.

1.3 Objectives and Contributions

The main objective of the research is to develop a high sensitivity GPS receiver for land vehicular applications. The proposed receiver will use the block processing strategy and multiple sensor fusion techniques to improve the ultra-tightly coupled GPS and vehicle sensor integrated system. The expected position accuracy is within five metres and the velocity accuracy is within several decimeters per second. In order to fulfill the goal, the specific objectives are as follows:

1. *To implement and analyze the performance of a block processing-based HSGPS receiver*. In order to improve the sensitivity, the longer integration time over 20 ms is applied with additional bit adding information. Given the stability issues of the traditional closed loop tracking, the open loop tracking strategy is designed with a block of correlators. Since the outputs of the block estimators are usually noisier, Vector-based navigation feedback will be also applied to provide globally optimum filtered signal parameter estimates to control the NCO. The navigation performance as the function of the search uncertainty will be analyzed to help to determine the optimum search space in different environments. Finally,

the performance of the open loop tracking will be analyzed in both tracking and navigation domain under different operational environments and will be compared to a standard tracking loop.

2. *To improve the design of a DR based navigation system and analyze its performance.* With the commonly used vehicle sensors, namely four wheel speed sensors, a steering angle sensor and a reduced IMU inside modern vehicles, proper navigation equations will be derived from an INS mechanization and dead reckoning point of view. However, focus is given to DR algorithms in this thesis. For the DR based system, the kinematic model based navigation equations will be derived. A novel DR algorithm using all the vehicle sensor information with the compensation of the pitch and roll will be designed and implemented. The performance of the DR algorithms with different sensor setups will be analyzed to determine the best sensor setup for the land vehicular applications. Furthermore, the position, velocity and attitude accuracy will be used for navigation performance analysis.

3 *To design and implement the in-motion alignment algorithm with the DR system.* The DR based vehicle sensor system also requires the initial attitude information for the positioning process. Because of the low cost MEMS gyro used in this work, the static alignment cannot be used to obtain the initial heading information. Thus, a new in-motion alignment algorithm will be proposed and tested. The algorithm employs the large heading uncertainty model, thus it does not require any information about the initial heading during the alignment procedure.

4. *To integrate vehicle sensors for ultra-tightly coupled HSGPS receiver*. Given the findings in Task 2 and 3, the proper DR based algorithms will be used for the ultra-tight integration. The navigation feedback from the integrated GPS/DR system will be applied to the HSGPS receiver. In order to evaluate the overall system performance, both the tracking and navigation performance analysis will be conducted. The estimated C/N_0 and frequency tracking error will be used for tracking performance analysis and the position, velocity and attitude accuracy will be used for navigation performance analysis. The performance will also be compared between different sensor configurations.

All the algorithms proposed in this thesis are implemented in C/C++ software. The proposed ultra-tightly coupled GPS/vehicle sensor integrated receiver is based on the GNSS Software Navigation Receiver (GSNRx^{TM}) developed by the Position, Location and Navigation (PLAN) group (Petovello et al 2009). The high sensitivity version of GSNRx^{TM} is used as the basis for the work presented herein. The interfaces were implemented for sensor data collection and real-time processing. The DR based integration algorithms with various sensor configurations are implemented as a library to enhance navigation and tracking performance of GSNRx-hs^{TM}. Furthermore, the loose and tight integration solution of GPS and vehicle sensors (GSNRx-nav-dr^{TM}) are also implemented for performance comparison purposes. Over 3000 C/C++ lines of codes were implemented and extensively tested during the research.

1.4 Thesis Outline

Chapter 2 provides an overview of channel processing strategies. The block processing strategy is presented and compared with scalar and Kalman filter tracking strategies. The concept of the block correlators is described and the discussion of the pros and cons of the processing technique is included. After that, the vector based receiver architecture is introduced. Finally, the details of the HSGPS receiver used in the dissertation based on the block processing strategy and the vector based feedback is presented.

Chapter 3 provides the algorithm derivation of the DR based GPS/vehicle sensor integrated system with different sensor configurations. Both the system models and measurement models of the integrated system are presented in this chapter. For comparison purposes, two INS mechanization based algorithms namely the pseudo-signal and the local terrain predictor methods are also briefly introduced. Finally, field test results using different sensor setups, with different integration strategies and in various environments are used to analyze the navigation performance of the proposed system.

Chapter 4 describes the DR based in-motion alignment algorithm with the large initial heading uncertainty assumption. For comparison purposes, the in-motion alignment algorithm using a pseudo-signal approach is also presented. Finally, the algorithms are verified with field test data. The convergence time of the azimuth with different initial heading errors is analyzed.

Chapter 5 contains a description of the ultra-tightly coupled GPS/vehicle sensor receiver. Both the conventional and the HS block correlator based ultra-tight receiver architecture are described and compared. Their pros and cons are also discussed in this chapter. Finally, the proposed system is verified using field test data. The performance of the system is evaluated under different test scenarios.

Chapter 6 summarizes the work presented in this thesis, and draws conclusions from the test results and analysis. Several recommendations for future work are also presented.

CHAPTER TWO: HIGH SENSITIVITY BLOCK PROCESSING GPS RECEIVER

As mentioned in Section 1.1.1, GNSS signals in harsh environments such as dense foliage and urban canyon areas can experience 10 dB to 30 dB attenuation. In addition to the attenuation of signal strength, the multipath fading effect results in time varying signal power and degrades the code delay and Doppler estimation. Traditional GPS receivers usually lack the ability to maintain tracking under these conditions. Thus high sensitivity block processing using longer coherent integration time is introduced in this chapter.

In particular, this chapter gives the introduction of the block processing technique for high sensitivity receivers. The chapter starts with an overview of channel processing strategies. The block processing technique is introduced and compared with scalar and Kalman filter tracking strategies. The concept of block correlators is described and a discussion of the pros and cons of the processing technique is included. The proposed high sensitivity receiver architecture in this chapter forms the basis of the ultra-tightly coupled GPS and vehicle sensor integrated receiver.

2.1 General GPS Receiver Architecture

Before introducing the high sensitivity block processing GPS receiver architecture, the general review of the GPS receiver architecture is presented first. In general, GPS receiver architectures can be categorized into scalar-based receivers and vector-based receivers. Detailed introduction and discussion of the two receiver architectures are presented in this section.

2.1.1 Standard GPS Receiver Architecture

A high-level block diagram of a modern standard software based GPS receiver is shown in Figure 2.1. The GPS Radio Frequency (RF) signals of all satellites in view are received by a Right Hand Circular Polarization (RHCP) antenna with nearly a hemispherical (i.e., above the local horizon) gain pattern. In the front-end portion shown in the upper block of Figure 2.1, the RF signals are prefiltered, amplified and down-converted to Intermediate Frequency (IF) signals. At the end of the front-end block, IF signals are sampled by the Analog to Digital (A/D) converter into digital IF signals (Kaplan 1996, Van Dierendonck 1996).

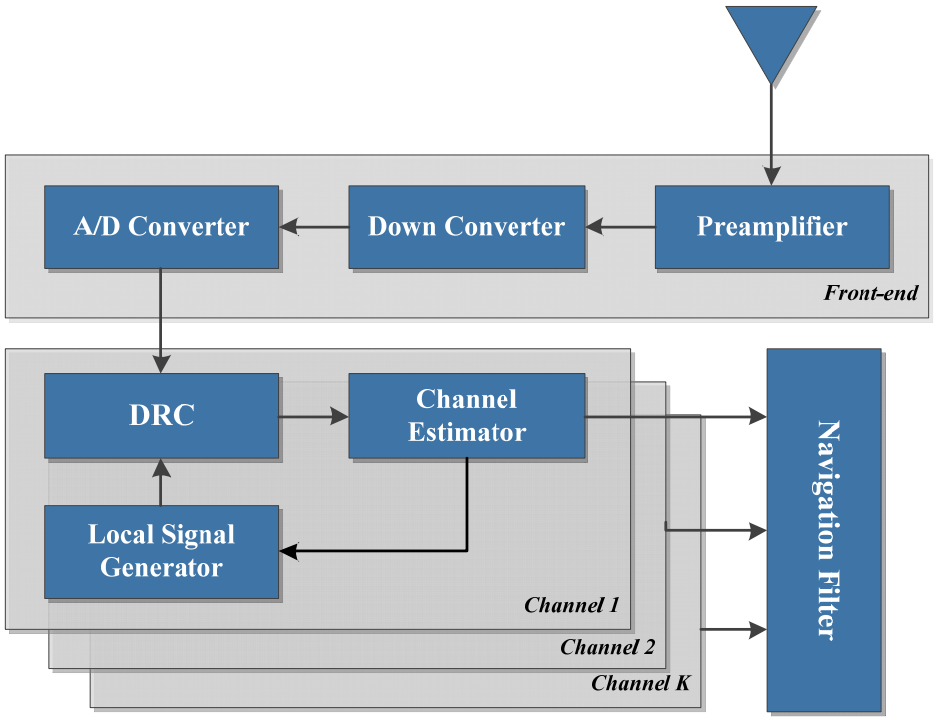

Figure 2.1: Standard GPS receiver

The IF samples are then passed to a signal processing function where Doppler removal and Correlation (DRC) are performed. After that, the correlator outputs are fed to channel

estimators which determine the difference between the incoming IF signals and the local generated signals. The channel estimator can be either the discriminator/ loop filter based estimator, Kalman filter or the block correlator based estimator. Finally, the local signal generators, whose output is used during Doppler removal and correlation are updated. Thus the standard receiver is characterized by the channel estimator feedback. As necessary/requested, each channel's measurements namely pseudorange and pseudorange rate are generated for the navigation filter (Kaplan 1996, Van Dierendonck 1996).

Finally, the navigation filter incorporates the GPS raw measurements with the GPS satellite orbit information to generate position and velocity estimates. The navigation filter, which could be based on least-squares or Kalman filter, is used to estimate the required positioning parameters. The typical estimated states of a GPS receiver are three position and velocity components, the receiver clock bias and the clock drift.

The benefits of the standard receiver architecture are its relative simplicity and robustness. In the case of robustness, such a receiver architecture has independently operated channels and therefore one tracking channel cannot corrupt another one. However, on the downside, the fact that the signals are inherently related via the receiver's position and velocity is completely ignored. Furthermore, the possibility for one tracking channel to aid another channels is lost (Petovello et al 2006).

2.1.2 Vector Based GPS Receiver Architecture

In contrast to the standard GPS receiver architecture, a vector-based receiver applies navigation feedback to each tracking channel. With the position and velocity of the receiver known, the feedback to the local signal generators is obtained from the computed range and range rate to each satellite. The general vector tracking architecture is shown in Figure 2.2 with the green part highlighting the differences between the standard and vector-based receiver. This enables inter-channel aiding among the channels so that strong signals can help track weak signals. Vector-based receivers can be further divided into two categories, cascaded vector-based and centralized vector-based receivers (Lashley & Bevly 2009, Pany et al (2009), Lin et al 2011a, Petovello et al 2008b).

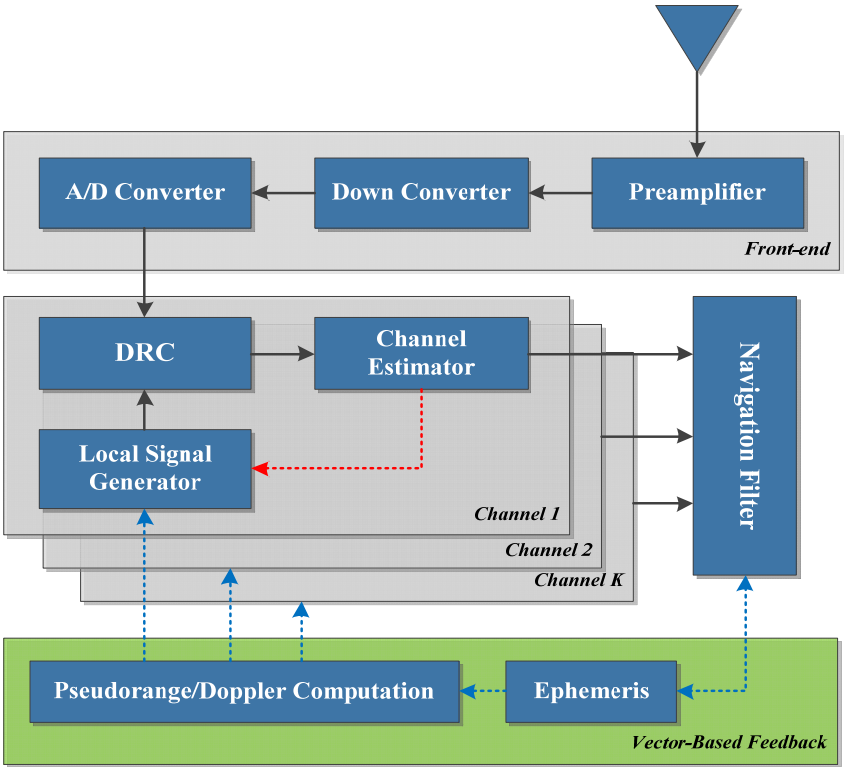

Figure 2.2: Vector-based software GPS receiver

For a cascaded vector-based receiver, direct feedback from the channel estimator to the local signal generator is used for the carrier phase, as illustrated in Figure 2.2 by the red dashed line, since the navigation solution accuracy (or the temporal variability of the navigation solution) is insufficient for carrier phase tracking. The navigation filter is only used to update the code phase and Doppler frequency, which are usually referred to as Vector Delay Lock Loop (VDLL) and Vector Frequency Lock Loop (VFLL) (Lashley & Bevly 2009, Pany et al (2009), Lin et al 2011a, Petovello et al 2008b).

The cascaded vector-based architecture reduces the order of the navigation filter and decreases the input rate into the navigation filter by using local channel filters. Furthermore, it provides carrier phase measurements. Thus, it is suitable for high precision navigation applications. However, under challenging conditions, maintaining carrier phase tracking is often difficult due to the weak signal strength and multipath fading. Therefore, the cascaded vector-based receiver is less suited for land vehicle navigation under harsh environments.

For a centralized vector-based receiver, the feedback from the individual channel estimators to the local signal generator is removed. The outputs from the channel estimators are directly fed into the navigation solution. Then, the local signal generator is completely controlled by the computed code phase and Doppler from the navigation solution. It is noted that due to the limited accuracy of the standalone GPS navigation solution the carrier phase feedback is usually not possible for the centralized vector-based receiver.

The use of centralized vector-based receiver architecture limits the performance degradation and instability issues associated with the channel filters, in particular when a long coherent integration period is used (O'Driscoll et al 2010). Thus the centralized vector-based GPS receiver usually provides improved sensitivity over the cascaded one due to the longer coherent integration time (Pany et al 2009, Lashley & Bevly 2009, Lin et al 2011). However, higher measurement noise levels due to the elimination of the local filter feedback would influence the performance of the navigation solution.

2.2 Overview of Channel Processing Strategies

Having discussed the general receiver architecture, the focus is moved to the channel estimator in this section. Associated with the three main channel estimators, three channel processing strategies, namely scalar processing, Kalman filter processing and block processing, are introduced.

2.2.1 Scalar Processing / Tracking

The block diagram of the scalar processing/tracking strategy is shown in Figure 2.3. The discriminators and loop filters are used as the channel estimator. Within each channel, the down-converted samples from the front-end (not shown) are passed to the DRC module where the Doppler removal and correlation are performed. The correlator outputs are then processed by the discriminators and loop filters to generate the error estimates between the incoming signals and the locally generated signals. Finally, the updated signal parameters are used to control the local signal generator for the DRC. Therefore the local signal replicas always align with the incoming signal if the signal is properly tracked. It is noted

that scalar processing normally uses three correlator outputs namely the early, prompt and late for signal tracking; all three are in the code phase (delay) domain and are all the same in the carrier frequency (Kaplan 1996, Van Dierendonck 1996)..

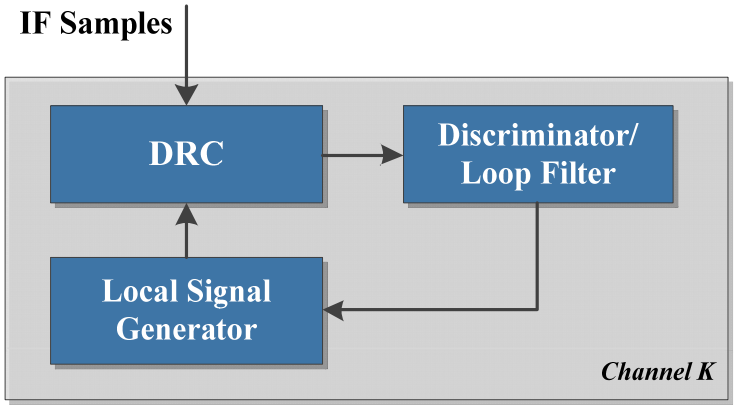

Figure 2.3: Block diagram of scalar tracking architecture

Scalar processing offers the relative ease of implementation and a level of robustness gained by the independent channel implementations. However, on the downside, the loop filter of the scalar processing suffers from stability issues when the longer coherent integration time is used (Kazemi 2010, Lin et al 2011), which limits its use for high sensitivity applications. Although a redesigned digital filter can be used to extend the coherent integration time up to 100 ms (Kazemi 2010), the low update rate and the limited linear region of the discriminators prevent its application for very long coherent integration time (e.g. 1 s).

2.2.2 Kalman Filter Processing / Tracking

Kalman filter can be used to replace both the discriminators and the loop filters as the channel estimator for signal parameter estimation as shown in Figure 2.4. Instead of weighting all the measurements (from the discriminator) equally, the Kalman filter can vary

its gain based on the changing measurement noise statistics and process noise statistics. The measurement noise statistics can be configured to vary with Signal to Noise Ratio (SNR) levels and the process noise statistics to vary with user dynamics. Improved tracking sensitivity with Kalman filter based tracking has been shown by Ziedan & Carrison (2004), Psiaki & Jung (2002) and Psiaki (2001).

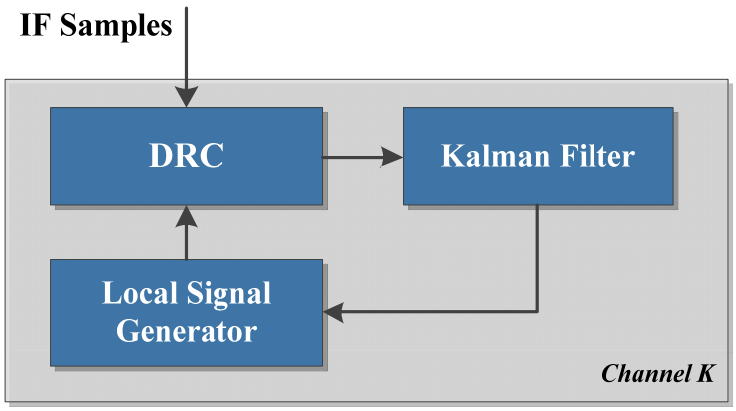

Figure 2.4: Block diagram of Kalman filter tracking architecture

However, a stable weighting strategy of signals under urban canyon environments is difficult to obtain due to the fluctuations of the signal strength caused by multipath fading. Furthermore, the underlying assumption of the Gauss distribution of the channel processing noise for the Kalman filter is not always valid in degraded signal conditions. Finally, merely applying longer coherent integration does not guarantee better tracking performance for a Kalman filter tracking loop. It may result from the conflict between the coherent integration time and the NCO update rate (Lin et al 2011, O'Driscoll et al 2010).

2.2.3 Block Processing Strategy

Unlike the scalar and the Kalman filter processing strategies where the locally generated signals are perfectly aligned with the incoming signal, the block processing strategy allows

for some level of "asynchronization" between the local replicas and the signal. Specifically, a grid of correlators centred on the predicted signal parameters is used. The extent and resolution of the grid can be predefined, or can be computed based on knowledge regarding the receiver/signal uncertainty. At each point in the grid, a local signal is generated and correlated with the incoming signal. Finally, a grid of correlator outputs is used to determine the search centre and ultimately to control the local signal generator (Lin et al 2011).

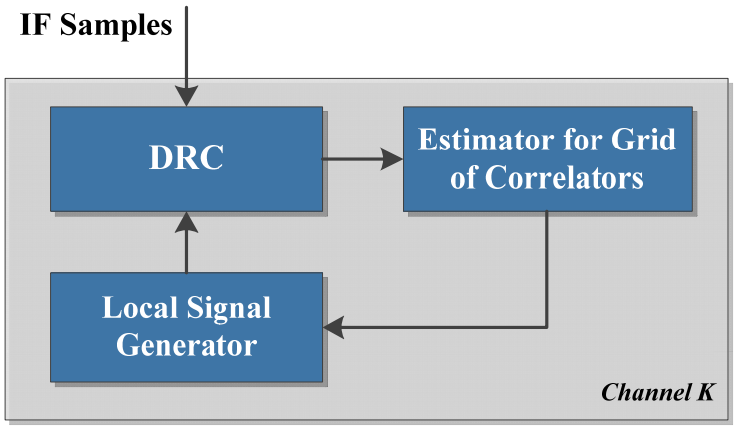

Figure 2.5: Block diagram of block processing architecture

Because of the elimination of the local channel filter, block processing removes the loop filter stability issues. Although sometimes an interpolation filter can be applied to filter the measurements for the block processing, the stability issue of this filter is minimum as compared with the channel filters. Block processing also provides the flexibility to use various combinations of non-coherent and coherent integrations. However, because of the asynchronous nature of the processing, a correlator grid with a large number of correlator outputs is required to generate sufficiently accurate signal parameter estimates. Thus a large computation load and a high power consumption are expected for the block processing strategy.

2.3 Implementation of High Sensitivity Block Processing GPS Receiver

Given that the objective of this work is to maintain five metre accuracy navigation solution under dense foliage or urban canyon environments, a high sensitivity GPS receiver using block processing is implemented. This section provides the implementation details of the proposed high sensitivity GPS receiver.

2.3.1 High Sensitivity Block Processing GPS Receiver Architecture

Figure 2.6 shows the block diagram of the high sensitivity block processing receiver architecture used herein. The receiver is based on the GNSS Software Navigation Receiver (GSNRxR^{TM}) developed by the Position, Location and Navigation (PLAN) group (Petovello et al 2009). The high sensitivity version is denoted as (GSNRx-hs^{TM}). As shown in this figure, GSNRx-hs^{TM} is based on the centralized vector-based receiver architecture with the block processing tracking strategy. It is also noted that external bit aiding is applied as highlighted in the red box for coherent integration times in excess of 20 ms in order to improve the receiver sensitivity. Therefore, the major differences between GSNRx-hs^{TM} used herein and a standard GNSS receiver are as follows: 1) the individual tracking loops (scalar tracking or Kalman filter tracking) in a standard receiver architecture are replaced by the block processing estimator, and the pseudorange and range rate measurements are generated from the estimator for the grid correlators; 2) the navigation solution is used to directly control the local signal generator and determine the center point of the signal parameter uncertainty space; 3) over 20 ms coherent integration time can be applied to improve the tracking sensitivity with external data bit aiding.

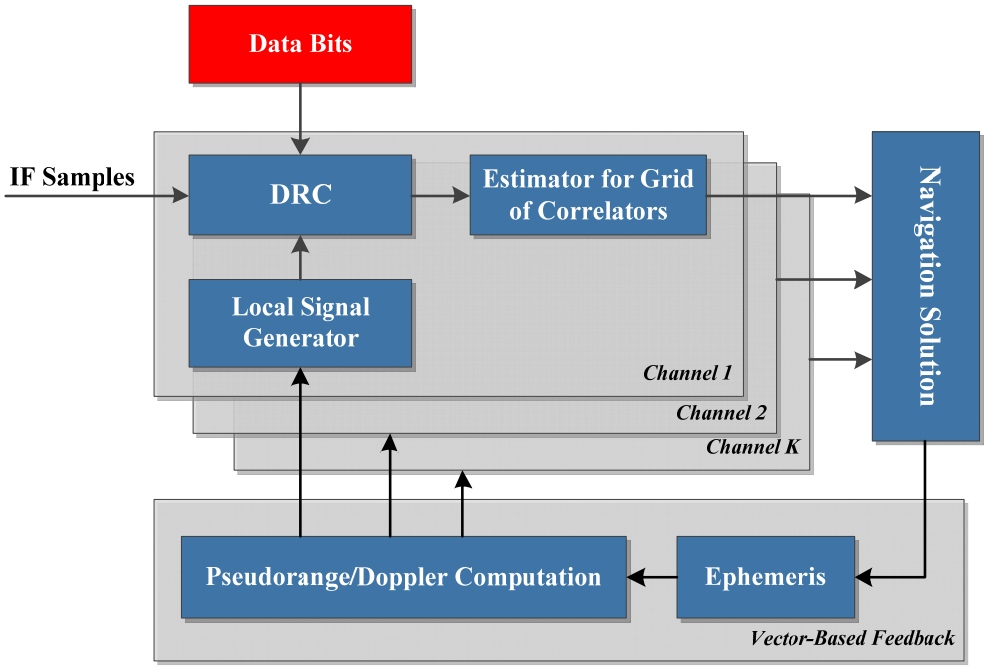

Figure 2.6: Block diagram of GSNRx-hs^{TM} architecture

Compared with the implementations of high sensitivity GPS receivers from previous researchers, GSNRx-hs^{TM} uses an estimator for a grid of correlators rather than the discriminator based implementation used in Pany (2006). The multi-correlator based estimator outperforms the discriminator based implementation because of the increased error determination region. Furthermore, GSNRx-hs^{TM} applies the external data bits aiding instead of estimating them by the receiver itself in Soloviev (2007). The large BER of GPS signals in the weak signal conditions make it difficult to estimate the data bits without aiding information.

It is also noted that GSNRx-hs^{TM} forms the basis of the ultra-tight high sensitivity GPS and vehicle sensor integrated receiver proposed in this thesis. The same receiver architecture to GSNRx-hs^{TM} is applied for the ultra-tight receiver except for the inclusion of vehicle

sensors and the change of navigation equations. Further details of implementation of the ultra-tight receiver are presented in the following chapters.

2.3.2 Estimator for Grid of Correlators

Having introduced the general receiver architecture of GSNRx-hs^{TM}, the implementation details of the major components of the receiver are presented. Firstly, the estimator for grid of correlators is introduced in this section.

The estimator implemented herein is termed as Approximate Maximum Likelihood Estimator (AMLE) (Hurd et al 1987). The basic idea of the AMLE is to approximate the operation of the two-dimensional maximum likelihood estimator using a discrete correlator for code delay and Doppler estimation. A main consequence of using the AMLE is that the estimator works only when the signal delay and frequency fall within the code delay and frequency uncertainty space and their resolution of the search grid is sufficient to generate the correlation peaks. AMLE uses a massive number of correlators to search for the possible code delays and Doppler frequencies with the predefined search space and search resolution. The maximum AMLE peak can be obtained as those of the local replica that maximize the correlation function. Once the maximum peak is identified, using the closest neighbors of the AMLE peak to form the second order parabola, finer pseudorange and range rate estimates are obtained by interpolation.

2.3.3 Navigation Filter

The navigation solution of GSNRx-hs™ is based on a Kalman filter. The system error states $\delta\mathbf{x}$ for the GPS only navigation filter include eight states, and is given by

$$\delta\mathbf{x} = \begin{bmatrix} \delta\mathbf{r}^n & ct & \delta\mathbf{v}^n & c\delta t \end{bmatrix}^T \tag{2.1}$$

where

$\delta\mathbf{r}^n$ is the position error vector in the East, North and Up (ENU) directions; $\delta\mathbf{r}^n = \begin{bmatrix} \delta r^E & \delta r^N & \delta r^U \end{bmatrix}$;

ct is the receiver clock bias state;

$\delta\mathbf{v}^n$ is the velocity error vector in the local level frame $\delta\mathbf{v}^n = \begin{bmatrix} \delta v^E & \delta v^N & \delta v^U \end{bmatrix}$;

cdt is the receiver clock drift state.

For the position and velocity model, velocity random walk is used as

$$\begin{bmatrix} \delta\dot{\mathbf{r}}^n \\ \delta\dot{\mathbf{v}}^n \end{bmatrix} = \begin{bmatrix} 0 & 1 \\ 0 & 0 \end{bmatrix} \begin{bmatrix} \delta\mathbf{r}^n \\ \delta\mathbf{v}^n \end{bmatrix} + \begin{bmatrix} 0 \\ \eta_v \end{bmatrix} \tag{2.2}$$

where the "over dot" denotes the time derivative. w_v is the driving noise for the velocity error state with units of $m^2/s^4/Hz$.

The receiver clock bias and the clock drift are modeled as a random walk processes. The clock error states are defined in units of length (metres and metres per second). Therefore, the GPS error model can be written as (Brown & Hwang 1992)

$$\begin{bmatrix} \dot{ct} \\ \dot{cdt} \end{bmatrix} = \begin{bmatrix} 0 & 1 \\ 0 & 0 \end{bmatrix} \begin{bmatrix} ct \\ cdt \end{bmatrix} + \begin{bmatrix} w_b \\ w_d \end{bmatrix} \tag{2.3}$$

where

w_b is the driving noise of clock bias with spectral density q_t;

w_d is the driving noise of clock drift with spectral density q_{ct}.

For computing the clock error spectral densities, a standard clock stability model is used where the spectral densities are computed as (Brown & Hwang 1992)

$$\begin{aligned} q_t &= h_0 \\ q_{\delta t} &= 8\pi^2 h_2 \end{aligned} \qquad 2.4$$

where h_0 and h_2 are Allan variance parameters that describe clock stability.

For the measurement equation of the navigation filter, the differences between GPS pseudorange and pseudorange rate measurements and the system predicted pseudoranges and pseudorange rates are used as the observation vector $\delta\mathbf{Z}$. It is noted that the relationship between pseudorange rate and Doppler is

$$f = \frac{\dot{\rho}}{\lambda_{L1}} \qquad 2.5$$

where f is the Doppler and $\dot{\rho}$ is the corresponding pseudorange range rate; λ_{L1} is L1 carrier wavelength.

Assuming there are n satellites in-view, the measurement misclosures can be written as:

$$\delta\mathbf{Z} = \begin{bmatrix} \delta\mathbf{Z}_\rho \\ \delta\mathbf{Z}_{\dot{\rho}} \end{bmatrix} = \begin{bmatrix} \boldsymbol{\rho}_{GPS} \\ \dot{\boldsymbol{\rho}}_{GPS} \end{bmatrix}_{2n\times 1} - \begin{bmatrix} \hat{\boldsymbol{\rho}} \\ \hat{\dot{\boldsymbol{\rho}}} \end{bmatrix}_{2n\times 1} \qquad 2.6$$

where, $\delta\mathbf{Z}_{\rho}$ and $\delta\mathbf{Z}_{\dot{\rho}}$ represent the range and range rate misclosures; $\boldsymbol{\rho}_{GPS}$ and $\dot{\boldsymbol{\rho}}_{GPS}$ are the raw GPS pseudorange and pseudorange rate measurements; $\hat{\boldsymbol{\rho}}$ and $\hat{\dot{\boldsymbol{\rho}}}$ are the predicted pseudorange and pseudorange rate measurements. The i-th elements of $\hat{\boldsymbol{\rho}}$ and $\hat{\dot{\boldsymbol{\rho}}}$ are the predicted pseudorange $\hat{\rho}^i$ and pseudorange rate $\hat{\dot{\rho}}^i$ for the i-th satellite respectively, which can be computed as

$$\hat{\rho}^i = \sqrt{(r^i_{s,x} - \hat{r}^e_x)^2 + (r^i_{s,y} - \hat{r}^e_y)^2 + (r^i_{s,z} - \hat{r}^e_z)^2} + c\hat{t} \qquad 2.7$$

$$\hat{\dot{\rho}}^i = -\hat{e}^i_x(v^i_{s,x} - \hat{v}^e_x) + \hat{e}^i_y(v^i_{s,y} - \hat{v}^e_y) + \hat{e}^i_z(v^i_{s,z} - \hat{v}^e_z) + c\hat{dt} \qquad 2.8$$

where

$[r^i_{s,x} \quad r^i_{s,y} \quad r^i_{s,z}]^T$ is the position vector of the i-th satellite in e-frame;

$[v^i_{s,x} \quad v^i_{s,y} \quad v^i_{s,z}]^T$ is the velocity vector of the i-th satellite in e-frame;

$[\hat{r}^e_x \quad \hat{r}^e_y \quad \hat{r}^e_z]^T$ is the predicted position vector transformed into e-frame;

$[\hat{v}^e_x \quad \hat{v}^e_y \quad \hat{v}^e_z]^T$ is the predicted velocity vector transformed into e-frame;

$[\hat{e}^i_x \quad \hat{e}^i_y \quad \hat{e}^i_z]^T$ is the unit vector along the line of sigh between the satellite position and the predicted receiver position.;

$c\hat{t}$, $c\hat{dt}$ are the estimated receiver clock bias and drift.

The line of sight vector can be written as

$$\mathbf{e}^i = [\hat{e}^i_x \quad \hat{e}^i_y \quad \hat{e}^i_z]^T = [\frac{r^i_{s,x} - \hat{r}^e_x}{\left\|\mathbf{r}^i_s - \hat{\mathbf{r}}^e\right\|} \quad \frac{r^i_{s,y} - \hat{r}^e_y}{\left\|\mathbf{r}^i_s - \hat{\mathbf{r}}^e\right\|} \quad \frac{r^i_{s,z} - \hat{r}^e_z}{\left\|\mathbf{r}^i_s - \hat{\mathbf{r}}^e\right\|}]^T \qquad 2.9$$

where, $\left\| \mathbf{r}_s^i - \hat{\mathbf{r}}^e \right\|$ denotes the distance between the satellite position and the predicted position.

Thus the pseudorange measurement equation is given as

$$\delta \mathbf{Z}_\rho^i = \rho_{GPS}^i - \hat{\rho}^i = H_{\rho,1\times 3}^i \begin{bmatrix} \delta r^E \\ \delta r^N \\ \delta r^U \end{bmatrix}^T + c\delta t + v_\rho^i \qquad 2.10$$

where $H_{\rho,1\times 3}^i = \begin{bmatrix} -\cos(E)\sin(A) & -\cos(E)\cos(A) & -\sin(E) \end{bmatrix}$, and A and E are the satellite elevation angle and azimuth respectively.

Similarly, the range rate misclosure for the i-th satellite is given as

$$\delta \mathbf{Z}_{\dot{\rho}}^i = \dot{\rho}_{GPS}^i - \hat{\dot{\rho}}^i = H_{\dot{\rho},1\times 3}^i \begin{bmatrix} \delta v^E \\ \delta v^N \\ \delta v^U \end{bmatrix}^T + c\delta dt + v_{\dot{\rho}}^i \qquad 2.11$$

where $H_{\dot{\rho},1\times 3}^i = \begin{bmatrix} -\cos(E)\sin(A) & -\cos(E)\cos(A) & -\sin(E) \end{bmatrix}$.

Finally, the measurement model for the GPS navigation filter can be written as

$$\delta \mathbf{Z} = \begin{bmatrix} \delta \mathbf{Z}_\rho \\ \delta \mathbf{Z}_{\dot{\rho}} \end{bmatrix}_{2\times n,1} = \mathbf{H}\delta \mathbf{x} + \mathbf{v} \qquad 2.12$$

where n is the number of satellites in view and the design matrix $\mathbf{H}$ is given by

$$\mathbf{H} = \begin{bmatrix} \mathbf{H}_{\rho,n\times 3} & 1_{n\times 1} & 0_{n\times 3} & 0_{n\times 1} \\ 0_{n\times 3} & 0_{n\times 1} & \mathbf{H}_{\dot{\rho},n\times 3} & 1_{n\times 1} \end{bmatrix} \qquad 2.13$$

2.3.4 Vector-based Navigation Solution Feedback

Having reviewed the navigation filter and the channel filter, the vector-based navigation feedback is discussed in this section.

When the receiver is operated in vector-based mode, the position and velocity estimated from the navigation filter are used to control the local NCOs. The update rate of NCOs mainly depends on the GPS measurement update rate. Because the transmitted signal is corrupted by a variety of errors such as the satellite clock error, ionospheric error and tropospheric error, the received signal's code phase and Doppler are affected. Since the navigation solution derived pseudorange and Doppler are computed based on the true range and Doppler, those errors should be reintroduced before they are applied to the NCOs. Therefore the navigation solution derived code phase, which is used to update the code NCO for the i-th satellite is given as (Lashley 2006)

$$\tau_{NCO}^{i} = \mathrm{mod}(t_{receiver} \cdot f_c - \frac{f_c(\hat{\rho}^i + ct - ct_s + \Delta d_{tr} + c\Delta d_g)}{c}, 1023) \qquad 2.14$$

where the function mod(A, B) computes the remainder of A/B ,

$t_{receiver}$ is the receiver time;

f_c is the code chipping rate;

$\hat{\rho}^i$ is the navigation solution derived range;

ct is the receiver clock bias in metres;

ct_s is the satellite clock bias in metres;

Δd_{tr} is the tropospheric delay in metres;

$c\Delta d_g$ is the group delay in metres.

Similarly, the navigation solution derived Doppler, which is used to update the carrier NCO for the i-th satellite is given as (Lashley & Bevly 2006, Yang 2008)

$$f_{NCO}^{i} = \frac{\hat{\dot{\rho}}^{i} + c\dot{dt} - c\dot{dt}_s}{\lambda_{L1}} \qquad 2.15$$

where

$\hat{\dot{\rho}}^{i}$ is the navigation solution derived range rate before error compensation;

$c\dot{dt}_s$ is the satellite clock drift.

2.4 Field Test Results and Performance Analysis

Having explained the operational principles of the high sensitivity block processing GSNRx-hs™, this section uses field test results to evaluate its performance of the receiver in both the tracking and navigation domain under different operational environments. The performance analysis of the GSNRx-hs™ provides useful information for the design and implementation of the ultra-tight GPS receiver described in later chapters. The field test was conducted under two scenarios: suburban and foliage scenario and urban canyon scenario. For comparison purposes, the results from the standard GSNRx™ and a commercial automotive grade HSGPS receiver were also analyzed.

2.4.1 Suburban and Foliage Scenario

The performance of the GSNRx-hs^{TM} receiver using the block processing architecture is analyzed in the suburban and foliage scenario first. This scenario is used to evaluate the system performance under a slightly degraded signal environment.

2.4.1.1 Field Test description

A field test was on conducted in a suburban and foliage environment in the neighbourhood of Calgary on 19 August 2011. The test vehicle was a 2009 model Sports Utility Vehicle (SUV).

Figure 2.7 shows the block diagram of the equipment setup for the suburban and foliage test. A NovAtel 702GG antenna, which has 13 dB gain roll off from zenith to horizon, was used to receive the GPS signal which was then split into three branches. The first branch was connected to a NovAtel SPAN SE™ system; the second branch was connected to an automotive grade high sensitivity GPS receiver; and the third branch was connected to the front-end. The front-end down-converted the signal to an intermediate frequency (IF) of 0.42 MHz and sampled it at 10 MHz (complex) with 16 bit quantization level (although typically only 3-4 bits are necessary). Also noted is that a relatively high quality OCXO (0.5 ppm) was used in the front-end. The samples were recorded to disk for post-processing. The SPAN™ system consists of a NovAtel OEMV receiver and an IMU, in this case a Northrop-Grumman UIMU-LCI IMU ("LCI"). The LCI is a tactical-grade IMU with a turn-on gyro bias of 1 deg/h which is synchronized by the NovAtel OEMV receiver. Raw GPS pseudorange and range rate measurements were logged from the SPAN™ system at

20 Hz, while the raw IMU data (i.e., velocity and angular increments) from the LCI was logged at 200 Hz into a Compact Flash (CF) card. The automotive grade GPS receiver collected the raw GPS pseudorange and Doppler measurements at 2 Hz.

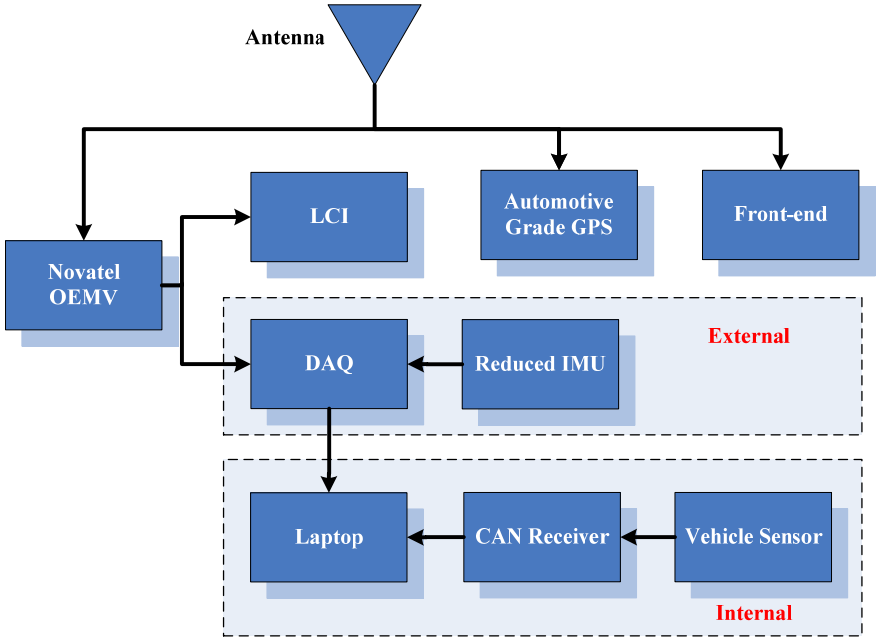

Figure 2.7: Block diagram of equipment setup for the suburban and foliage test

Data from the onboard vehicle sensors including one lateral accelerometer, one vertical gyro, four wheel speed sensors (WSS) and one steering angle sensor (SAS) were received by the CAN-bus receiver. The laptop was used to record the data from CAN-bus recevier and to time tag (in a relative sense) each received data record. In addition to the internal vehicle sensor described above, data from an external reduced IMU ("external RIMU") containing two lateral accelerometers and one gyro (of the same quality as what is contained inside the vehicle) was collected using a data acquisition device (DAQ) in the test and was time tagged using the PPS signal from the NovAtel OEMV receiver.

Figure 2.8: Reference IMU, reduced IMU and antenna used in the foliage test

Figure 2.8 shows the equipment inside and outside of the vehicle. As shown in the figure (left side), the LCI IMU and the external RIMU were rigidly mounted the base of the roof rack on the SUV. The NovAtel 702GG antenna was also mounted on the roof of the vehicle. The equipment was powered by the vehicle directly or by additional batteries.

To get an idea of the relative quality of the tactical grade IMU (LCI) and the automotive IMUs used in the vehicle, Table 2.1 compares the gyro parameters (the gyro errors are more significant than the accelerometer errors in terms of navigation performance). It is clear that the automotive IMU used in the vehicle, being based on MEMS technology, are of considerably poorer quality.

Table 2.1: LCI and automotive grade IMU parameters

Sensor	LCI	Automotive IMU
Gyro In-Run Variability	1.0 deg/hr	113 deg/hr
Angular Random Walk	0.05 deg/hr/√Hz	1044 deg/hr/√Hz

In order to generate a reference solution using DGPS/INS integration, a NovAtel OEMV receiver was setup on a building roof at the University of Calgary to act as the base station.

The raw pseudorange and Doppler measurement rate for this receiver was 1 Hz. The processing strategy of the reference solution is introduced in Section 2.4.1.3.

2.4.1.2 Foliage Test Environment

The test lasted about 20 minutes starting with a relatively open sky area for the purpose of reference solution initialization. Figure 2.9 shows the suburban and foliage test environments. As shown in this figure, the sky was nearly obscured by three branches of during the foliage test. Figure 2.10 shows the test trajectory in Google Earth™ and illustrates the foliage test areas. For the test route selected, the test vehicle first entered the test area and ran for about 300 s, then went into the foliage test area and ran for about 500 s. Finally, the vehicle went back the same route from the foliage area to the suburban area. Figure 2.11 shows the satellite sky plot during the test. There were 10 satellites in view with elevation angles varying between 71 degrees to 5 degrees.

Figure 2.9: Suburban (left) and foliage (right) test environment

Figure 2.10: Trajectory of the foliage test

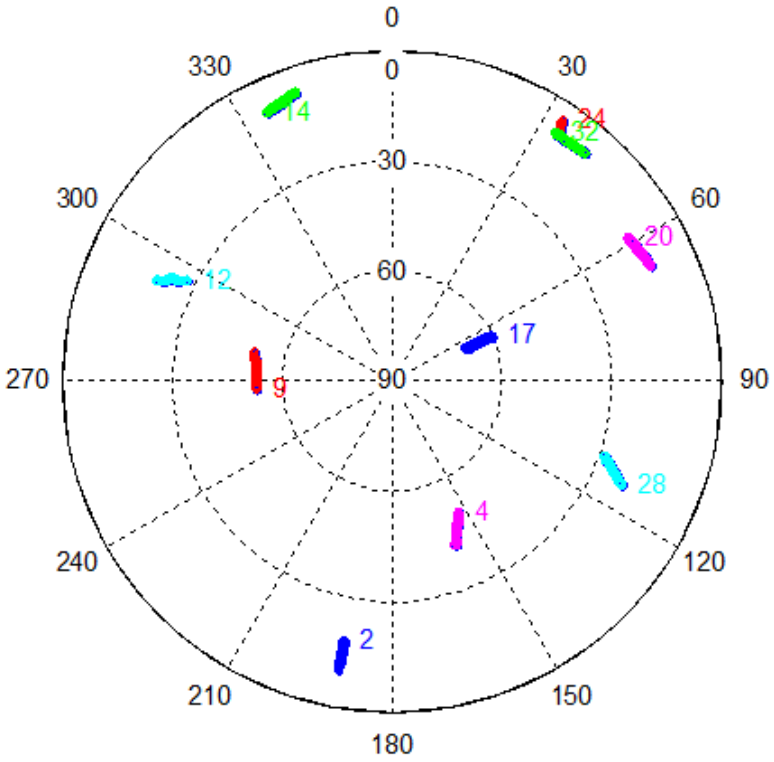

Figure 2.11: Satellite sky plot during the foliage test

2.4.1.3 Data Processing and Analysis Strategy

The reference solution was generated using the NovAtel Inertial Explorer™ post-processing software. The reference solution applied tight integration of the DGPS and LCI with combined forward and backward smoothing. Table 2.2 summarizes the estimated positioning accuracy of the reference solution. As shown in the table, the estimated accuracy of the reference solution (per axis) is 0.2 m for position and 0.02 m/s for velocity. The attitude solution of the integrated system is about 0.20 degrees for pitch and roll, and 0.75 degrees for azimuth. This is considered sufficient for the analysis performed herein. The reference velocity and attitude plot are shown in Figure 2.12 and Figure 2.13. The maximum speed is about 15 m/s. The vehicle's pitch and roll were within 5 degrees.

Table 2.2: Estimated accuracy of the reference solution

Position (m)	Velocity (m/s)	Pitch/Roll (deg)	Azimuth (deg)
0.2	0.02	0.20	0.75

Different coherent integration time and search space sizes were applied for the post-processing to evaluate the performance of GSNRx-hs^{TM}. The optimum receiver parameters including integration time, search space size and processing time were determined based on the performance analysis. The recorded tracking and navigation results from the automotive grade GPS receiver during the data collection were also decoded for the performance comparison.

The analysis of the processed results is performed in both the tracking domain and navigation domain. The performance of GSNRx-hs^{TM} is compared with the standard GSNRx^{TM} and the automotive grade GPS receiver. For the positioning domain analysis, the position and velocity accuracy are used as the criteria to assess the system performance. The tracking performance is evaluated by means of the number of tracked satellites and tracked carrier to noise density (C/N_0) values. In the context of the thesis, a "tracked satellite" means that the satellite is code and frequency locked with navigation bit synchronization. The estimated C/N_0 that indicates the signal quality is also used as the metric of the tracking performance. Furthermore, the estimated Doppler accuracy is used for the performance evaluation of the tracking capability.

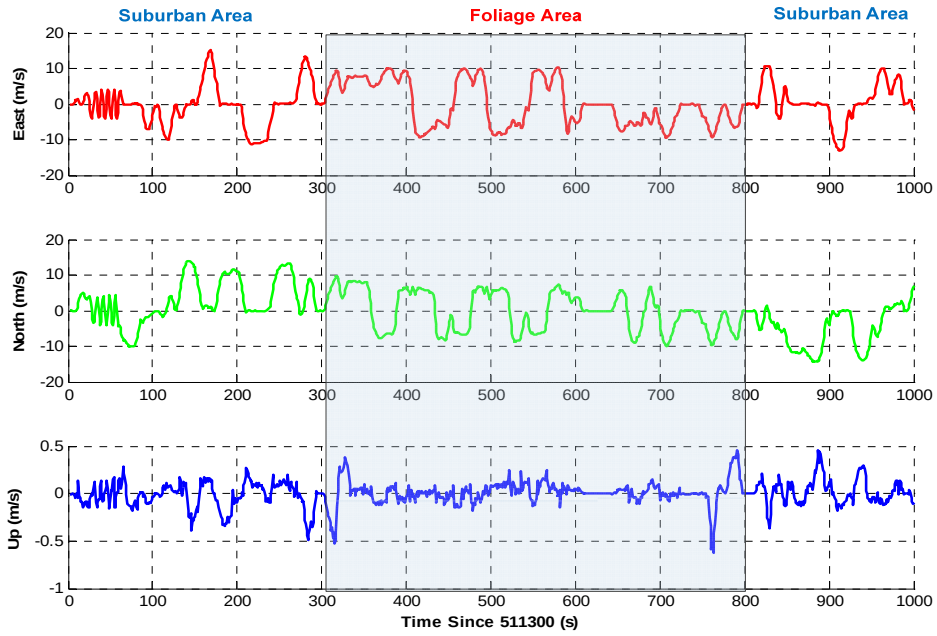

Figure 2.12: Reference velocity plot of the suburban and foliage test

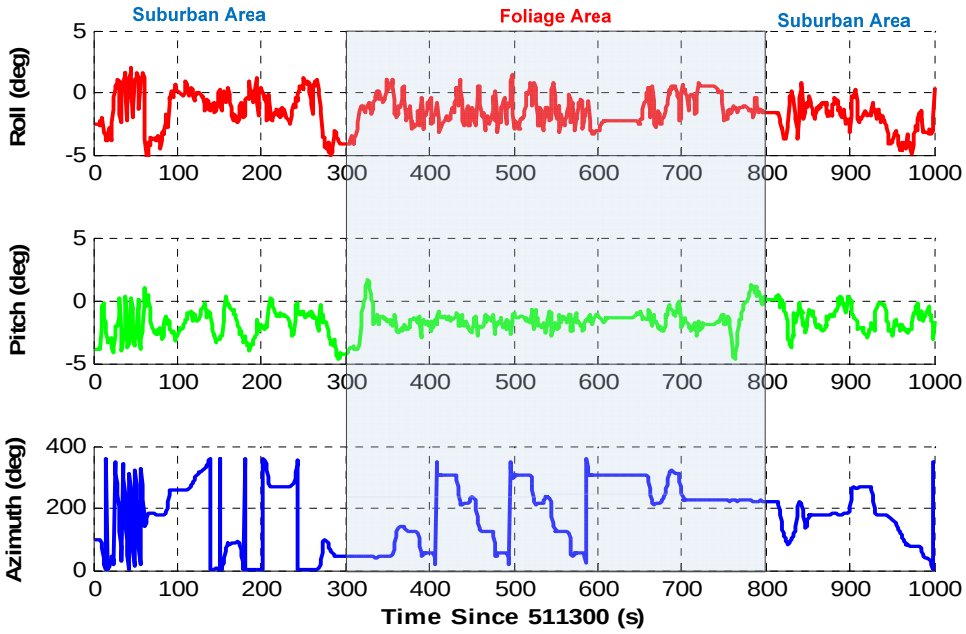

Figure 2.13: Reference attitude plot of the suburban and foliage test

2.4.1.4 Position Domain Performance Analysis

Firstly, the performance of the GPS only solutions is analyzed in the position domain. The position and velocity accuracy are used to assess the positioning performance of the various receivers. The performances of the standard GSNRx^{TM}, the high sensitivity GSNRx-hs^{TM}, and the automotive grade GPS receiver are used for the analysis herein.

The position and velocity error plots from the three GPS receivers are shown in Figure 2.14 and Figure 2.15 respectively. GSNRx^{TM} receiver used 20 ms coherent integration time with a standard PLL/DLL tracking loop. The GSNRx-hs^{TM} used 100 ms coherent integration time with the pseudorange and range rate uncertainty being 150 m and 2m/s respectively. Both GSNRx^{TM} and GSNRx-hs^{TM} provided a 10 Hz measurement output rate. The automotive grade GPS receiver used here had a 2 Hz measurement output rate. As shown in this figure, there were relatively large velocity and position error variations during the 300 – 800 s interval. These variations are mainly due to signal degradation when the vehicle entered into the foliage area. In terms of positioning accuracy, as shown in the two figures, GSNRx-hs^{TM} provides a similar position accuracy as that of the automotive grade HSGPS receiver but slightly better velocity accuracy in the suburban and foliage scenarios. This can also be verified by the position and velocity error histogram plots illustrated in Figure 2.16. As expected, the standard GSNRx™ cannot provide sufficient sensitivity for reliable navigation solution in foliage areas.

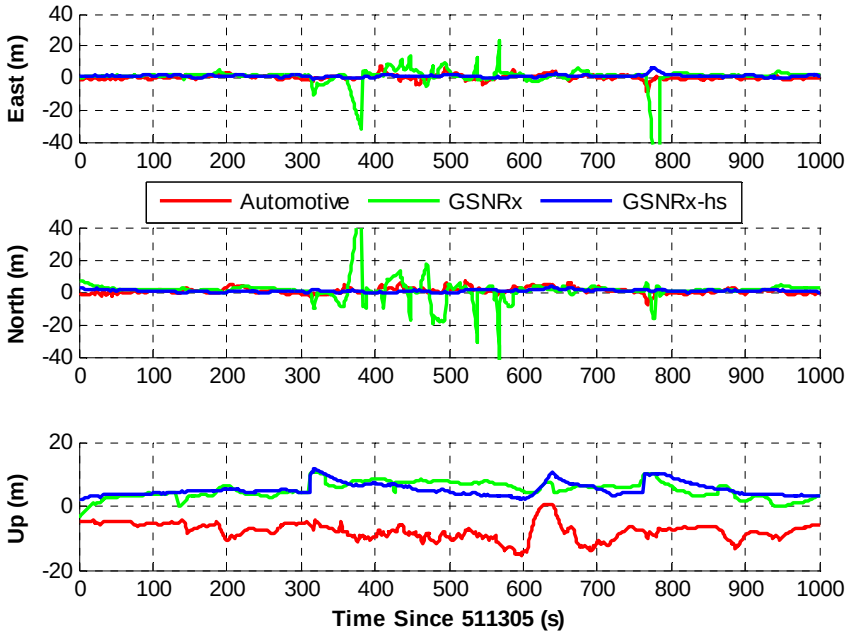

Figure 2.14: Position error plots in suburban and foliage test

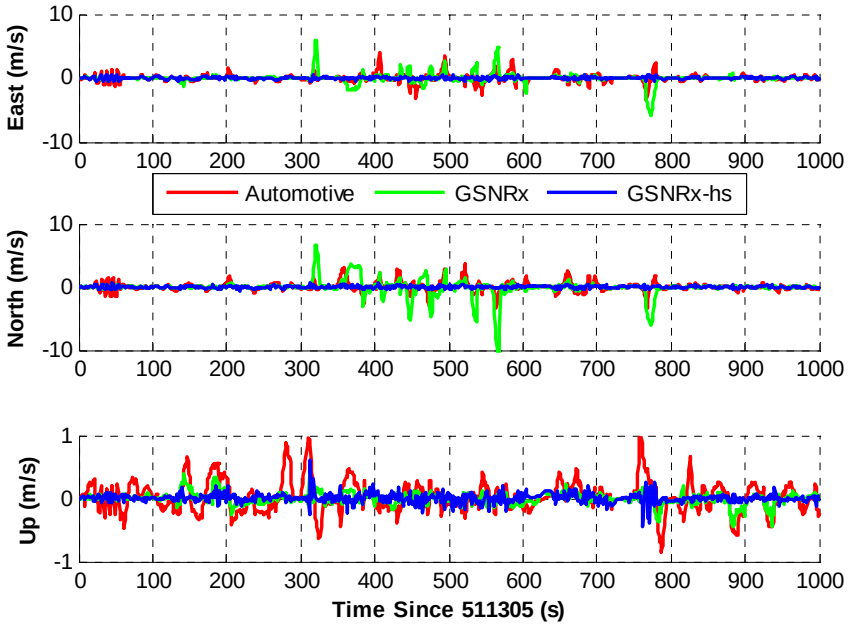

Figure 2.15: Velocity error plots in suburban and foliage test

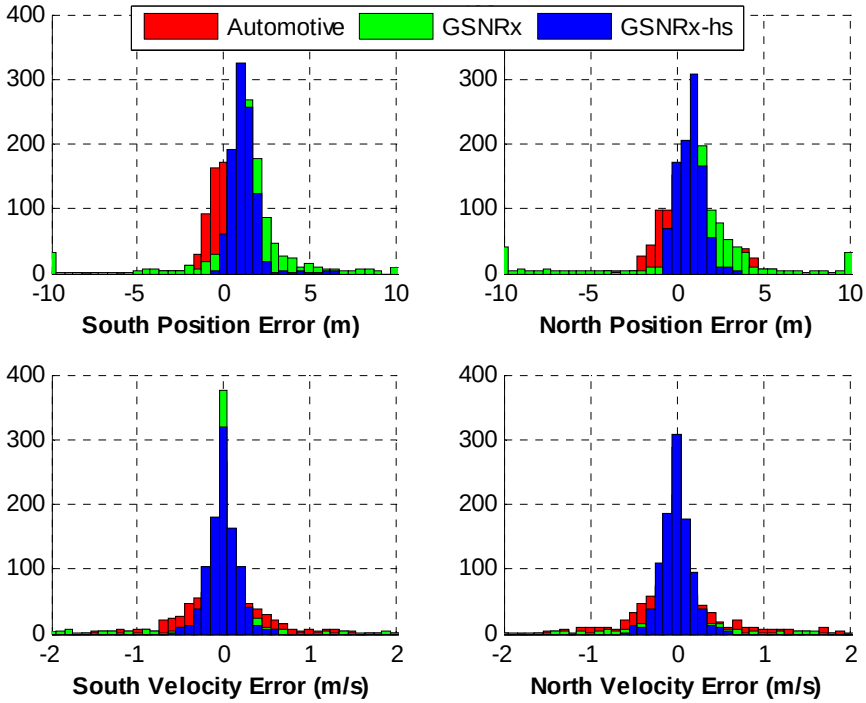

Figure 2.16: Error histogram of the receivers in suburban and foliage test

Table 2.3 summarizes the RMS position and velocity errors from the automotive grade GPS receiver, GSNRx™ and GSNRx-hs™ respectively. It is also noted that the height and vertical velocity from GSNRx™ and GSNRx-hs™ are constrained in the navigation processing. Therefore, even the standard GSNRx™ demonstrates a higher vertical velocity accuracy as compared to that of the automotive grade GPS receiver.

Table 2.3: Summarized RMS position and velocity errors with GPS only solutions in the suburban and foliage test

	Position (m)			Velocity (m/s)		
	East	North	Up	East	North	Up
Automotive	1.8	2.1	7.8	0.64	0.72	0.25
GSNRx™	7.0	7.2	5.7	1.37	0.84	0.09
GSNRx-hs™	1.5	1.1	5.6	0.17	0.17	0.07

Figure 2.17 shows the number of satellites used in the navigation solution from GSNRx^{TM} and GSNRx-hs^{TM}. In the dense foliage area (300 – 800 s), more GPS measurements from GSNRx-hs^{TM} as compared to GSNRx^{TM} are used in the navigation solution. It is mainly due to the improved tracking sensitivity from GSNRx-hs^{TM}.

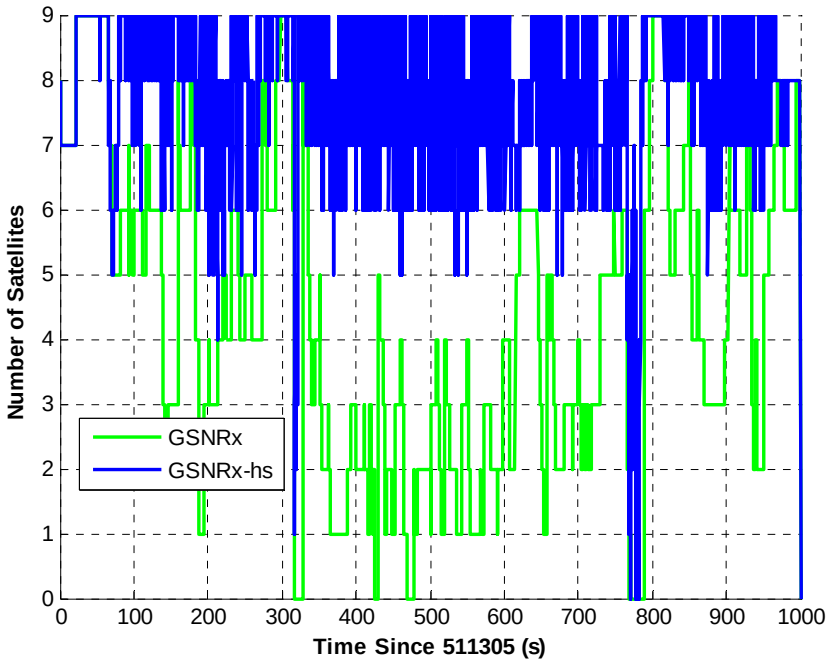

Figure 2.17: Number of satellites used in the navigation solution in the foliage test

In order to analyze the navigation performance as the function of the search space for the high sensitivity block processing receiver, post-processing results using different search spaces reported here. To begin with the analysis, the navigation performance using different frequency uncertainties is evaluated. It is noted that the term "uncertainty" used here is the double side +/- uncertainty. For example, the 2 m/s frequency uncertainty means that the frequency ranges from -1 m/s to 1 m/s. Four frequency uncertainties were applied for the analysis namely 2 m/s, 4 m/s, 6 m/s and 8 m/s with a 1 m/s frequency step size. The coherent integration time and the range uncertainty are still 100 ms and 150 m respectively.

Table 2.4: Summarized RMS position and velocity errors as a function of frequency search uncertainties in the suburban and foliage test

	Position (m)			Velocity (m/s)		
	East	North	Up	East	North	Up
2 m/s	1.5	1.1	5.6	0.17	0.17	0.07
4 m/s	1.6	1.1	5.8	0.20	0.19	0.08
6 m/s	2.0	1.5	5.8	0.20	0.20	0.08
8 m/s	2.1	1.5	5.8	0.21	0.20	0.08

Table 2.4 summarizes the RMS position and velocity errors as a function of the various frequency search spaces in the suburban and foliage scenario. As shown in this table, the GSNRx-hs^{TM} using a 2 m/s frequency uncertainty offers the best position and velocity accuracy. With an increase of the frequency search space, the navigation performance drops. Even this performance degradation is minimal; it suggests that large frequency uncertainty increases the possibility of utilizing the erroneous correlation peaks (due to multipath) for the final navigation solution. Therefore, given the reliable navigation solution obtained in the suburban and foliage scenario and the vector based feedback mechanism used in the GSNRx-hs^{TM}, the small frequency search space is desirable in this case.

A similar analysis strategy can be applied for the navigation performance as a function of the range uncertainty. The range uncertainties used for the processing were 150 m, 300 m and 450 m with a step size of 25 m. The coherent integration time and the frequency uncertainty are 100 ms and 2 m/s respectively. Similar conclusions can be drawn as for the frequency uncertainty analysis, namely that the increased range uncertainty decreases the

position and velocity accuracy, especially the position accuracy. Therefore, a 150 m range uncertainty is sufficiently large in this test scenario to provide reliable navigation solution.

Table 2.5: Summarized RMS position and velocity errors as a function of range search uncertainties in the suburban and foliage test

	Position (m)			Velocity (m/s)		
	East	North	Up	East	North	Up
150 m	1.5	1.1	5.6	0.17	0.17	0.07
300 m	1.6	1.4	6.0	0.17	0.17	0.07
450 m	1.6	1.5	6.1	0.17	0.18	0.08

Finally, the navigation performance as a function of coherent integration time is presented. Three sets of coherent integration time namely 20 ms, 50 ms and 100 ms are used for the analysis. The 150 m and 8 m/s range and frequency uncertainty were applied in this case, respectively. Table 2.6 lists the positioning and velocity errors as a function of coherent integration time. As shown in this table, the higher the coherent integration time, the better the navigation performance. As the objective of the work is to obtain 5 m RMS position error, 50 ms integration time is sufficient for suburban and foliage scenarios.

Table 2.6: Summarized RMS position and velocity errors as a function of coherent integration time in the suburban and foliage test

	Position (m)			Velocity (m/s)		
	East	North	Up	East	North	Up
20 ms	5.7	4.6	8.0	0.43	0.34	0.18
50 ms	3.7	3.5	6.3	0.30	0.20	0.13
100 ms	1.5	1.1	5.6	0.17	0.17	0.07

2.4.1.5 Tracking Domain Performance Analysis

Having discussed the performance of the three GPS receivers in the navigation domain, the tracking performance is analyzed in terms of the number of tracked satellites, tracked C/N_0 values and estimated Doppler accuracy.

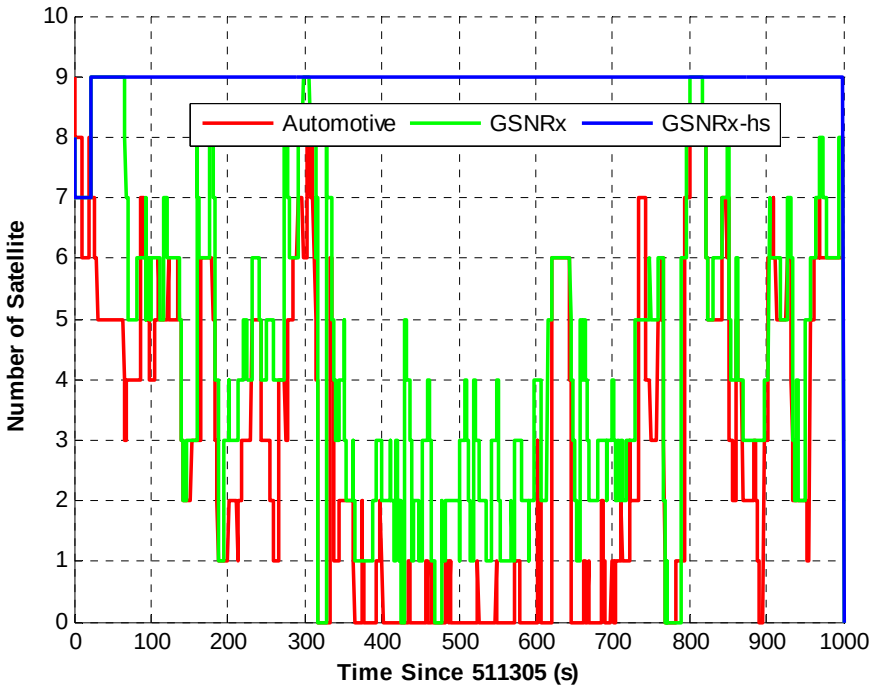

Figure 2.18: Number of tracked satellites in the suburban and foliage test

In the context of this report, a "tracked satellite" means that the satellite is code and frequency locked with navigation bit synchronization. However, it is not the case for the block processing in which a satellite is defined as being tracked after bit synchronization and until it is out of view. Instead, the number of tracked satellites for the block processing represents the number of successfully initialized tracking channels (one per satellite). Successful initialization means completion of the bit synchronization in this case. It is noted that this metric is not indicative of actual tracking performance. Therefore, C/N_0 is used as a better indicator for the tracking performance analysis in this thesis. Figure 2.18 shows the

number of satellites during the suburban and foliage test. The number of tracked satellites for GSNRx-hs™ remains constant during the test as discussed before. GSNRx™ provides a higher number of tracked satellites compared to that of the automotive grade GPS receiver. However, the unreliable re-acquisition and signal lock of satellites with degraded signal power may contribute to the higher number of tracked satellites but with poor navigation performance.

Figure 2.19 shows the estimated C/N_0 plots of PRN 17 from different receivers. PRN 17 is a high elevation satellite with an elevation angle of 65 deg. It is noted that different receivers used different C/N_0 estimation methods. GSNRx™ uses the prompt correlation results to generate C/N_0 estimates whereas GSNRx-hs™ uses the highest correlation peak among all the correlator outputs to generate C/N_0 estimates. The estimated C/N_0 for PRN17 from the three receivers remains at a similar level which indicates that the three receivers have similar tracking performance for high elevation satellites in the foliage scenario. Figure 2.20 illustrates the cumulative C/N_0 estimates for PRN 17 from the three receivers. Cumulative C/N_0 plots indicate the percentage of the C/N_0 estimates that are above the specific C/N_0 values (on the x-axis). As shown, 100% of C/N_0 estimates are above 0 dB-Hz for all the three receivers. In contrast, the value drops to 93% with C/N_0 estimates above 45 dB-Hz for the automotive grade GPS receiver, 89% for GSNRx-hs™ receiver, and 81% for GSNRx™ receiver. The more rapid drop off of GSNRx-hs™ relative to the automotive grade GPS receiver at high C/N_0 values is likely due to small differences in the C/N_0 estimation algorithms used. (See Figure 2.20). In any event, these differences are of no practical importance in the context of this work. Figure 2.21 shows the Doppler error for

the three receivers. GSNRx-hs™ provides the best performance with less variations of the Doppler error. It is mainly due to the vector based tracking structure with compensated user motion dynamics. GSNRx™ shows frequency loss lock indicated by the large Doppler error spikes in this figure.

In contrast, Figure 2.22 shows the estimated C/N_0 plots of PRN 32 which is a relatively low elevation satellite with an elevation angle of 8 deg. In this case, GSNRx-hs™ and automotive grade GPS receivers have similar C/N_0 estimation performance. Figure 2.21 more clearly shows the quality of the C/N_0 estimates for the three receivers and confirmed the above. However, GSNRx-hs™ provides improved Doppler values estimated as shown in Figure 2.24. GSNRx™ cannot provide sufficient tracking sensitivity for reliable Doppler estimates.

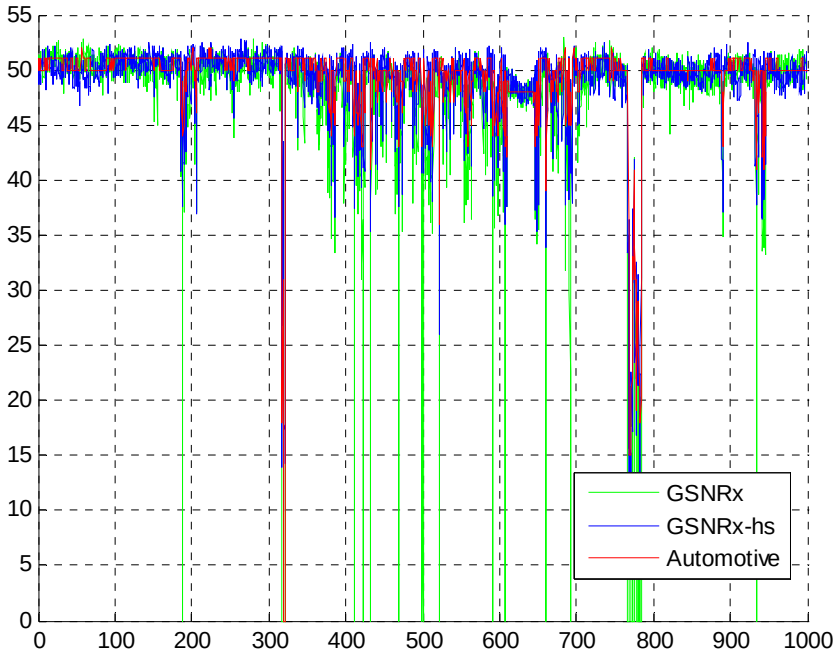

Figure 2.19: C/N_0 plots of PRN 17 in the suburban and foliage test

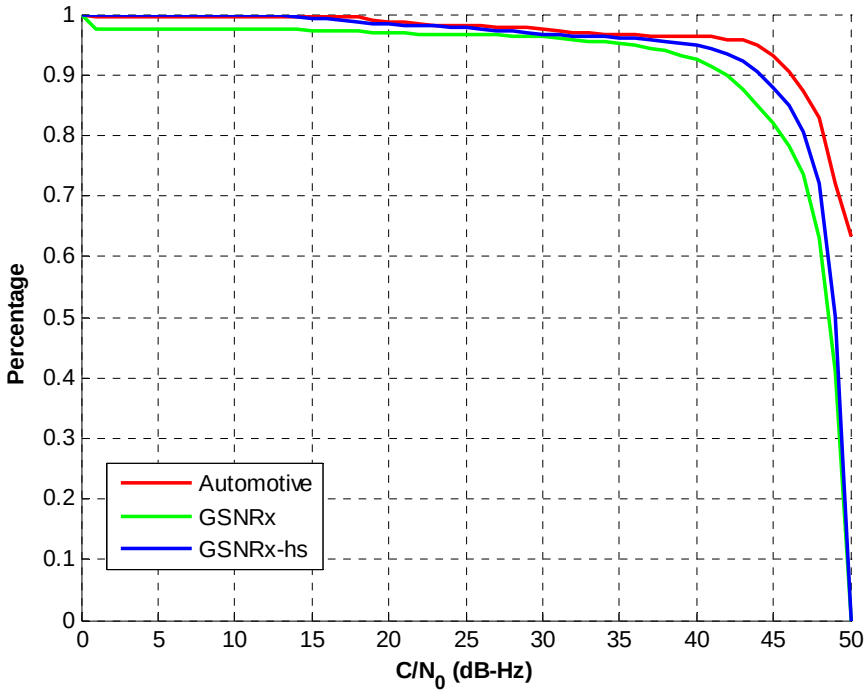

Figure 2.20: Cumulative C/N_0 plots of PRN 17 in the suburban and foliage test

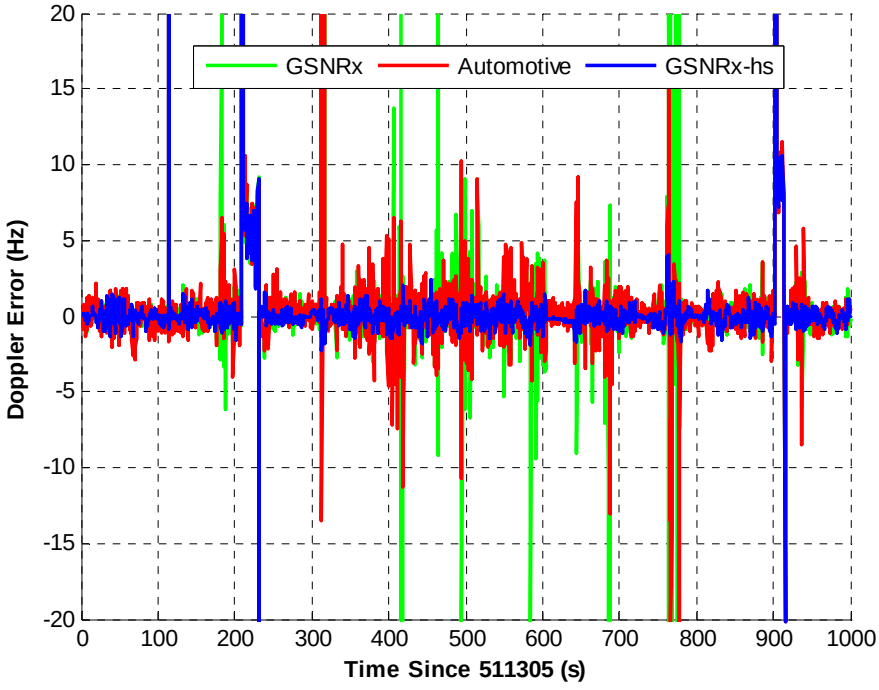

Figure 2.21: Doppler error of PRN 17 in the foliage test

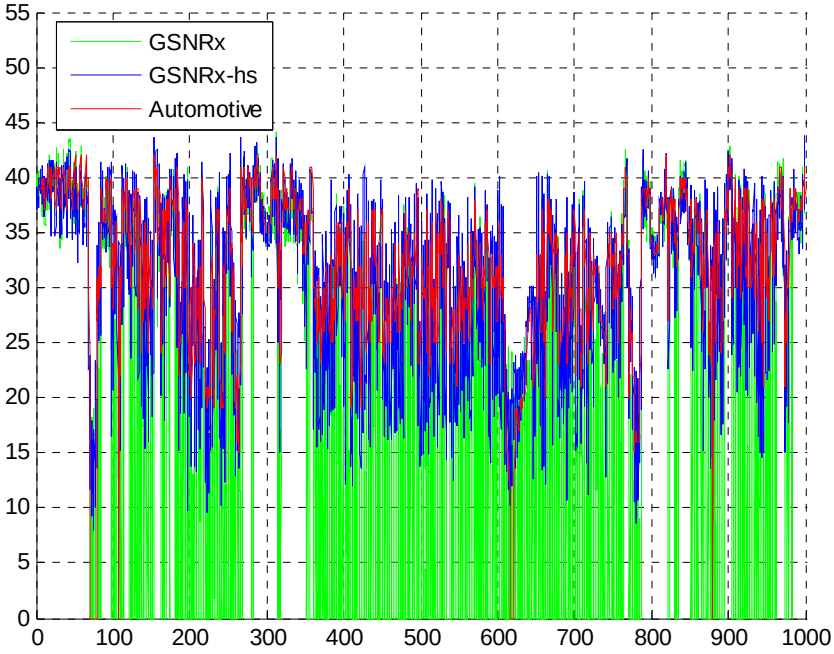

Figure 2.22: C/N_0 plots of PRN 32 in the suburban and foliage test

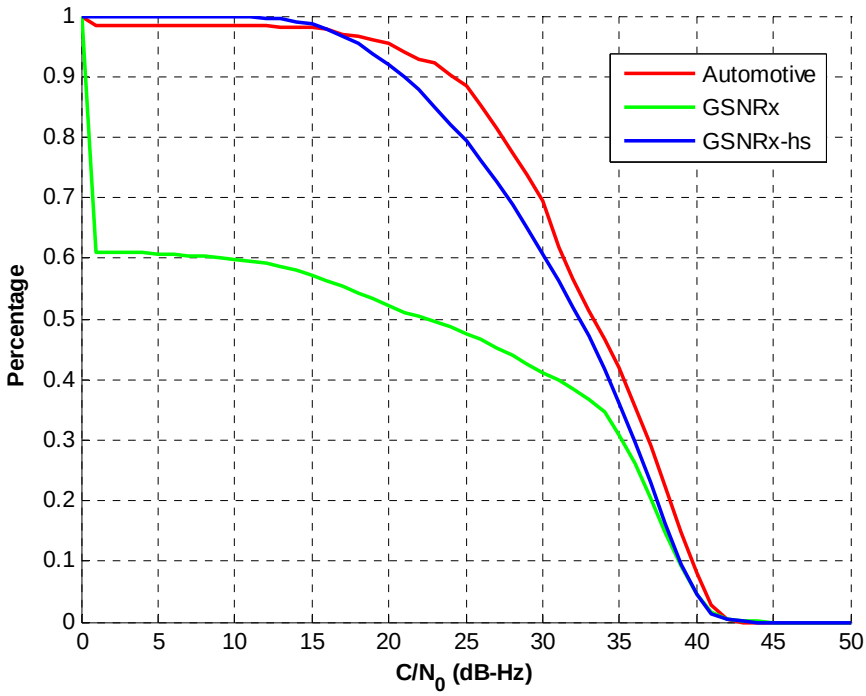

Figure 2.23: Cumulative C/N_0 plots of PRN 32 in the suburban and foliage test

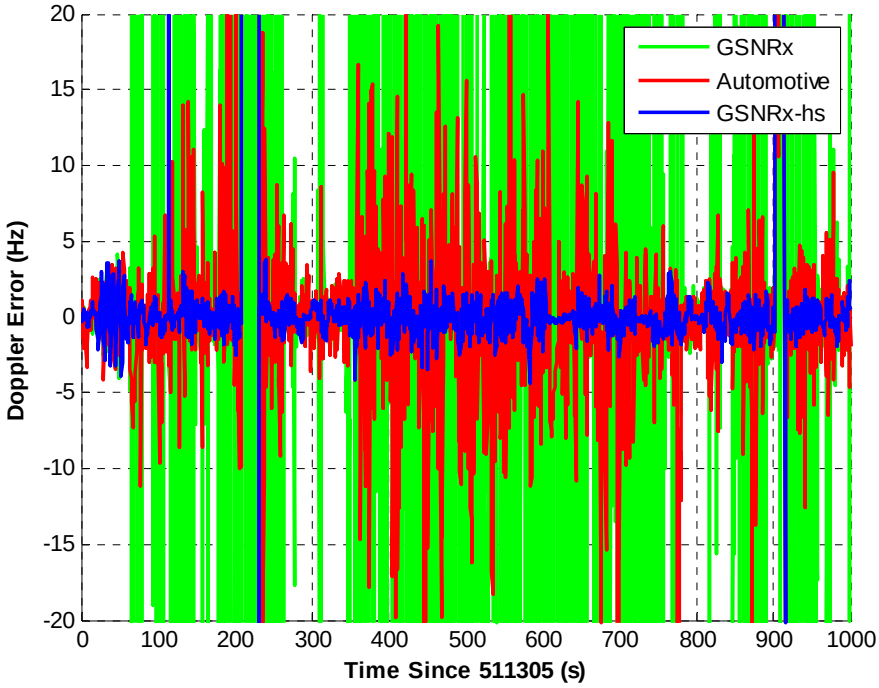

Figure 2.24: Doppler error of PRN 32 in the foliage test

Table 2.7: Summarized RMS Doppler errors with GPS only solutions in the suburban and foliage test

	PRN 17 (Hz)	PRN 32 (Hz)
Automotive	1.7	3.2
GSNRx™	67.5	51.7
GSNRx-hs™	1.2	1.0

Finally, Table 2.7 shows the summarized RMS Doppler error for both the high and low elevation angle satellites from the three GPS receivers.

2.4.2 Urban Canyon Scenario

Having evaluated the performance of GSNRx-hs™ under the suburban and foliage scenario, a similar analysis strategy is applied to assess the receiver's performance in an urban

canyon environment. A Similar equipment setup was used in the urban canyon test except for the sampling frequency of the GPS IF signals being 12.5 MHz (complex). Thus for the details of the equipment setup, refer to Section 2.4.1.1.

2.4.2.1 Test Environment

The urban canyon test was conducted in downtown Calgary. The test lasted about 30 minutes starting with a relatively open sky area. Figure 2.25 shows the test environment. For the test route selected, building heights are typically 30-40 stories on both sides of the road. Figure 2.26 and Figure 2.27 show the satellite sky plot and the test trajectory respectively. It is shown that there were ten satellites above the horizon during the test.

Figure 2.25: Urban canyon test environment

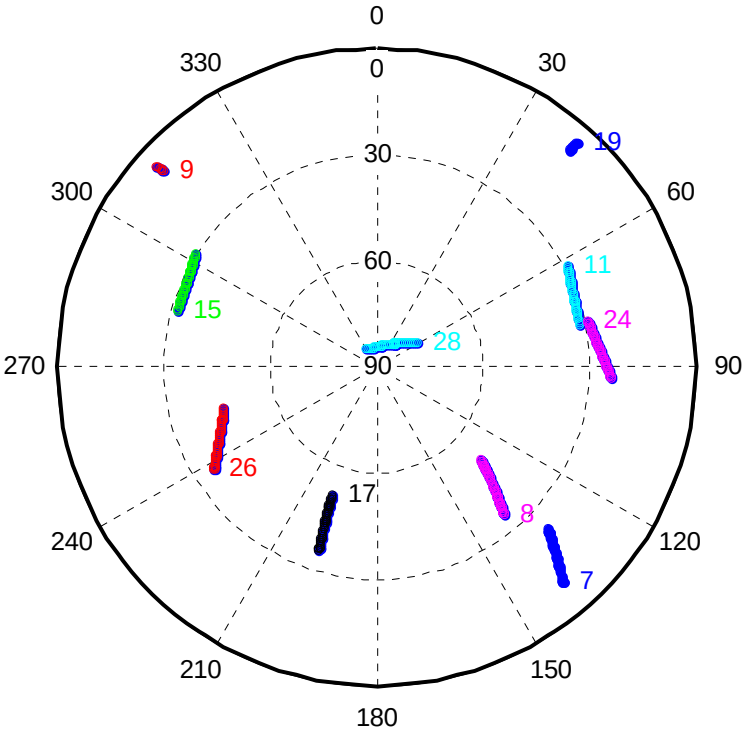

Figure 2.26: Satellite sky plot during the urban canyon test

Figure 2.27: Trajectory of the urban canyon test

2.4.2.2 Data Processing and Analysis Strategy

The same data processing strategy used for the urban canyon test as was used for the suburban and foliage test. The estimated accuracy of the reference solution (per axis) in this case is 0.5 m for position and 0.02 m/s for velocity. The attitude solution of the integrated system is accurate to about 0.20 degrees for pitch and roll, and 0.65 degrees for azimuth, which is considered sufficient for the analysis herein. The reference velocity and attitude plot are shown in Figure 2.28 and Figure 2.29. The maxim velocity is round 15 m/s. The vehicle's pitch and roll were within 5 degrees.

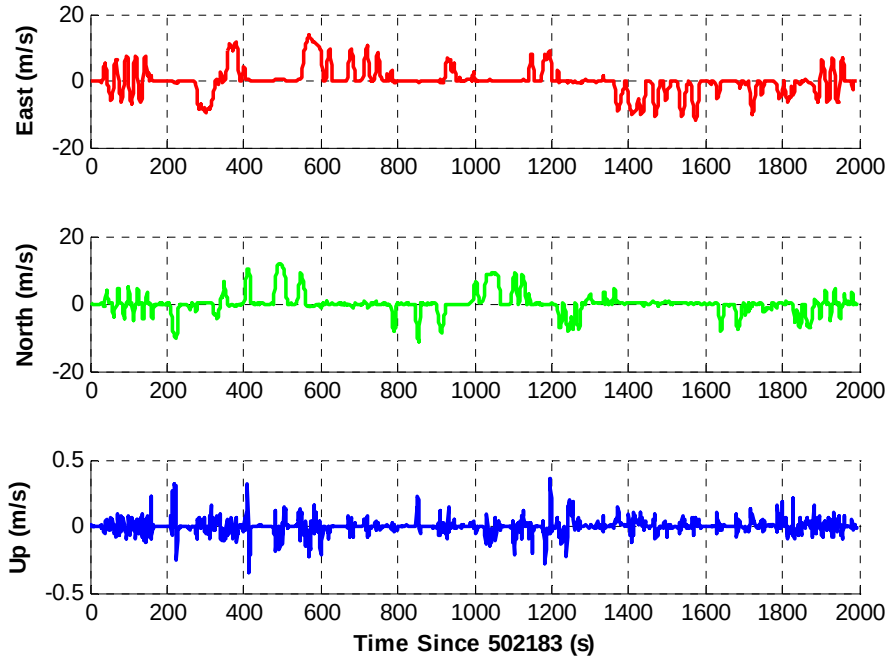

Figure 2.28: Reference velocity plot of the urban canyon test

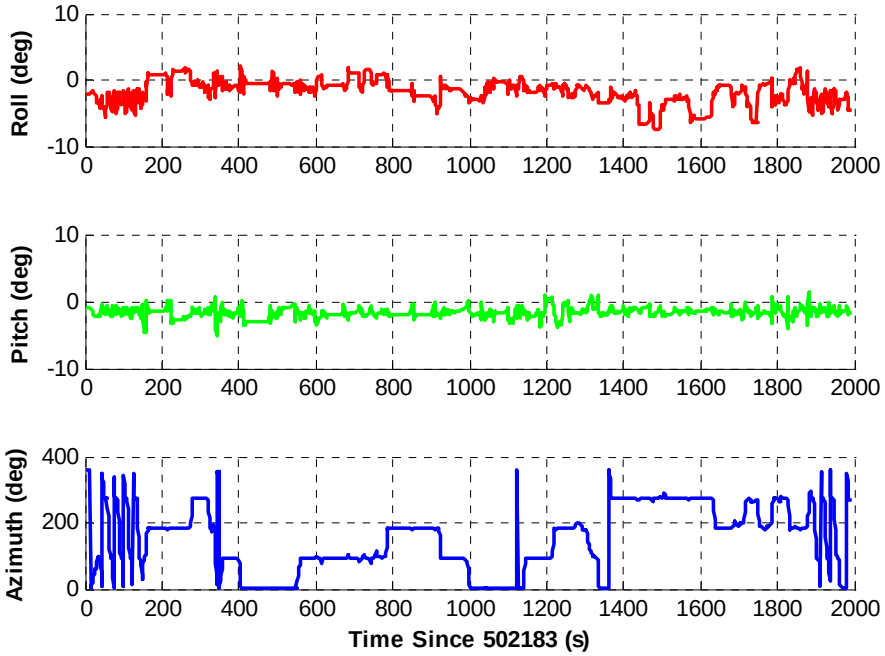

Figure 2.29: Reference attitude plot of the urban canyon test

Different coherent integration times and search space sizes were used for the processing to determine the optimum receiver parameter configuration under urban canyon environment. Furthermore, the same performance analysis strategy as the suburban and foliage test was used to evaluate the receiver's performance under urban canyon environment.

2.4.2.3 Position Domain Performance Analysis

A Similar positioning domain analysis as that for the suburban and foliage scenario is applied for the urban canyon case. The performances of the standard GSNRx^{TM}, the high sensitivity GSNRx-hs^{TM}, and the automotive grade GPS receiver are used for the analysis herein.

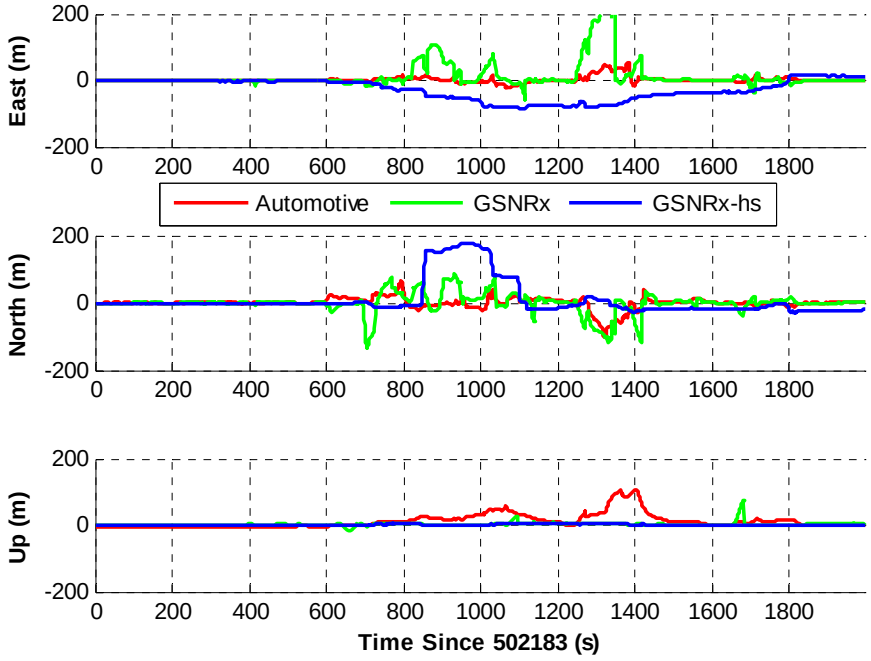

Figure 2.30: Position error plots for urban canyon test

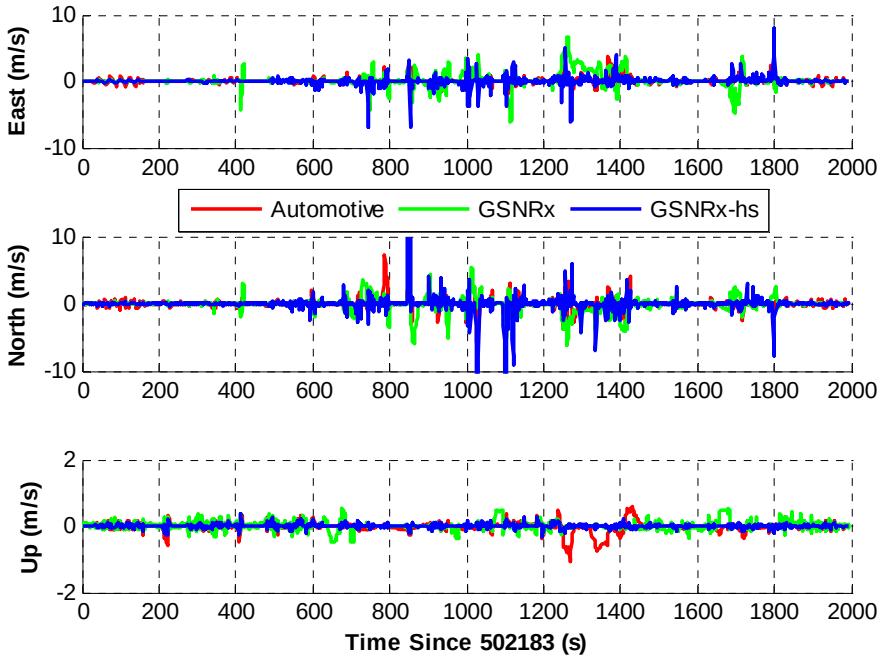

Figure 2.31: Velocity error plots for urban canyon test

Firstly, the analysis is performed in the position domain. The position and velocity error plots for all receivers in the urban canyon environment are shown in Figure 2.30 and Figure 2.31 respectively. It is noted that there were relatively large velocity and position error variations during the 600 – 1400 s interval. These variations are mainly due to signal degradation and multipath when the vehicle went into deep urban canyon area. In terms of positioning accuracy as shown in the two figures, both GSNRx^{TM} and GSNRx-hs^{TM} demonstrate poor performance compared to the automotive grade receiver in the downtown area. The problem with GSNRx^{TM} is insufficient tracking sensitivity to obtain the GPS measurements in such conditions. Although GSNRx-hs^{TM} applies over 100 ms coherent integration time, the navigation performance still does not show any improvement. It may be due to 1) the processing gain with 100 ms coherent integration being still inadequate to reliably keep track of weak signals in downtown areas, especially when signals are blocked by high surrounding buildings, and 2) biased GPS measurements due to multipath deteriorate the navigation solution.

Table 2.7 summarizes the RMS position and velocity errors for the automotive grade GPS receiver, GSNRx^{TM} and GSNRx-hs^{TM} in the urban canyon test. Due to the erroneous signal parameter estimates caused by the multipath or falsely detected correlation peaks being accepted by the navigation filter, positioning performance from the block processing are severely degraded.

Table 2.8: Summarized RMS position and velocity errors with GPS only solutions for the urban canyon test

	Position (m)			Velocity (m/s)		
	East	North	Up	East	North	Up
Automotive	9.6	17.1	25.3	0.50	0.84	0.16
GSNRx™	12.1	18.5	16.5	2.31	1.06	0.92
GSNRx-hs™	27.4	22.2	5.6	0.58	1.79	0.13

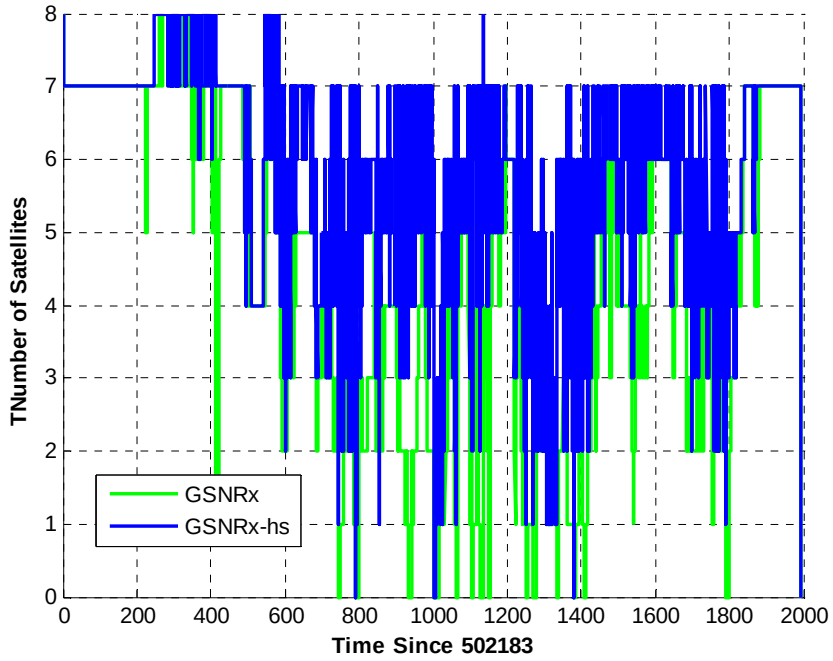

Figure 2.32: Number of satellites used in the navigation solution in the urban canyon test

Figure 2.32 shows the number of satellites used in the navigation solution for the urban canyon environment. Similar to the foliage case, GSNRx-hs™ outperforms GSNRx™ by using more measurements in the navigation solution, especially during the period 600-1800 s. However, the position accuracy of GSNRx-hs™ is still worse than GSNRx™

even with more measurements used in the navigation solution. It may result from the inclusion of multipath signal measurements in the navigation solution.

Table 2.9: Summarized RMS position and velocity errors as a function of a frequency search uncertainties for the urban canyon test

	Position (m)			Velocity (m/s)		
	East	North	Up	East	North	Up
2 m/s	33.4	75.6	35.1	0.70	2.21	0.13
4 m/s	27.4	22.2	5.6	0.58	1.79	0.13
6 m/s	37.4	35.6	5.8	0.71	1.80	0.13
8 m/s	38.9	44.1	6.9	0.92	2.13	0.13

In order to analyze navigation performance as a function of the search space for the high sensitivity block processing receiver, post-processing results using different search spaces are examined. To begin with the analysis, navigation performance using different frequency uncertainties is evaluated. Table 2.8 summarizes the RMS position and velocity errors as a function of the various frequency search space in the urban canyon test. As listed in this table, GSNRx-hs^{TM} using a 4 m/s frequency uncertainty offers the best position and velocity accuracy. By either increasing or decreasing the frequency search space, the navigation performance drops. The reason is that the frequency search space should be sufficient large to tolerate the relatively large navigation errors to maintain reliable tracking when using vector feedback in degraded signal environment. Also, the larger search space the higher the possibility to include multipath in the navigation solution, which could degrade the solution. In this case, a 4 m/s frequency uncertainty provides the best results.

A similar analysis strategy can be used for the navigation performance as the function of the range uncertainty. The range uncertainties used for the processing were 150 m, 300 m and 450 m with a step size of 25 m. The coherent integration time and the frequency uncertainty are still 100 ms and 4 m/s respectively. Similar conclusions can be drawn as for the frequency uncertainty analysis, namely that either too large or too small range uncertainties decrease the position and velocity accuracy, especially the position accuracy. Therefore, a 300 m range uncertainty is appropriate in this test scenario.

Table 2.10: Summarized RMS position and velocity errors as a function of the range search uncertainties for the suburban and foliage test

	Position (m)			Velocity (m/s)		
	East	North	Up	East	North	Up
150 m	35.4	41.2	5.6	0.60	1.91	0.13
300 m	27.4	22.2	5.6	0.58	1.79	0.13
450 m	32.1	34.9	5.9	0.54	1.73	0.13

Finally, navigation performance as a function of coherent integration time is presented. Three sets of coherent integration time namely 20 ms, 50 ms and 100 ms are used for the analysis. The 300 m and 8 m/s range and frequency uncertainty were applied in this case. Table 2.10 lists the positioning errors as a function of coherent integration time. As shown in this table, the higher the coherent integration time, the better the navigation performance.

Table 2.11: Summarized RMS position and velocity errors as a function of coherent integration time for the urban canyon test

	Position (m)			Velocity (m/s)		
	East	North	Up	East	North	Up
20 ms	47.7	69.3	8.9	2.31	2.44	0.13
50 ms	40.9	46.1	8.9	2.11	2.34	0.13
100 ms	38.9	44.1	6.9	0.92	2.13	0.13

In summary, GSNRx-hs^{TM} has worse performance compared with the automotive grade GPS receiver and the standard GSNRx^{TM} in this test environment even with a 100 ms coherent integration time. It may due to the inclusion of strong multipath peaks in the navigation solution. Because of poor positioning accuracy, larger search space should be used to avoid missing correlation peaks. However, it also increases the possibility to include multipath peaks in the navigation solution.

2.4.2.4 Tracking Domain Performance Analysis

Having discussed the performance of the three GPS receivers in the navigation domain, the tracking performance is now analyzed in terms of tracked C/N_0 values. Figure 2.33 shows the estimated C/N_0 plots of a high elevation satellite PRN 28 (85 deg) from different receivers. Similar C/N_0 estimates from the three receivers were obtained which indicates that the three receivers have similar C/N_0 estimation performance for the high elevation satellite, which can be more clearly observed in Figure 2.34.

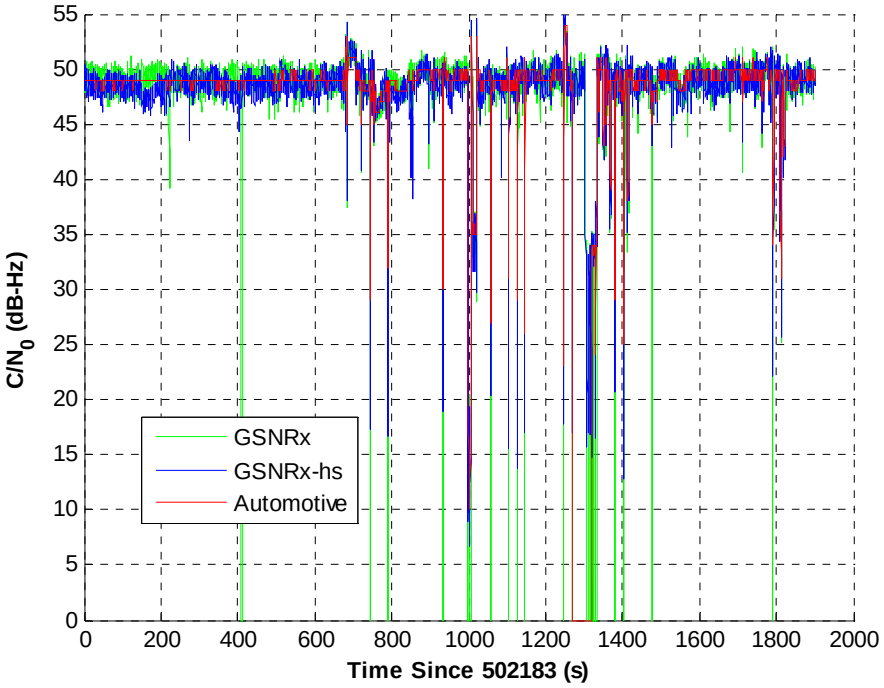

Figure 2.33: C/N_0 plots of PRN 28 in the urban canyon test

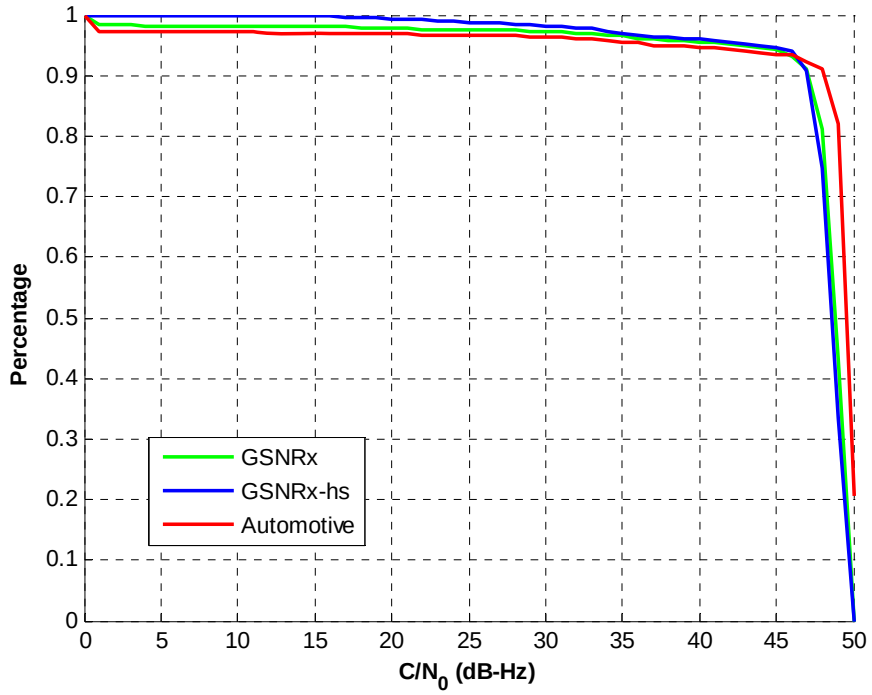

Figure 2.34: Cumulative C/N_0 plots of PRN 28 in the urban canyon test

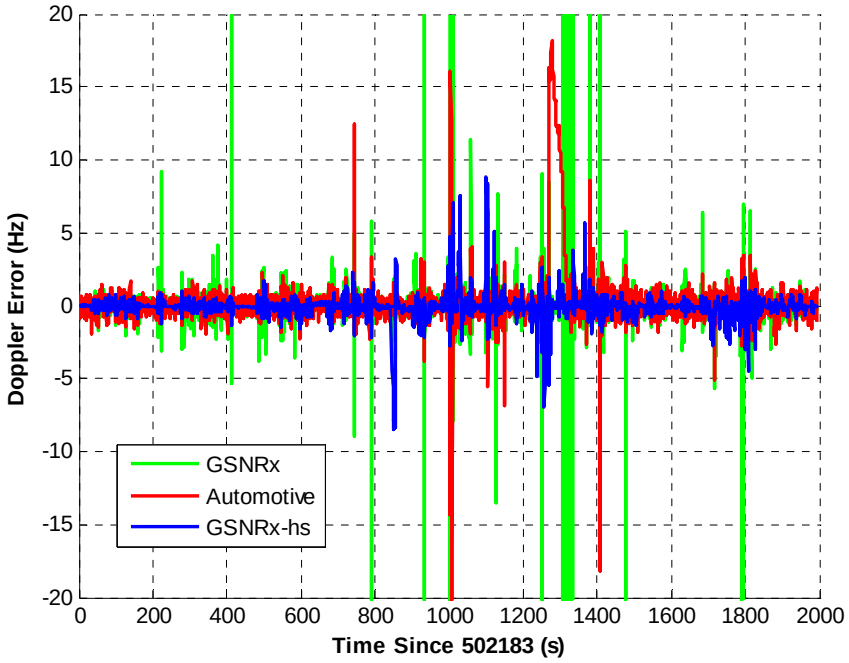

Figure 2.35: Doppler error of PRN 28 in the urban canyon test

Figure 2.35 shows the Doppler error of PRN 28 from the automotive grade HSGPS receiver, GSNRx™ and GSNRx-hs™. The Doppler error spikes shown in this plot indicate losses of carrier tracking lock. Thus, GSNRx™ shows frequently losses of lock in this test scenario. GSNRx-hs™ provides the best performance with a RMS Doppler error of 0.9 Hz as listed in Table 2.12, which is 1.4 Hz better compared to that of the automotive grade HSGPS receiver.

Figure 2.36 shows the estimated C/N_0 plots of a low elevation satellite PRN 24 (28 deg) from different receivers. In this case, GSNRx-hs™ and the automotive grade HSGPS receiver have similar tracking performance. However standard GSNRx™ receiver does not have sufficient sensitivity to keep tracking PRN 24 in this case.

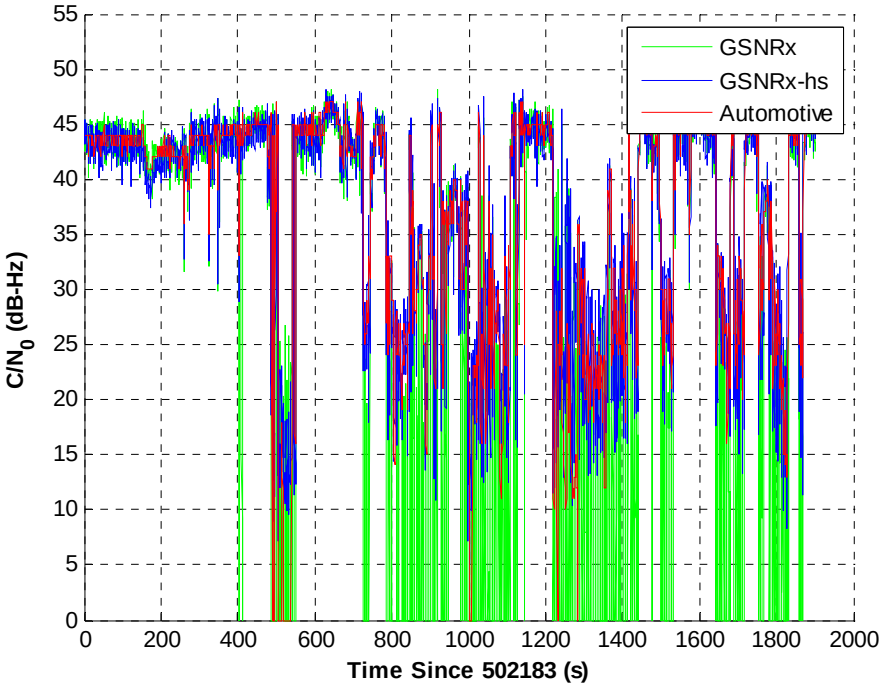

Figure 2.36: C/N_0 plots of PRN 24 in the urban canyon test

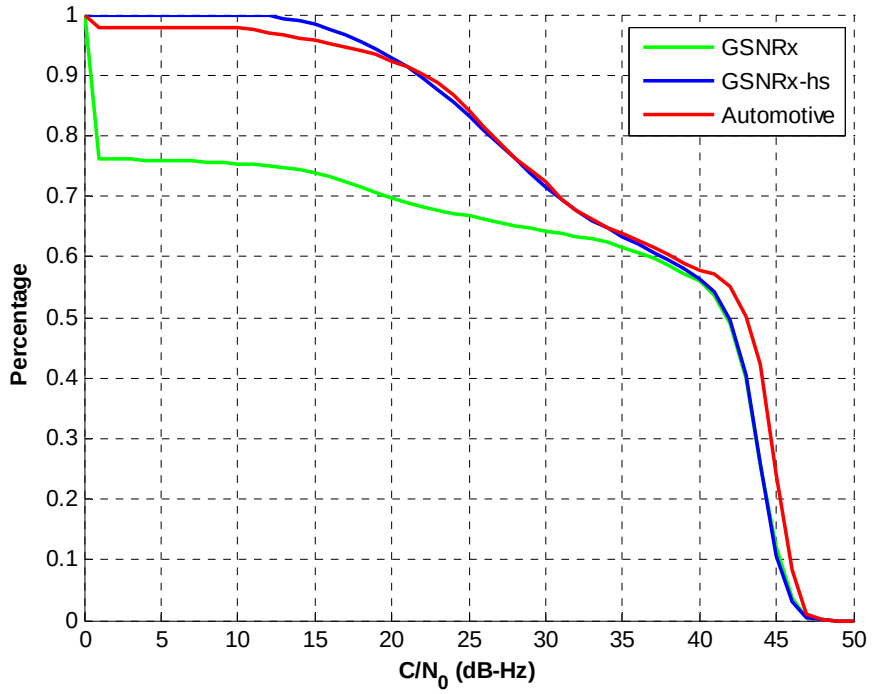

Figure 2.37: Cumulative C/N_0 plots of PRN 24 in the urban canyon test

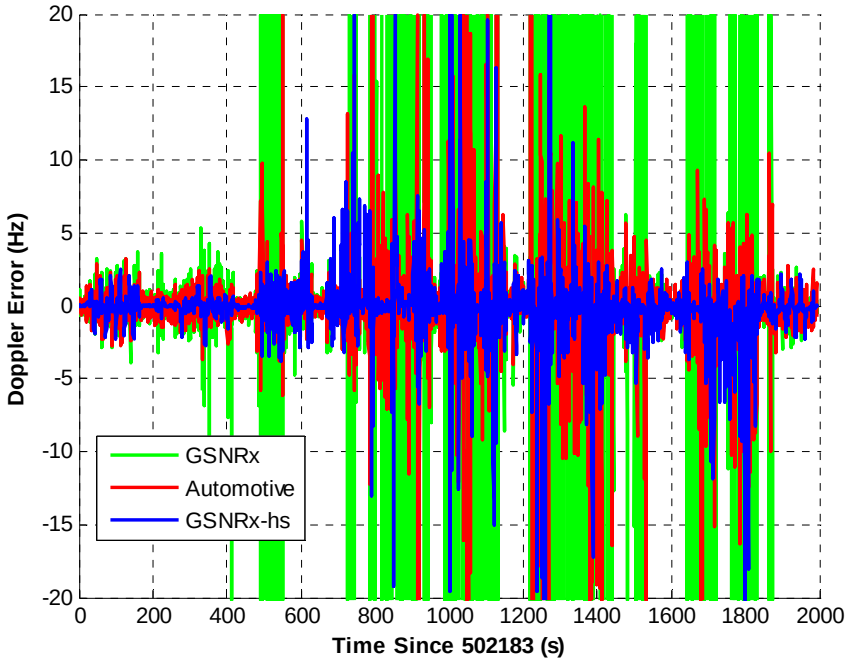

Figure 2.38: Doppler error of PRN 24 in the urban canyon test

Figure 2.38 shows the Doppler error plot for the low elevation satellite PRN 24. Compared to PRN 28, larger Doppler error variations for the three receivers are observed in this figure. Still, GSNRx-hs™ provides the best performance with a RMS Doppler error of 2.9 Hz, which is a 2 Hz improvement compared with the automotive grade HSGPS receiver. GSNRx™ cannot track this satellite during most of the time, as indicated by the large variations of Doppler errors.

Table 2.12: Summarized RMS Doppler errors with GPS only solutions in the urban canyon test

	PRN 28 (Hz)	PRN 24 (Hz)
Automotive	2.3	5.9
GSNRx™	25.7	107.3
GSNRx-hs™	0.9	2.9

In summary, GSNRx-hs™ has similar C/N_0 estimates but improved Doppler estimation performance as that of the automotive grade GPS receiver in this test scenario. Furthermore, GSNRx-hs™ outperforms the standard GSNRx™ as indicated by more reliable C/N_0 estimates and smaller Doppler error. However, the improved tracking performance does not lead to a better navigation accuracy. The degraded positioning may be caused by the inclusion of multipath peaks in the signal parameter estimation (Xie & Petovello 2011). However, the multipath identification and removal in the block processing is beyond the scope of the thesis.

CHAPTER THREE: GPS/VEHICLE SENSOR INTEGRATION USING DEAD RECKONING

As discussed in the previous chapter, the standalone HSGPS receiver using block processing technique cannot provide sufficient sensitivity to achieve five metre positioning accuracy in the urban canyon scenario. Therefore, the vehicle sensors should be used to provide aiding information to improve the positioning performance under degraded signal environments.

To apply measurements from vehicle sensors to navigation, mainly two categories of algorithms are commonly used, namely DR based and INS mechanization based. This chapter introduces both of the algorithms but with the focus on the DR based methods. The chapter starts with the DR based algorithms. Given the various vehicle sensor configurations used in modern vehicles nowadays, a discussion on vehicle sensor configurations is presented first. Then the proposed DR algorithms based on different sensor configurations are presented. Having introduced the DR based algorithms, the INS mechanization based algorithms are briefly described which are mainly used for the performance comparison. Following the theoretical algorithm development, field test results are used to analyze the performance of the GPS/DR based integration system under different environments. Results from both the DR and the INS mechanization based approaches are compared and analyzed in terms of the positioning and attitude accuracy.

3.1 Dead-Reckoning Based Algorithms

The DR based algorithms are introduced in this section. Because of the various vehicle sensor configurations, the DR algorithms should be varied corresponding to the different sensor configurations.

Unlike the INS mechanization approach where the vehicle sensors drive the system via INS mechanizations, the DR algorithms proposed here use the vehicle sensors as measurements to update the system. Therefore, the measurements from different vehicle sensors can be separately used in the system. This approach improves the flexibility and the robustness of the system via encapsulating different vehicle sensor updates into separate modules. In this case, if one vehicle sensor encounters failures, it can be easily identified and excluded from the system.

In addition, this implementation allows the measurement models to vary according to the vehicle sensor configurations whereas the system models remain similar for each sensor setup except for the inclusion of the corresponding sensor error terms (e.g. bias, scale factor and drift).

3.1.1 Vehicle Sensor Configurations

Different models of vehicles are usually equipped with different vehicle sensor setups, thus, the proposed DR algorithms in this chapter are based on five commonly used vehicle sensor configurations, namely:

- the rear wheel speed sensor (RWSS) only setup,

- the rear wheel speed sensor and yaw rate sensor (RWSS/YRS) setup,
- the rear wheel speed sensor, single longitudinal accelerometer and yaw rate sensor (RWSS/1A1G) setup,
- the front and rear wheel speed sensor, steering angle sensor, single longitudinal accelerometer and yaw rate sensor setup (WSS/SAS/1A1G)
- and the front and rear wheel speed sensor, steering angle sensor, two horizontal longitudinal accelerometers and yaw rate sensor setup (WSS/SAS/2A1G).

The RWSS only setup is the simplest sensor configuration. In this case, only rear left and right wheel speed sensors' measurements are used to update the integrated navigation filter. These measurements contain both the longitudinal vehicle velocity and the yaw rate information. It is noted that the wheel speed is corrupted by noise and scale factor errors. These scale factors errors are mainly induced by the varying tire radius and thus should be taken into consideration in the algorithm development. The details of the system and measurement models will be presented in Section 3.1.3.

Compared with the RWSS sensor setup, the RWSS/YRS uses additional measurements from the YRS to update the navigation solution. Since the wheel slips of the wheel speed sensors often severely deteriorate the vehicle velocity and yaw rate estimates, especially when GPS updates are not available, the error of the vehicle azimuth accumulates quickly because of the integration of the erroneous yaw rate estimates. Thus the positioning performance would degrade accordingly in this case. However, the YRS provides additional information about the yaw rate and can be used to update the navigation solution

in addition to the RWSS. It improves the yaw rate estimates and helps to identify the wheel slips. Therefore, the RWSS/YRS setup offers improved navigation performance compared with the RWSS only setup. The details will be presented in Section 3.1.4

In addition to the RWSS and YRS measurements, the RWSS/1A1G setup applies the longitudinal accelerometer measurements to estimate the pitch, which is neglected or cannot be estimated without GPS updates for the previous two sensor setups. Therefore the pitch dynamics can be compensated with this sensor setup. It implicitly improves the navigation performance especially when the vehicle is running on un-levelling roads or going up and down hills. More details about this algorithm development will be introduced in Section 3.1.5.

The above sensor configurations include only the rear WSS in their sensor setups. However, the front WSS can also provide the velocity and the yaw rate information. The sensor redundancy could improve the reliability of the system. In order to use front WSS, the SAS should be used to compensate for the front wheel steering angles. Therefore, the WSS/SAS/1A1G setup uses the measurements from all the four WSS to update navigation filter. More Details will be presented in Section 3.1.6.

The WSS/SAS/2A1G sensor setup includes the additional lateral accelerometer compared with WSS/SAS/1A1G. Information from the lateral accelerometer could provide the estimates of the lateral velocity and thus information about the roll angle of the vehicle. The compensated lateral vehicle dynamics and roll dynamics would improve the navigation

performance accordingly. More details about the algorithm development will be introduced in Section 3.1.7.

3.1.2 Simplified Four Wheel Vehicle Model

In order to effectively form the measurement update equations using vehicle sensors, a four-wheel vehicle model is introduced for the simplicity. Figure 2.3 shows the simplified four-wheel vehicle model. M is located at the center of the real axle, which is also the point of interest to generate positioning information of the vehicle for the DR algorithm; e represents half of the wheel track; L represents the wheel base; ψ_c is the steering angle of the virtual front wheel; and ψ_l, ψ_r are the left and right wheel angles, respectively.

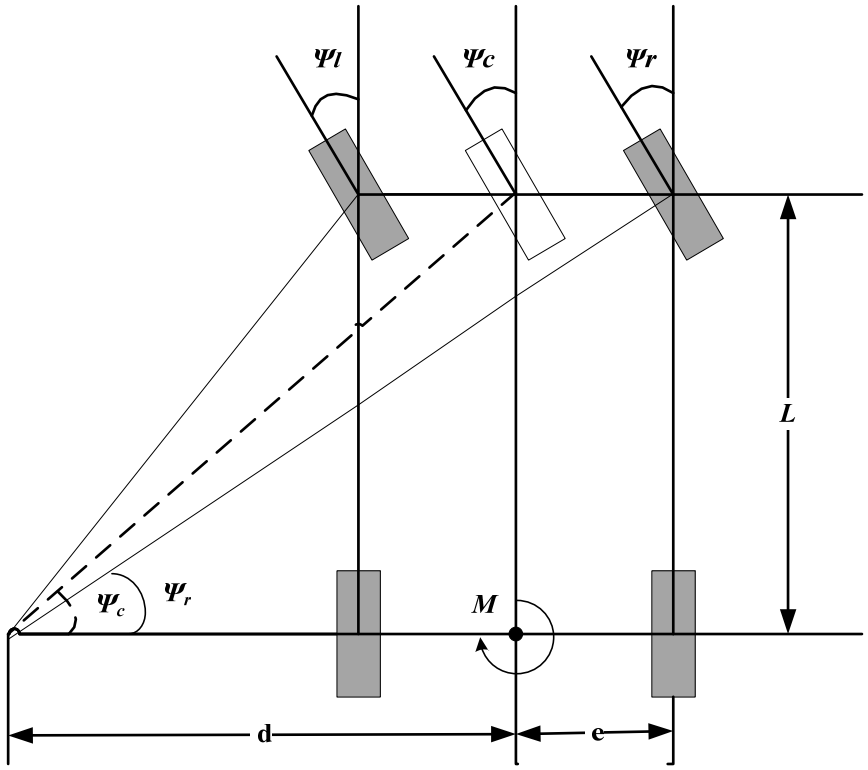

Figure 3.1: Simplified four wheel vehicle model

Differential odometry techniques (Bonnifait et al 2001, Sasse et al 2009) can be used to derive the relationship between the four wheel speeds and the forward velocity and yaw rate of the vehicle, which can be expressed as

$$\begin{aligned} V_{rl} &= V_y^b + e\dot{\psi} \\ V_{rr} &= V_y^b - e\dot{\psi} \\ V_{fl}\cos\psi_l &= V_y^b + e\dot{\psi} \\ V_{fr}\cos\psi_r &= V_y^b - e\dot{\psi} \end{aligned} \qquad 3.1$$

where V_{rl}, V_{rr}, V_{fl} and V_{fr} are the rear left, rear right, front left and front right wheel speed respectively; V_y^b is the longitudinal velocity in the body frame; $\dot{\psi}$ is the yaw rate in the body frame, which is defined as clockwise positive. For details of the body frame definition refer to Appendix A. ψ_l, ψ_r can be obtained using the following equations.

$$\psi_l = \begin{cases} \tan^{-1}\dfrac{L}{d-e} & (\psi_l < 0) \\ \tan^{-1}\dfrac{L}{d+e} & (\psi_l \geq 0) \end{cases} \qquad 3.2$$

$$\psi_r = \begin{cases} \tan^{-1}\dfrac{L}{d+e} & (\psi_r < 0) \\ \tan^{-1}\dfrac{L}{d-e} & (\psi_r \geq 0) \end{cases} \qquad 3.3$$

It is noted that ψ_l and ψ_r are both clockwise positive. The negative angles of ψ_l and ψ_r indicate the front wheels turning left whereas the positive angles indicate them turning right. The L, d and e are all positive scalars. L and e can be easily obtained from the specifications of the vehicle. d can be computed as

$$d = \frac{L}{\tan|\psi_c|} \tag{3.4}$$

where ψ_c is the steering ratio scaled SAS outputs. $|X|$ indicates the magnitude of X.

Combining Equation (3.2), (3.3) and (3.4), ψ_l, ψ_r can be given by

$$\psi_l = \frac{L \cdot \tan|\psi_c|}{L + e \cdot \tan\psi_c}$$
$$\psi_r = \frac{L \cdot \tan|\psi_c|}{L - e \cdot \tan\psi_c} \tag{3.5}$$

3.1.3 RWSS Setup

RWSS is the simplest sensor configuration using only measurements form the rear wheel speed sensors in the navigation solution. The details of the system and measurement model for this sensor setup are presented in this section.

3.1.3.1 System Model

Eight states are used to represent the system, namely three dimensional position error $\delta\mathbf{r}^n$ in east, north and vertical ("up") directions (δr_E ; δr_N ; δr_U), the longitudinal velocity error in the body frame δV_y^b, the longitudinal acceleration error δa_y^b, pitch error $\delta\theta$, azimuth error $\delta\psi$, yaw rate error $\delta\dot{\psi}$, rear left wheel scale factor error δS_{rl} and rear right wheel scale factor error δS_{rr}. The system error states $\mathbf{dx}$ are given by

$$\mathbf{dx} = \begin{bmatrix} \delta r_E & \delta r_N & \delta r_U & \delta V_y^b & \delta a_y^b & \delta\theta & \delta\psi & \delta\dot{\psi} & \delta S_{rl} & \delta S_{rr} \end{bmatrix}^T \tag{3.6}$$

$\delta\mathbf{r}^n$ is directly related with velocity error vector $\delta\mathbf{v}^n$ in the navigation frame as

$$\begin{bmatrix} \delta\dot{r}_E \\ \delta\dot{r}_N \\ \delta\dot{r}_U \end{bmatrix} = \delta\mathbf{V}^n = \begin{bmatrix} \delta V_E^n \\ \delta V_N^n \\ \delta V_U^n \end{bmatrix} \tag{3.7}$$

Since the body frame velocity can be rotated into the navigation frame which is defined in Appendix A by the rotation matrix R_b^n, which is given by

$$\mathbf{V}^n = R_b^n \mathbf{V}^b = R_b^n \begin{bmatrix} 0 \\ V_y^b \\ 0 \end{bmatrix} = \begin{bmatrix} \cos\psi & \sin\psi & 0 \\ -\sin\psi & \cos\psi & 0 \\ 0 & 0 & 1 \end{bmatrix} \begin{bmatrix} 1 & 0 & 0 \\ 0 & \cos\theta & -\sin\theta \\ 0 & \sin\theta & \cos\theta \end{bmatrix} \begin{bmatrix} 0 \\ V_y^b \\ 0 \end{bmatrix} \tag{3.8}$$

It is noted that the roll angle is neglected in R_b^n because of the typically small roll angle in the land vehicle navigation. In addition, the non-holonomic constraints of the vehicle with the lateral and vertical velocities being assumed as zeros are applied.

Thus the velocity error can be obtained by differentiating Equation (3.8) as

$$\delta\mathbf{V}^n = \begin{bmatrix} \delta V_y^b \sin\psi\cos\theta + \delta V_y^b \cos\psi\cos\theta\delta\psi - V_y^b \sin\psi\sin\theta\delta\theta \\ \delta V_y^b \cos\psi\cos\theta - \delta V_y^b \sin\psi\cos\theta\delta\psi - V_y^b \cos\psi\sin\theta\delta\theta \\ \delta V_y^b \sin\theta + V_y^b \cos\theta\delta\theta \end{bmatrix} \tag{3.9}$$

Substituting Equation (3.8) into (3.7), the position error can be derived as

$$\begin{bmatrix} \delta\dot{r}_E \\ \delta\dot{r}_N \\ \delta\dot{r}_U \end{bmatrix} = \begin{bmatrix} \sin\psi\cos\theta & V_y^b \cos\psi\cos\theta & -V_y^b \sin\psi\sin\theta \\ \cos\psi\cos\theta & -V_y^b \sin\psi\cos\theta & -V_y^b \cos\psi\sin\theta \\ \sin\theta & 0 & V_y^b \cos\theta \end{bmatrix} \begin{bmatrix} \delta V_y^b \\ \delta\psi \\ \delta\theta \end{bmatrix} \tag{3.10}$$

The longitudinal velocity and acceleration error can be expressed as:

$$\begin{bmatrix} \delta\dot{V}_y^b \\ \delta\dot{a}_y^b \end{bmatrix} = \begin{bmatrix} 0 & 1 \\ 0 & 0 \end{bmatrix} \begin{bmatrix} \delta V_y^b \\ \delta a_y^b \end{bmatrix} + \begin{bmatrix} 0 \\ w_a \end{bmatrix} \tag{3.11}$$

where the acceleration is modeled as random walk with the driving noise w_a in units of $m/s^3/\sqrt{Hz}$.

With the pitch being estimated with this sensor setup, the error of yaw rate error $\delta\dot{\psi}$ can be rewritten to include the pitch compensation as

$$\begin{bmatrix} \delta\dot{\psi} \\ \delta\ddot{\psi} \\ \delta\dot{\theta} \end{bmatrix} = \begin{bmatrix} 0 & \frac{1}{\cos\theta} & \frac{\sin\theta}{\cos^2\theta} \\ 0 & 0 & 0 \\ 0 & 0 & -\alpha_\theta \end{bmatrix} \begin{bmatrix} \delta\psi \\ \delta\dot{\psi} \\ \delta\theta \end{bmatrix} + \begin{bmatrix} 0 \\ w_\omega \\ w_\theta \end{bmatrix} \tag{3.12}$$

where the azimuth error is modeled as a random walk, the pitch dynamic is modeled as first order Gauss-Markov process (Sun et al 2008) . w_ω is the driving noise of the azimuth random walk; α_θ and w_θ are the reciprocal correlation time and the driving noise of the pitch Gauss-Markov process. It is noted that the pitch can be estimated only when GPS updates are available in this sensor setup.

The scale factor errors of the rear left and right WSS are modeled as the first order Gauss Markov processes. The details of first order Gauss-Markov process can be found in Appendix B.

3.1.3.2 Measurement Model

For the RWSS sensor setup, only rear wheel speeds are used to update the navigation filter. The measurement misclosure is given by

$$\delta \mathbf{Z}_{RWSS} = \begin{bmatrix} \hat{V}_y^b + e\hat{\dot{\psi}} \\ \hat{V}_y^b - e\hat{\dot{\psi}} \end{bmatrix} - \begin{bmatrix} V_{rl} \\ V_{rr} \end{bmatrix} \tag{3.13}$$

where $\hat{X}$ represents the estimated value of X . Correspondingly $\hat{V}_y^b$ and $\hat{\dot{\psi}}$ are the predicted forward velocity and yaw rate propagated from the last estimates. V_{rl} and V_{rr} are the scale factor-compensated rear left and right wheel speed respectively. The raw outputs of RWSS $\widetilde{V}_{rl,rr}$ can be modeled as

$$\widetilde{V}_{rl,rr} = (1 + S_{rl,rr})V_{rl,rr} + v_{rl,rr} \tag{3.14}$$

where $v_{rl,rr}$ is the wideband noise of the rear left/right WSS in unit of m/s. Finally, the measurement equation for the RWSS updates is given by

$$\delta \mathbf{Z}_{RWSS} = \mathbf{H}_{RWSS}\mathbf{dX} + \mathbf{v}_{RWSS,2\times 1} \tag{3.15}$$

where $\mathbf{v}_{RWSS,2\times 1}$ is measurement noise vector. $\mathbf{H}_{RWSS}$ is the design matrix for the RWSS updates, and is expressed as

$$\mathbf{H}_{RWSS} = \begin{bmatrix} 0_{3\times 1} & 1 & 0_{3\times 1} & e & -V_{rl} & 0 \\ 0_{3\times 1} & 1 & 0_{3\times 1} & -e & 0 & -V_{rr} \end{bmatrix} \tag{3.16}$$

The measurement noise matrix $\mathbf{R}_{RWSS}$ for the RWSS is simply as follows:

$$\mathbf{R}_{RWSS} = \begin{bmatrix} \sigma_{rl}^2 & 0 \\ 0 & \sigma_{rr}^2 \end{bmatrix} \tag{3.17}$$

where σ_{rl}^2 and σ_{rr}^2 are the variance of wideband noise for the rear left and right wheel speeds.

3.1.4 RWSS/YRS Setup

Compared with the RWSS only setup, the RWSS/YRS sensor setup uses the YRS measurements to improve the yaw rate estimates of the vehicle. Since the YRS outputs are corrupted by drift and noise, the additional YRS drift state is introduced in the system error states.

3.1.4.1 System Model

The system states of the RWSS/YRS setup augmented with YRS drift d_{YRS} are given by

$$\mathbf{dx} = \begin{bmatrix} \delta r_E & \delta r_N & \delta r_U & \delta V_y^b & \delta a_y^b & \delta\theta & \delta\psi & \delta\dot{\psi} & d_{YRS} & \delta S_{rl} & \delta S_{rr} \end{bmatrix}^T \quad 3.18$$

where d_{YRS} is modeled as a first order Gauss-Markov process. The reciprocal correlation time and the variance of the process can be determined using Allan Variance of the YRS's outputs. The other states of the RWSS/YRS remain the same as those of the RWSS.

3.1.4.2 Measurement Model

When using YRS measurements to update the navigation filter, the difference between the estimated yaw rate and the YRS outputs is used as the measurement misclosure $\delta\mathbf{Z}_{YRS}$, which is expressed as

$$\delta\mathbf{Z}_{YRS} = \hat{\dot{\psi}} + \omega_{ibz}^b \quad 3.19$$

where ω_{ibz}^b is the drift-compensated YRS outputs, which can be obtained by

$$\omega_{ibz}^{b} = \tilde{\omega}_{ibz}^{b} - d_{YRS} \tag{3.20}$$

where $\tilde{\omega}_{ibz}^{b}$ is the raw YRS output. It is noted that the different sign conventions of YRS outputs and the yaw rate of the vehicle lead to the "+" rather than "-" in Equation (3.19). The yaw rate of the vehicle is clockwise positive defined whereas the YRS outputs are counter clockwise positive. Furthermore, Equation (3.19) is derived based on the small pitch and roll angle assumption, which is usually valid during normal driving conditions..

Finally the measurement equation for the YRS updates is expressed as

$$\delta \mathbf{Z}_{YRS} = \mathbf{H}_{YRS}\mathbf{dx} + v_{YRS} \tag{3.21}$$

where v_{YRS} is the wideband noise of YRS. The design matrix of the YRS updates is given by

$$\mathbf{H}_{YRS} = \begin{bmatrix} 0_{1\times 7} & 1 & -1 & 0_{1\times 2} \end{bmatrix} \tag{3.22}$$

The measurement noise matrix $\mathbf{R}_{YRS}$ for the YRS is given by

$$R_{YRS} = \sigma_{YRS}^{2} \tag{3.23}$$

where σ_{YRS}^{2} is the variance of wideband noise for the YRS.

3.1.5 RWSS/1A1G

The RWSS/1A1G sensor setup includes rear WSS, one longitudinal accelerometer and one vertical gyro (yaw rate sensor). Since a longitudinal accelerometer is used in the sensor configuration, the pitch angle can be estimated without GPS updates. When using the

measurements from the accelerometer, the in-run bias of the sensor should be taken into consideration. Thus the accelerometer bias should be added into the system states.

3.1.5.1 System Model

With the longitudinal accelerometer bias b_y considered in the system states, the system error states can be expressed as

$$\mathbf{dx} = \begin{bmatrix} \delta\mathbf{r}^n & \delta V_y^b & \delta a_y^b & \delta\theta & \delta\psi & \delta\dot{\psi} & b_y & d_{YRS} & \delta S_{rl} & \delta S_{rr} \end{bmatrix}^T \quad 3.24$$

The system model remains the same as that in the RWSS/YRS setup. The longitudinal accelerometer bias b_y is also modeled as a first order Gauss-Markov process.

3.1.5.2 Measurement Model

The measurement equations for the RWSS and YRS updates are the same as in the RWSS/YRS sensor setup. Thus the focus here is on the filter update using accelerometer measurements.

Unlike the traditional INS mechanization based approach, the accelerometer outputs are used to generate pseudo-pitch measurements for the navigation updates rather than to generate velocity information. Such implementation avoids the accumulated error resulting from integrating the biased accelerometer outputs. The pseudo-pitch can be obtained using the wheel speed sensor derived acceleration and the longitudinal accelerometer's measurements. The details of the derivation are as follows.

Using the kinematic relationship between the IMU outputs and the derivatives of the Euler angles, and assuming that the rotation rate of the earth is negligible, the longitudinal acceleration can be written as (Tseng et al 2007)

$$a_y^b = f_y + \dot{\psi} \cdot V_x^b - |g| \sin\theta \qquad 3.25$$

where

f_y is the accelerometer sensed acceleration;

V_x^b is the lateral velocity of the vehicle in the body frame;

$|g|$ is the magnitude of the local gravity vector in the body frame.

Thus, the pitch angle θ can be obtained by using the following equation:

$$\theta = \sin^{-1} \frac{f_y - b_y - a_y^b + \dot{\psi} V_x^b}{|g|} \qquad 3.26$$

Since V_x^b is not available for the current sensor setup, it cannot be obtained directly. However, during the normal vehicle maneuvers, V_x^b is fairly small (within 0.2 m/s) and can be neglected. However, when the vehicle performs fast turns with side slips, the term $\dot{\psi} V_x^b$ cannot be ignored and should be taken into consideration carefully. For the time being however, the so-called pseudo pitch signal θ_{pseudo} is given by the following equation:

$$\theta_{pseudo} = \sin^{-1} \frac{f_y - b_y - a_y^b}{|g|} \qquad 3.27$$

Therefore, the misclosure of the pseudo-pitch measurements is given by

$$\delta Z_\theta = \hat{\theta} - \theta_{pseudo} \tag{3.28}$$

where $\hat{\theta}$ is the filter predicted pitch angle based on the best estimate from the last epoch. Finally the observation equation for the pseudo-pitch measurements is given by

$$\delta Z_\theta = \mathbf{H}_\theta \mathbf{dx} + v_\theta \tag{3.29}$$

where v_θ is the measurement noise of the pseudo-pitch; $\mathbf{H}_\theta$ is the corresponding design matrix that can be expressed as:

$$\mathbf{H}_{\hat{\theta}} = \begin{bmatrix} 0_{1\times5} & 1 & 0_{1\times2} & -1/|g| & 0_{1\times3} \end{bmatrix} \tag{3.30}$$

The measurement noise matrix R_θ for the pseudo-pitch is given by

$$R_\theta = \sigma_\theta^2 \tag{3.31}$$

where σ_θ^2 is the variance of v_θ for the pseudo-pitch measurements. It is noted that v_θ is related to the wheel speeds and the accelerometer sensed acceleration and thus it is implicitly correlated with the wheel speed sensor and accelerometer measurements. Thus, white noise assumption of v_θ will have a negative impact on the pitch estimates. However, this impact is expected to be minimum which is verified in the post-processing results presented below. Therefore, white noise is used here for the simplicity.

3.1.6 WSS/SAS/1A1G

When using measurements from the front wheel speed sensors, the steering angle of each of the front wheels should be compensated. The inclusion of the front wheel speed data

provides the redundant longitudinal velocity information to the system and thus improves the system reliability.

3.1.6.1 System Model

The system error states should be further augmented with four additional states in this sensor setup, namely the front left wheel scale factor error δS_{fl}, the front right wheel scale factor error δS_{fr} and the left and right steering angle error $\delta\psi_l$, $\delta\psi_r$. Therefore, the new system error states are given by

$$\mathbf{dx} = \begin{bmatrix} \delta\mathbf{r}^n & \delta V_y^b & \delta a_y^b & \delta\theta & \delta\psi & \delta\dot{\psi} & \delta\mathbf{S}_{fl} & \delta\mathbf{S}_{fr} & \delta\mathbf{S}_{rl} & \delta\mathbf{S}_{rr} & b_y & d_{YRS} & \delta\psi_l & \delta\psi_r \end{bmatrix}^T \quad 3.32$$

Similar to the rear wheel scale factor errors, the front wheel scale factors errors δS_{fl} and δS_{fr} are modeled as first order Gauss-Markov processes. The left and right steering angle error $\delta\psi_l$, $\delta\psi_r$ are also modeled as first order Gauss-Markov processes.

3.1.6.2 Measurement Model

In addition to the RWSS and YRS measurements updates, the front WSS information is also used to feed into the integration filter. The measurement misclosure for the front wheel speed sensors (FWSS) $\delta\mathbf{Z}_{FWSS}$ can be obtained by;

$$\delta\mathbf{Z}_{FWSS} = \begin{bmatrix} \hat{V}_y^b + e\hat{\dot{\psi}} \\ \hat{V}_y^b - e\hat{\dot{\psi}} \end{bmatrix} - \begin{bmatrix} V_{fl}\cos\psi_l \\ V_{fr}\cos\psi_r \end{bmatrix} \quad 3.33$$

where $\hat{V}_y^b$ and $\hat{\dot{\psi}}$ are the estimated forward speed and the yaw rate respectively; e is half of the wheel track; V_{fl} and V_{fr} are the measured front wheel speeds; ψ_l and ψ_r are the front left and right wheel angles, which can be obtained using Equation (3.5).

In order to find the relation between the measurement misclosure $\delta\mathbf{Z}_{FWSS}$ and the system error states, the steering angle-compensated front left wheel speed is differentiated as follows:

$$dV_{fl}\cos\psi_l = dV_{fl}\cos\psi_l - V_{fl}\sin\psi_l\delta\psi_l = \delta S_{fl}V_{fl}\cos\psi_l - V_{fl}\sin\psi_l\delta\psi_l \quad 3.34$$

Similarly, for the front right wheel speed

$$dV_{fr}\cos\psi_r = dV_{fr}\cos\psi_r - V_{fr}\sin\psi_r\delta\psi_r = \delta S_{fr}V_{fr}\cos\psi_r - V_{fr}\sin\psi_r\delta\psi_r \quad 3.35$$

Therefore, the measurement equation for the FWSS is expressed as:

$$\delta\mathbf{Z}_{FWSS} = \mathbf{H}_{FWSS}\mathbf{dx} + \mathbf{v}_{FWSS} \quad 3.36$$

where $\mathbf{v}_{FWSS}$ is the FWSS measurement noise vector; $\mathbf{H}_{FWSS}$ is the design matrix for the front WSS measurements, which is given by

$$\mathbf{H}_{FWSS} = \begin{bmatrix} 0_{1\times3} & 1 & 0_{1\times3} & e & -V_{fl}\cos\psi_l & 0 & 0_{1\times4} & V_{fl}\sin\psi_l & 0 \\ 0_{1\times3} & 0 & 0_{1\times3} & -e & 0 & -V_{fr}\cos\psi & 0_{1\times4} & 0 & V_{fr}\sin\psi_r \end{bmatrix} \quad 3.37$$

The measurement noise matrix $\mathbf{R}_{FWSS}$ for the FWSS is simply as follows:

$$\mathbf{R}_{FWSS} = \begin{bmatrix} \sigma_{fl}^2 & 0 \\ 0 & \sigma_{fr}^2 \end{bmatrix} \quad 3.38$$

where σ_{fl}^2 and σ_{fr}^2 are the variance of wideband noise for the front left and right wheel speeds.

3.1.7 WSS/SAS/2A1G

The last sensor setup introduced in this thesis includes all the available sensors, namely the four wheel speed sensors, one steering angle sensor, two horizontal accelerometers and one vertical gyro (yaw rate sensor). Similar as for the 1A1G case, the two accelerometers are not used for the velocity estimation with the integrated acceleration information. The lateral accelerometer is only used to provide roll estimates. The main benefit is to avoid the error accumulation during the integrating process. Furthermore, it explicitly improves the navigation performance with the roll being compensated.

The system error state in this case includes three dimensional position error $\delta\mathbf{r}^n$ in east north and up directions (δr_E ; δr_N ; δr_U), three dimensional velocity error $\delta\mathbf{V}^b$ in the body frame, two horizontal acceleration error δa_x^b, δa_y^b, three dimensional attitude error in the h- frame $\boldsymbol{\varepsilon}^h$ (refer to Appendix A for the definition of h-frame), yaw rate error $\delta\dot{\psi}$, four wheel scale factor error $\delta\mathbf{S}$ and two steering angle scale factor error $\delta\psi_l$, $\delta\psi_r$. The system states are given by

$$\mathbf{dx} = \begin{bmatrix} \delta\mathbf{r}^n & \delta\mathbf{V}^b & \delta a_x^b & \delta a_y^b & \boldsymbol{\varepsilon}^h & \delta\dot{\psi} & \delta\mathbf{S} & b_x & \delta\mathbf{S}_{rl} & \delta\mathbf{S}_{rr} & b_y & d_{YRS} & \delta\psi_l & \delta\psi_r \end{bmatrix}^T \qquad 3.39$$

3.1.7.1 System Model

The major differences between the system models used for WSS/SAS/2A1G and WSS/SAS/1A1G are the inclusion of the vertical and lateral velocity error, the lateral acceleration error, the roll error and the lateral accelerometer bias states.

The new position error states can be derived as

$$\delta\dot{\mathbf{r}}^n = R_b^n \delta\mathbf{V}^b + \delta R_b^n \mathbf{V}^b \tag{3.40}$$

Since $\boldsymbol{\varepsilon}^h$ is defined in the h-frame,

$$\delta R_b^n = R_h^n E^h R_b^h \tag{3.41}$$

Substituting Equation (3.41) into (3.40) yield::

$$\delta\dot{\mathbf{r}}^n = R_b^n \delta\mathbf{V}^b + R_h^n E^h R_b^h \mathbf{V}^b \tag{3.42}$$

Reformulating Equation (3.42), the position error equation can be obtained as

$$\delta\dot{\mathbf{r}}^n = R_b^n \delta\mathbf{V}^b - R_h^n \left(\mathbf{V}^h \times\right)\boldsymbol{\varepsilon}^h \tag{3.43}$$

The velocity error equation can be simply formed as

$$\begin{bmatrix} \delta\dot{V}_x^b \\ \delta\dot{V}_y^b \\ \delta\dot{V}_z^b \end{bmatrix} = \begin{bmatrix} 1 & 0 \\ 0 & 1 \\ 0 & 0 \end{bmatrix} \begin{bmatrix} \delta a_x^b \\ \delta a_y^b \end{bmatrix} + \begin{bmatrix} 0 \\ 0 \\ w_{vz} \end{bmatrix} \tag{3.44}$$

where w_{vz} is the driving noise of the vertical velocity random walk in unit of $m/s^s/\sqrt{Hz}$.

The attitude error states $\boldsymbol{\varepsilon}^h$ is given by

$$\boldsymbol{\varepsilon}^h = \begin{bmatrix} \delta\dot{\theta} \\ \delta\dot{\phi} \\ -\delta\dot{\psi} \end{bmatrix} = \begin{bmatrix} -\alpha_\theta & 0 \\ 0 & -\alpha_\phi \\ 0 & 0 \end{bmatrix} \begin{bmatrix} \delta\theta \\ \delta\phi \end{bmatrix} + \begin{bmatrix} 0 \\ 0 \\ -1 \end{bmatrix} \ddot{\psi} + \begin{bmatrix} w_\theta \\ w_\phi \\ 0 \end{bmatrix} \quad 3.45$$

where ϕ is the roll angle. The pitch and roll errors are modeled as first order Gauss-Markov processes. w_ϕ is the driving noise for the roll error. For details of the derivation for the attitude error equations refer to Sun (2008).

The lateral accelerometer bias is also modeled as the first order Gauss-Markov process. The other states in this sensor configuration remain the same as the in the WSS/SAS/1A1G sensor setup.

3.1.7.2 Measurement Model

Similar to the pseudo-pitch update, the pseudo-roll measurements are used to update the integration in the WSS/SAS/2A1G sensor setup. Using the kinematic relationship between the IMU outputs and the derivatives of the Euler angles, and assuming that the rotation rate of the earth is negligible, the lateral acceleration can be written as (Tseng et al 2007)

$$a_x^b = f_x - \dot{\psi} \cdot V_y^b + |g| \sin\phi \quad 3.46$$

Where

f_x is the accelerometer sensed acceleration;

V_x^b is the lateral velocity of the vehicle in the body frame;

Therefore, the so-called pseudo pitch signal ϕ_{pseudo} is given by the following equations:

$$\phi_{pseudo} = -\sin^{-1}\frac{f_x - b_x - a_y^b - \psi \dot{V}_x^b}{|g|} \tag{3.47}$$

The misclosure of the pseudo-roll measurements is given by

$$\delta Z_\phi = \hat{\phi} - \phi_{pseudo} \tag{3.48}$$

where $\hat{\phi}$ is the filter predicted roll angle based on the best estimate from the last epoch. Finally the observation equation for the pseudo-pitch measurements is given by

$$\delta Z_\phi = \mathbf{H}_\phi \mathbf{dx} + v_\phi \tag{3.49}$$

where v_ϕ is the measurement noise of the pseudo-roll $\mathbf{H}_\phi$ is the corresponding design matrix which can be expressed as:

$$\mathbf{H}_\phi = \begin{bmatrix} 0_{1\times 10} & 1 & 0_{1\times 6} & -1/|g| & 0_{1\times 4} \end{bmatrix} \tag{3.50}$$

The measurement noise matrix R_ϕ for the pseudo-roll is given by

$$R_\phi = \sigma_\phi^2 \tag{3.51}$$

where σ_ϕ^2 is the variance of v_ϕ for the pseudo-roll measurements. Similar as the pseudo-pitch measurements, the pseudo-roll measurements are correlated with WSS and accelerometer measurements. However, for simplicity, v_ϕ is considered as the white noise.

3.2 INS Mechanization Based Algorithms

For the INS mechanization based algorithms, usually two sensor setups are used namely 2A1G, and 3A1G. Since the 3A1G sensor configuration is not used for the DR based sensor

setup, and its performance is similar to that of the 2A1G setup (Sun et al 2008), only 2A1G setup is used for the development of the INS mechanization based algorithms.

Because of the removal of the two horizontal gyros and the vertical accelerometers for the 2A1G setup, the INS mechanizations and error equations should be modified to compensate the errors induced from the absent sensors. The pseudo-signal approach (Niu et al 2007b) and the local terrain predictor based approach (Sun et al 2008) are applied as compared with the DR-based algorithms.

3.2.1 Pseudo-signal Approach

Since land vehicles mainly run on relatively flat roads with pitch and roll typically less than five degrees, the output of a vertical accelerometer in a full IMU system is mainly composed of the local gravity, the road vibrations, and vehicle dynamics (Li et al 2010, Niu et al 2007b). Therefore, the z-axis accelerometer outputs of a full IMU are approximated as the sum of gravity and white noise. Similarly, the two horizontal gyro outputs of a full IMU can be regarded as zero mean white noise. Given these findings, the pseudo-signal approach proposed by Niu et al 2007b is employed for the reduced IMU/GPS integration. The main concept of the pseudo-signal approach is to replace the unavailable sensors of the reduced IMU (i.e., the vertical accelerometer and horizontal gyros) with pseudo-signals that have constant values. The pseudo-sensor noise is modeled as white noise. The horizontal gyro signals are assumed to be zero and the vertical accelerometer outputs are assumed as gravity plus white noise. These pseudo signals, together with real signals from the available sensors, are used to calculate the position, velocity, and attitude using standard INS

mechanizations. Finally, the obtained position, velocity, and attitude are fed into the standard GPS/INS integration filter to obtain the final navigation solution.

In order to limit the errors induced by the reduced IMU/GPS integrated system, the wheel speed sensor and non-holonomic constraints are applied in this work. The three-dimensional (3D) velocity updates derived from the wheel speed and non-holonomic constraints are fed into the integration filter to improve the navigation solution. The non-holonomic constraints are derived assuming the vehicle does not slip in the across track direction, which is a reasonable assumption for travel in a constant direction in the absence of ice or snow (Niu et al 2007a, Li at al 2010). Since the two assumptions are valid under most normal driving conditions, the additional description of the vehicle dynamics provided by the constraints improves navigation performance (Niu et al 2007a, Li at al 2010).

The INS mechanizations and the system model for the pseudo-signal approach is similar to that of the traditional full IMU (Niu et al 2007b, Li el al 2010). In order to apply WSS measurement updates, the scale factor $\mathbf{S}_{WSS}$ of the average rear wheel speeds is included in the system model. Therefore, the system error states in this case is

$$\mathbf{dx} = \begin{bmatrix} \delta\mathbf{r}^n & \delta\mathbf{V}^n & \delta\boldsymbol{\varepsilon}^n & \mathbf{b} & \mathbf{d} & \mathbf{S}_{WSS} \end{bmatrix}^T \tag{3.1}$$

where $\delta\boldsymbol{\varepsilon}^n$ is the attitude error in the navigation frame; $\mathbf{b}$ and $\mathbf{d}$ are the three dimensional accelerometer bias and the gyro drift in the right, forward and up directions respectively; $\mathbf{S}_{WSS}$ is the scale factor of the wheel speed sensor.

The measurement equations for the 3D velocity updates can be represented as follows:

$$\delta \mathbf{Z}_{3D} = \mathbf{V}_{3D} - \hat{\mathbf{V}}^{b}_{INS} = \begin{bmatrix} \hat{V}^{b}_{x} \\ \hat{V}^{b}_{y} \\ \hat{V}^{b}_{z} \end{bmatrix} - \begin{bmatrix} 0_{cons} \\ V^{b}_{WSS} \\ 0_{cons} \end{bmatrix} = H_{3DvsV}\delta \mathbf{V}^{n} + H_{3DvsE}\delta \boldsymbol{\varepsilon}^{n} - \delta S_{WSS} + \mathbf{n}_{3D} \qquad 3.2$$

where $\delta \mathbf{Z}_{3D}$ is the measurement misclosure of 3D velocity updates, v_{3D} is the 3D velocity constraints, 0_{cons} indicates an assumed zero velocity according to the non-holonomic constraints, $\hat{v}_{WSS}$ is the averaged velocity from the rear wheel speed sensors, $\hat{V}^{b}_{x}$, $\hat{V}^{b}_{y}$ and $\hat{V}^{b}_{z}$ are the estimated velocities in the b-frame from the INS. The 3D velocity update is related with the velocity error and the attitude error via H_{3DvsV} and H_{3DvsE} as;

$$\begin{aligned} \mathbf{H}_{3DvsV} &= R^{b}_{n} \\ \mathbf{H}_{3DvsE} &= R^{b}_{n}\left(\mathbf{V}^{n}\times\right) \end{aligned} \qquad 3.3$$

$\left(\mathbf{V}^{n}\times\right)$ is the symmetric skew matrix of $\mathbf{V}^{n}$; $\mathbf{n}_{3D}$ is the measurement noise. The measurement noise for the non-holonomic constraints is computed based on a projection of the longitudinal velocity in the lateral and up directions due to the attitude error angles (Li 2010, Godha 2006). Typically, the maximum velocity of a vehicle in the longitudinal direction is 35 m/s which is the equivalent to 126 km/h. Assuming a two degree attitude error in each direction, the projected velocity is around 1 m/s. Therefore the standard deviation of the measurement noise for the non-holonomic constraints can be set to 1 m/s. Although the noise of the two constraints is correlated, it is difficult to derive the relationship of the two noise components mathematically because the correlation is varying with vehicle dynamics. Therefore, they are assumed to be independent.

3.2.2 Local Terrain Predictor Based Approach

Sun (2008) proposed the local terrain predictor based approach for the GPS/reduced IMU integration. In his work, the pitch and roll are assumed as zeros in the INS mechanizations. Furthermore, both the pitch and roll are modeled as first order Gauss-Markov processes in the system model. Therefore, the difference between GPS and INS derived position and velocity can be used to estimate the pitch and roll.

The INS mechanization for the 2A1G configuration using the local terrain predictor approach is given by:

$$\begin{cases} \dot{\mathbf{r}}^{l} = \mathbf{D}^{-1}\mathbf{V}^{n} \\ \dot{\mathbf{V}}^{n} = R_b^n \mathbf{f}^{b} - (2\boldsymbol{\Omega}_{ie}^{n} + \boldsymbol{\Omega}_{en}^{n})\mathbf{V}^{n} + \mathbf{g}^{n} \\ \dot{\psi} = -\omega_{ibz}^{b} + \dfrac{v_e \tan\varphi}{N+h} + \omega_e \sin\varphi \\ R_b^n = R_3(\psi) \end{cases} \qquad 3.52$$

where

$$\mathbf{D}^{-1} = \begin{bmatrix} 0 & \dfrac{1}{M+h} & 0 \\ \dfrac{1}{(N+h)\cos\varphi} & 0 & 0 \\ 0 & 0 & 1 \end{bmatrix},$$

M is the meridian radius of the earth curvature;

N is the prime vertical radius of the earth curvature;

$\mathbf{r}^{l}$ is the position vector , $\mathbf{r}^{l} = [\varphi \quad \lambda \quad h]^{T}$; φ, λ and h are the latitude, longitude and height respectively;

$\mathbf{f^b}$ is the specific force vector $\mathbf{f}^b = \begin{bmatrix} f_x^b & f_y^b & f_z^b \end{bmatrix}$ from the IMU accelerometer triad. The vector represents for the specific force in the b-frame;

$\mathbf{g^l}$ is the earth's local gravity vector. $\mathbf{g}^{\mathbf{l}} = \begin{bmatrix} 0 & 0 & -g \end{bmatrix}$, where g is computed from a normal gravity model (Jekeli 2001);

$\mathbf{\Omega}_{bc}^{a}$ is a skew-symmetric matrix, which indicates the rotation rate of frame 'c', relative to frame 'b', expressed in frame 'a'. If $\boldsymbol{\omega} = \begin{bmatrix} \omega_x & \omega_y & \omega_z \end{bmatrix}$, then the corresponding skew-symmetric matrix is:

$$\mathbf{\Omega} = \begin{bmatrix} 0 & -\omega_z & \omega_y \\ \omega_z & 0 & -\omega_x \\ -\omega_y & \omega_x & 0 \end{bmatrix};$$

$\boldsymbol{\omega}_{ie}^{n}$ is the earth rotation rate projected into the l-frame, which is given by:

$\boldsymbol{\omega}_{ie}^{n} = \begin{bmatrix} 0 & \omega_e \cos\varphi & \omega_e \sin\varphi \end{bmatrix}$, ω_e is the earth rotation rate;

R_3 is the transport rate, which refers to the change of orientation of the l-frame with respect to the Earth due to motion of the object being positioned. Its expression is

$\boldsymbol{\omega}_{en}^{n} = \begin{bmatrix} -V_N/(M+h) & V_E/(N+h) & V_U \tan\varphi/(N+h) \end{bmatrix}$

R_3 is the rotation matrix about the z-axis.

It is noted that the vertical specific force f_z^b in the 2A1G sensor setup should be computed by $f_z^b = g\cos\theta\cos\phi$.

The corresponding error model for the local terrain predictor is given by

$$\begin{bmatrix} \delta\dot{\mathbf{r}}^n \\ \delta\dot{\mathbf{V}}^n \\ \dot{\boldsymbol{\varepsilon}}^h \\ \dot{d}_{YRS} \\ \dot{\mathbf{b}} \end{bmatrix} = \begin{bmatrix} 0_{3\times3} & \mathbf{I} & 0_{3\times3} & 0_{3\times1} & 0_{3\times3} \\ 0_{3\times3} & \mathbf{B} & -R_b^n(\mathbf{f}^b\times) & 0_{3\times1} & R_b^n \\ 0_{3\times3} & 0_{3\times3} & -\mathbf{A} & \mathbf{M}_d & 0_{3\times3} \\ 0_{1\times3} & 0_{1\times3} & 0_{1\times3} & -\alpha_d & 0_{1\times3} \\ 0_{3\times3} & 0_{3\times3} & 0_{3\times3} & 0_{3\times1} & -\boldsymbol{\Lambda} \end{bmatrix} \begin{bmatrix} \delta\mathbf{r}^n \\ \delta\mathbf{V}^n \\ \boldsymbol{\varepsilon}^h \\ d_{YRS} \\ \mathbf{b} \end{bmatrix} + \begin{bmatrix} 0_{3\times1} \\ R_b^n\mathbf{W}_f \\ \mathbf{W}_\varepsilon \\ w_{YRS} \\ \mathbf{W}_b \end{bmatrix} \quad 3.53$$

where $(\mathbf{f}^b\times)$ is the skew-symmetric matrix of $\mathbf{f}^b$; $\mathbf{A}$ is the $diag(\alpha_\phi \quad \alpha_\theta \quad 0)$; $\mathbf{M}_d$ is $[0 \quad 0 \quad -1]^T$; $\mathbf{W}_\varepsilon = [w_\phi \quad w_\theta \quad w_\psi]^T$; $\boldsymbol{\Lambda} = diag(\alpha_{bx} \quad \alpha_{by} \quad \alpha_{bz})$, α_{bx}, α_{by} and α_{bz} are the reciprocal correlation time of the accelerometer biases; $\mathbf{W}_b$ is the driving noise vector of the accelerometer biases. It is noted that the vertical accelerometer bias reflects the vertical variation of the local terrain rather than the actual accelerometer bias because of the unavailability of a vertical accelerometer. For further details of the model refer to Sun et al (2008).

The 3D velocity updates can be also applied in the local terrain predictor approach to improve the navigation performance using the WSS and the non-holonomic constraints information. Similar measurement equation as presented in Section 3.2.1 can be used in this case except for H_{3DvsE} being replaced by

$$\mathbf{H}_{3DvsE} = R_h^b(\mathbf{V}^h\times) \quad 3.4$$

where $\mathbf{V}^h = R_n^h\mathbf{V}^n$.

3.3 GPS and Vehicle Sensor Integration

The GPS and vehicle sensor integrated system provides improved long-term and short-term accuracy compared with the standalone GPS or vehicle sensor based system. Typically,

there are three integration strategies, which are classified into the loosely coupled, tightly coupled and ultra-tightly coupled integration. The ultra-tightly coupled integration has been introduced in Chapter 5. Therefore, it is not included in this section. Furthermore, the loose and tight integration introduced in this section is based on the DR approach. Please refer to Farrell (2008) or Jekeli (2001) for the traditional INS mechanization based GPS/INS integration.

3.3.1 Loosely Coupled Integration

In the loosely coupled integration, the GPS measurements are processed independently in a GPS-only navigation filter. Then the outputs of this filter are used to periodically update the integration filter. The integration filter uses the difference between the GPS-derived position and velocity estimates and the DR system derived position and velocities as the measurement misclosures to update the integrated navigation solution.

The benefits of the loose integration are the relative ease of implementation and robustness (Petovello 2003, Godha 2006). Robustness occurs because the GPS and INS operate independently. However, the use of a GPS filter used to compensate for the user's dynamics would have negative effect on the state estimation. Furthermore, the estimated position and velocity in east, north and up directions are not completely uncorrelated, which makes the Kalman filter suboptimal.

In order to form the GPS measurement misclosure, the longitudinal velocity V_y^b should be transformed into the navigation frame (n-frame), which is given by

$$\delta \mathbf{Z}_{GPS} = \left(\begin{bmatrix} \hat{\lambda} \\ \hat{\varphi} \\ \hat{h} \\ \hat{\mathbf{V}}^n \end{bmatrix}_{Filter} - \begin{bmatrix} \lambda \\ \varphi \\ h \\ \mathbf{V}^n \end{bmatrix}_{GPS} \right) \begin{bmatrix} (N+h)\cos\varphi \\ M+h \\ 1 \\ 1 \end{bmatrix}^T \quad 3.54$$

where $\hat{\lambda}$, $\hat{\varphi}$, $\hat{h}$ is the filter predicted latitude, longitude and altitude; M is the meridian radius of the earth curvature; N is the prime vertical radius of the earth curvature; $\hat{V}^n$ is filter predicted velocity in the navigation frame, which can be obtained by

$$\hat{\mathbf{V}}^n = R_b^n \begin{bmatrix} 0 & \hat{V}_y^b & 0 \end{bmatrix}^T \quad 3.55$$

3.3.2 Tightly Coupled Integration

For the tightly coupled integration strategy, the raw GPS measurements are directly used to update the integration filter. The integration filter uses the differences between the GPS generated pseudorange and range rate measurements and the DR predicted pseudorange and range rate measurements to obtain the error estimates. These error estimates are then used to correct the system states.

The primary advantage of tight integration is the GPS measurements used to update the filter are more statistically independent compared with the position and velocity, which improves the reliability of the blunder detection. The major drawback of the tight integration compared with the loosely integration is the increased size of the state vector, which leads to an increased computational burden (Petovello 2003).

When tight integration is applied, the system models as presented in previous sections should be augmented with receiver clock bias $c\delta t$ and drift $cd\delta t$ states. The measurement equation of the pseudorange updates is written as

$$\delta \mathbf{Z}_{\rho}^{i} = \hat{\rho}^{i} - \rho_{GPS}^{i} = H_{\rho,1\times 3}^{i} \begin{bmatrix} \delta r_E \\ \delta r_N \\ \delta r_U \end{bmatrix}^{T} + c\delta t + v_{\rho}^{i} \qquad 3.56$$

where $\delta \mathbf{Z}_{\rho}^{i}$ is the misclosure of the pseudorange measurements, $\hat{\rho}^{i}$ is the estimated pseudorange for the *i-th* statellite; ρ_{GPS}^{i} is the raw pseudorange measurement for the *i-th* satellite; $H_{\rho,1\times 3}^{i} = \begin{bmatrix} -\cos(E)\sin(A) & -\cos(E)\cos(A) & -\sin(E) \end{bmatrix}$, A and E are the *i-th* satellite elevation angle and azimuth respectively. v_{ρ}^{i} is the pseudorange measurement noise.

For the sensor setups except for the WSS/SAS/2A1G, the measurement equation for the pseudorange rate (i.e., Doppler) updates from GPS can be expressed as

$$\delta \mathbf{Z}_{\dot{\rho}}^{i} = \hat{\dot{\rho}}^{i} - \dot{\rho}_{GPS}^{i} = H_{\dot{\rho},1\times 3}^{i} H_{v} \delta V_{y}^{b} + H_{\dot{\rho},1\times 3}^{i} H_{\theta} \delta\theta + H_{\dot{\rho},1\times 3}^{i} H_{\psi} \delta\psi + c\delta dt + v_{\dot{\rho}}^{i} \qquad 3.57$$

where $\delta \mathbf{Z}_{\dot{\rho}}^{i}$ is the misclosure of the pseudorange range rate, $\hat{\dot{\rho}}^{i}$ is the estimated range rate for the *i-th* satellite, $\dot{\rho}_{GPS}^{i}$ is the raw GPS range rate measurements for the *i-th* satellitete and $v_{\dot{\rho}}^{i}$ is the measurement noise of the pseudorange rate; and

$$\begin{aligned} H_{\dot{\rho},1\times 3}^{i} &= \begin{bmatrix} -\cos(E)\sin(A) & -\cos(E)\cos(A) & -\sin(E) \end{bmatrix} \\ H_{v} &= \begin{bmatrix} \sin\psi\cos\theta & \cos\psi\sin\theta & \sin\theta \end{bmatrix}^{T} \\ H_{\theta} &= \begin{bmatrix} -V_{y}^{b}\sin\psi\sin\theta & -V_{y}^{b}\cos\psi\sin\theta & V_{y}^{b}\cos\theta \end{bmatrix}^{T} \\ H_{\psi} &= \begin{bmatrix} V_{y}^{b}\cos\psi\cos\theta & -V_{y}^{b}\sin\psi\cos\theta & 0 \end{bmatrix}^{T} \end{aligned}$$

For WSS/SAS/2A1G sensor setup, the measurement equation for the pseudorange rate (i.e., Doppler) updates from GPS can be expressed as

$$\delta \mathbf{Z}_{\dot{\rho}}^{i} = \hat{\dot{\rho}}^{i} - \dot{\rho}_{GPS}^{i} = H_{\dot{\rho},1\times 3}^{i} R_{n}^{b} \delta \mathbf{V}^{b} + H_{\dot{\rho},1\times 3}^{i} H_{\theta} \boldsymbol{\varepsilon}^{h} + c\delta dt + v_{\dot{\rho}}^{i} \qquad 3.58$$

where

$$H_{\dot{\rho},1\times 3}^{i} = \begin{bmatrix} -\cos(E)\sin(A) & -\cos(E)\cos(A) & -\sin(E) \end{bmatrix}$$
$$H_{\boldsymbol{\varepsilon}^{h}} = R_{h}^{n}\left(\mathbf{V}^{h}\times\right)$$

3.4 Field Test Results and Performance Analysis

Having explained the GPS/vehicle sensor integration using DR based algorithms, field test were used to evaluate the performance of the proposed algorithms. The field tests were conducted under two scenarios: a suburban and foliage scenario and an urban canyon scenario. The equipment setup and the test environments are the same as those presented in Section 2.4. Both the loose and tight GPS/vehicle sensor integration results are analyzed in this section. The standard GPS receiver GSNRx^{TM}, the high sensitivity block processing GPS receiver GSNRx-hs^{TM} and the automotive grade GPS receiver were used for the performance analysis.

3.4.1 Foliage Scenario

In this section, the results from the foliage test are summarized and analyzed. The test setup is the same as that presented in Section 2.4.1. Both loose and tight integration of GPS and various vehicle sensors are presented and discussed.

3.4.1.1 Loose Integration Results

To begin with the analysis, the results from the loose integration of GPS and vehicle sensors are presented. The position, velocity and attitude accuracy are used as metrics for performance evaluation with different sensor configurations.

RWSS Setup

The results from the RWSS setup are presented first for the performance analysis. The position, velocity and attitude errors are shown in Figure 3.2, Figure 3.3 and Figure 3.4 respectively. The GPS/RWSS solutions using the automotive grade GPS receiver and GSNRx-hs™ demonstrate similar positioning and attitude accuracies. It is expected since the standalone GSNRx-hs™ and automotive grade GPS receiver have similar performance in the suburban and foliage test. The RMS position, velocity and attitude errors are summarized in Table 3.1 and Table 3.2.

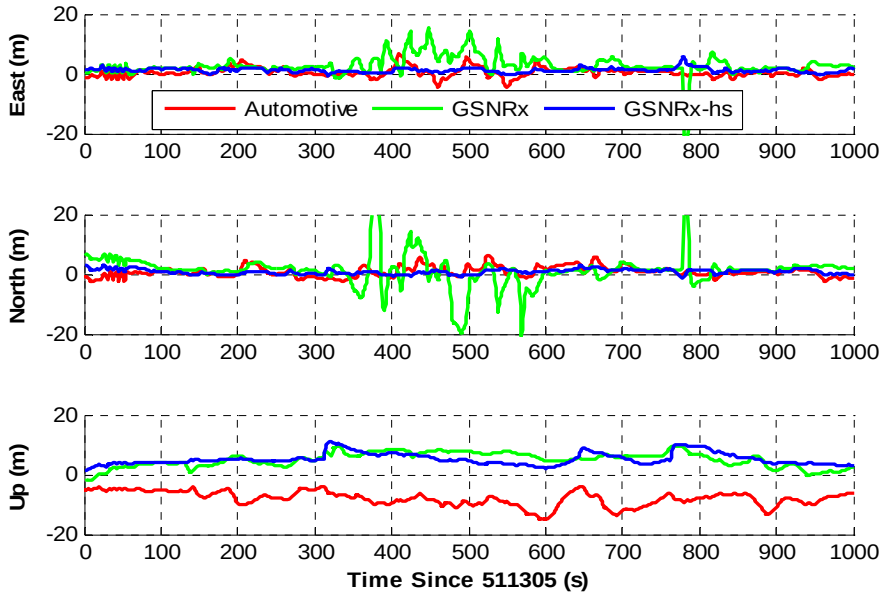

Figure 3.2: Position error plots for the GPS/RWSS in suburban and foliage test

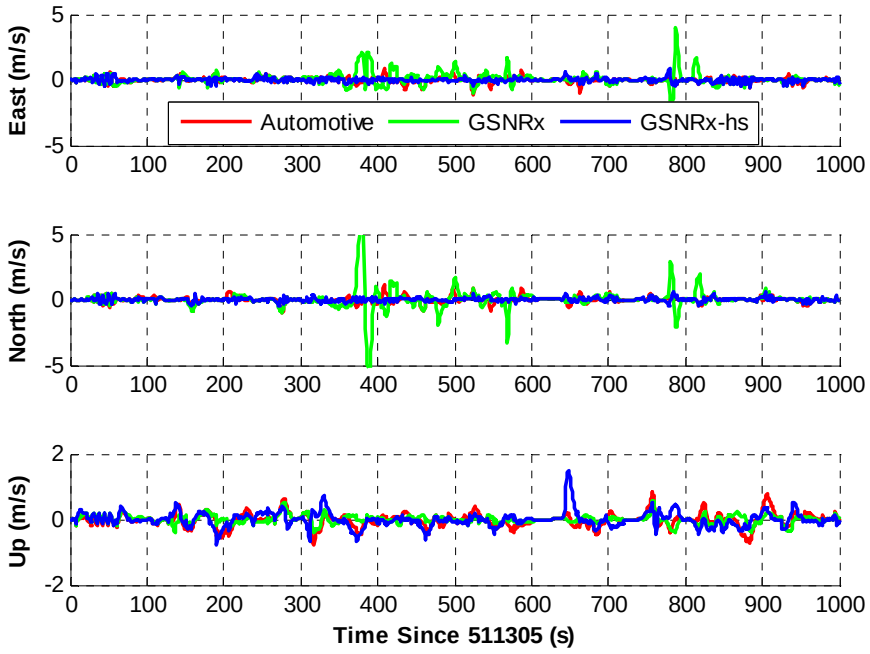

Figure 3.3: Velocity error plots for the GPS/RWSS in suburban and foliage test

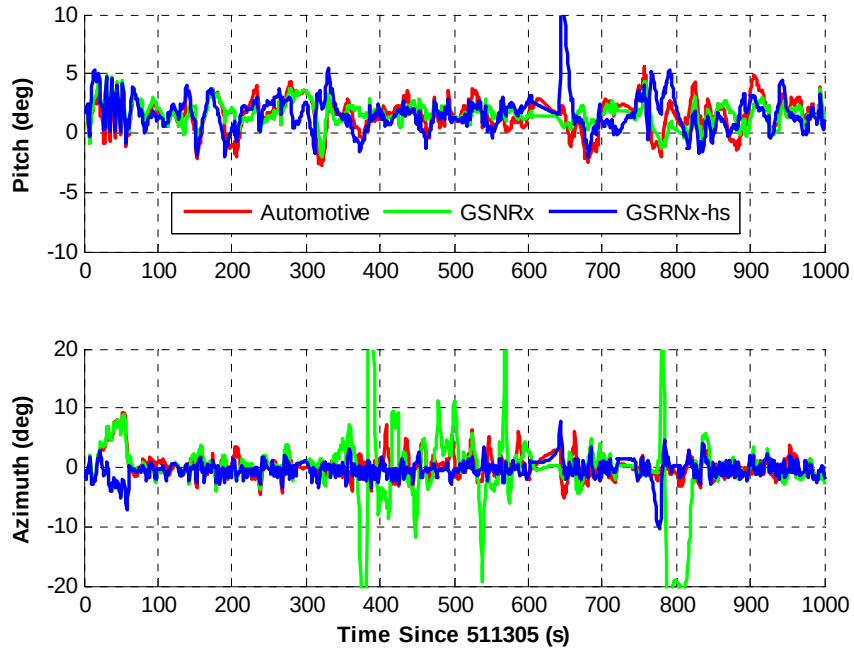

Figure 3.4: Attitude error plots for the GPS/RWSS in suburban and foliage test

Table 3.1: Summarized RMS position and velocity errors with loose integration of GPS/RWSS in the suburban and foliage test

	Position (m)			Velocity (m/s)		
	East	North	Up	East	North	Up
Automotive	1.7	1.9	8.4	0.21	0.24	0.21
GSNRx™	6.1	6.2	5.6	0.37	0.65	0.10
GSNRx-hs™	1.4	1.1	5.5	0.17	0.16	0.13

Table 3.2: Summarized RMS attitude errors with loose integration of GPS/RWSS in the suburban and foliage test

	Pitch (deg)	Azimuth (deg)
Automotive	2.27	2.38
GSNRx™	1.90	4.68
GSNRx-hs™	1.94	2.16

Compared with the GPS only solutions, the loosely coupled GPS/RWSS solutions provide minimal improvement in terms of position accuracy. However, for the automotive grade GPS receiver and standard GSNRx™ cases, improved velocity estimates were obtained when integrated with RWSS. The accuracy of the horizontal velocity improves by 23% to 73% for the two receivers. For the GSNRx-hs™ receiver, the velocity improvement is minimal since standalone GSNRx-hs™ already provides decent velocity estimates in this test environment.

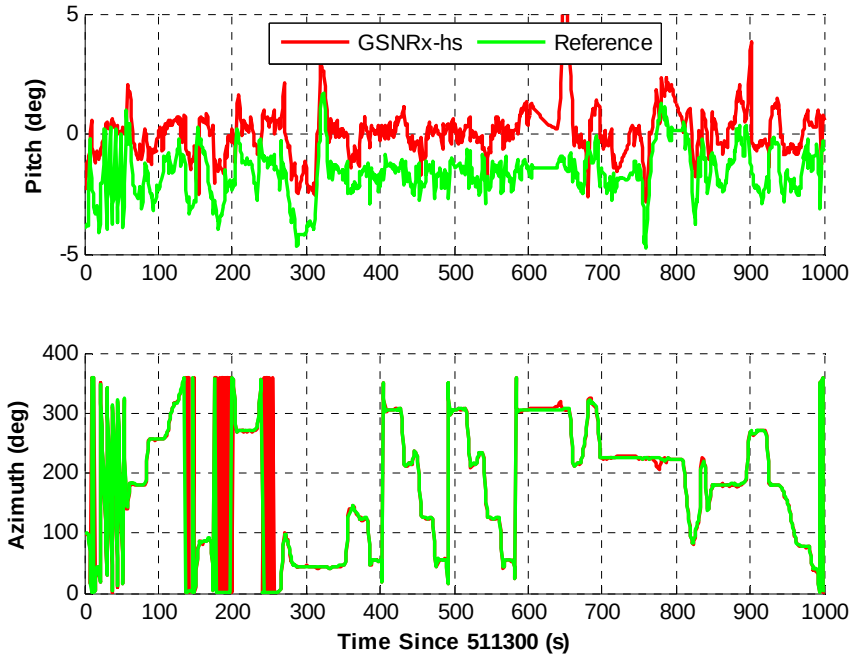

Figure 3.5: Attitude plots for the GSNRx-hs™/RWSS in suburban and foliage test

As shown in Figure 3.5, both the pitch and azimuth can be estimated with the RWSS sensor setup. However the azimuth estimates can be obtained without GPS updates. The accuracy of the azimuth estimates usually degrades with unidentified wheel slips and biased GPS velocity under dense foliage areas. Thus, due to the degraded velocity accuracy from the standard GSNRx™, the azimuth obtained from the automotive grade GPS receiver and GSNRx-hs™ outperforms that of the GSNRx™ receiver. Unlike the azimuth, the pitch estimates can be estimated only when GPS measurements are available. Compared with the results from the automotive grade GPS receiver, GSNRx™ and GSNRx-hs™ provide slightly better pitch estimates. The reason is that the pitch estimates are related to the accuracy of the vertical position and velocity from the GPS receiver. And the GPS only

solutions from GSNRx^{TM} and GSNRx-hs^{TM} receivers offer better vertical position and velocity accuracy compared to that of the automotive grade GPS receiver.

RWSS/YRS Setup

As discussed in the previous section, the differential wheel speed derived yaw rate is vulnerable to the wheel slips, thus resulting in the degraded azimuth estimates. The YRS can be applied to overcome the limitations of the RWSS setup as shown below.

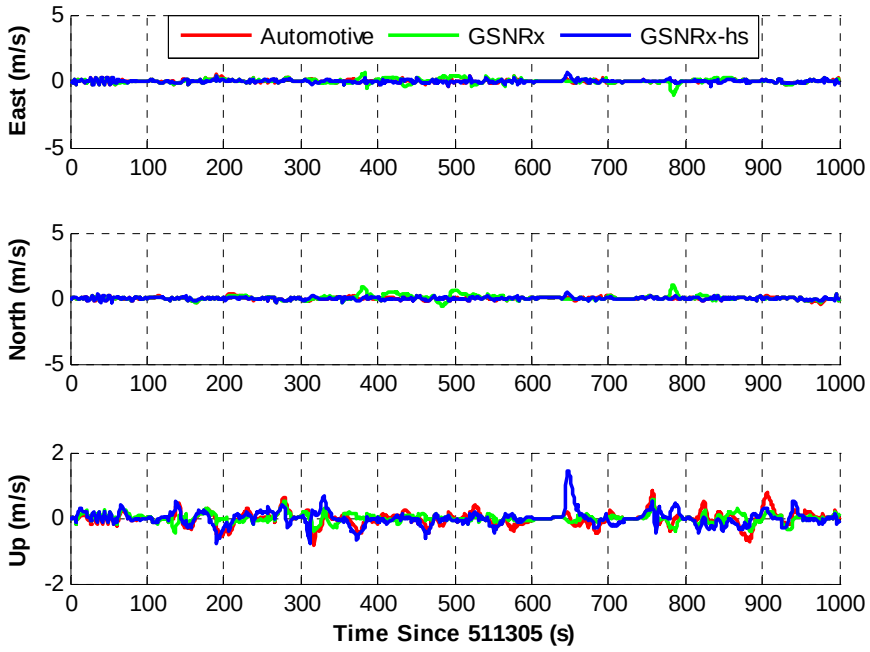

Figure 3.6: Velocity error plots for the GPS/RWSS/YRS in suburban and foliage test

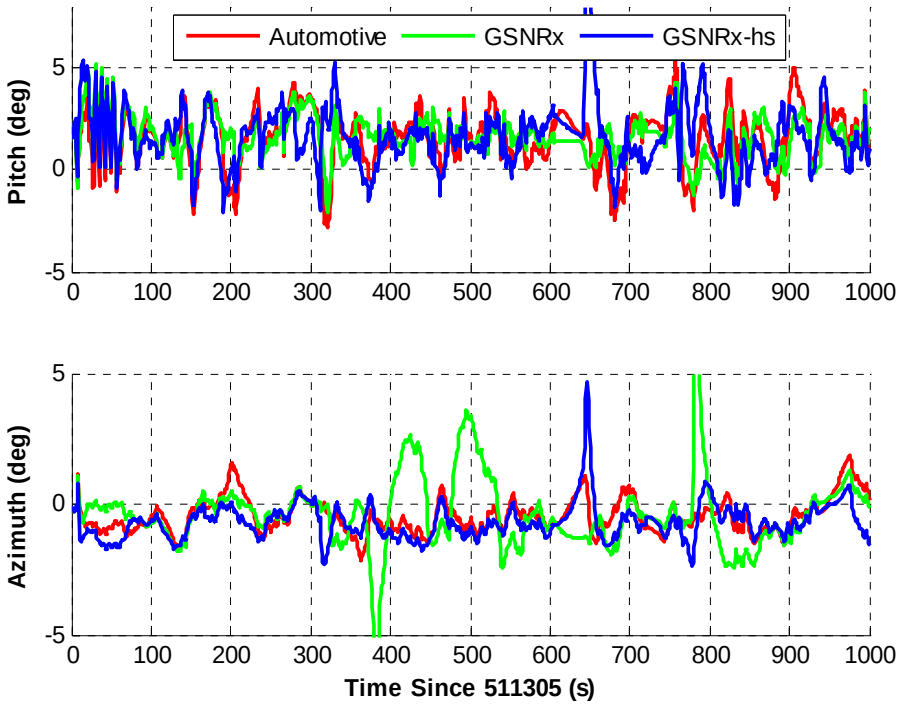

Figure 3.7: Attitude error for the GPS/RWSS/YRS in suburban and foliage test

Compared with the results from the RWSS setup, the GPS/RWSS/YRS solutions provide improved velocity and azimuth estimates as shown in Figure 3.6 and Figure 3.7. It is mainly due to the improved azimuth estimates benefitting from the YRS measurements. However, the position accuracy remains the same as that from the RWSS setup for the automotive grade GPS receiver and GSNRx-hs^{TM}. When using the standard GSNRx^{TM}, the inclusion of YRS does slightly improve the position accuracy, which is due to the noticeably improved velocity estimates. Table 3.3 and Table 3.4 give the position, velocity and attitude errors obtained from the GPS/RWSS/YRS system.

Table 3.3: Summarized RMS position and velocity errors with loose integration of GPS/RWSS/YRS in the suburban and foliage test

	Position (m)			Velocity (m/s)		
	East	North	Up	East	North	Up
Automotive	1.4	1.8	8.4	0.10	0.10	0.21
GSNRx™	2.6	3.7	5.6	0.11	0.12	0.10
GSNRx-hs™	1.4	1.1	5.4	0.10	0.09	0.09

Table 3.4: Summarized RMS attitude errors with loose integration of GPS/RWSS/YRS in the suburban and foliage test

	Pitch (deg)	Azimuth (deg)
Automotive	2.40	0.96
GSNRx™	1.86	1.03
GSNRx-hs™	1.80	0.97

RWSS/1A1G

When the longitudinal accelerometer is applied in the navigation solution, the pitch can be estimated without GPS updates. The improvement in the pitch estimates implicitly provides better navigation performance, especially during GPS outages.

Figure 3.8 illustrates the pitch and azimuth estimates from the RWSS/YRS sensor setup. Compared to pitch estimates in Figure 3.5 from the RWSS setup, RWSS/1A1G offers improved pitch accuracy as shown in Figure 3.8. Table 3.6 and Table 3.6 provide the summarized positioning and attitude results. The RWSS/1A1G sensor setup has unnoticeable position, velocity and azimuth improvements over the RWSS/YRS setup. It

may result from the limited pitch dynamics (within 5 deg) as shown in Figure 3.8. Since the estimated pitch is used to transform the wheel speeds and yaw rate from the body frame to the local level frame, the small pitch angle (e.g. within 5 deg) would contribute little to the transformation matrix, and thus does not impact the solution significantly. However, the pitch accuracy is improved by over 24% for all GPS receivers.

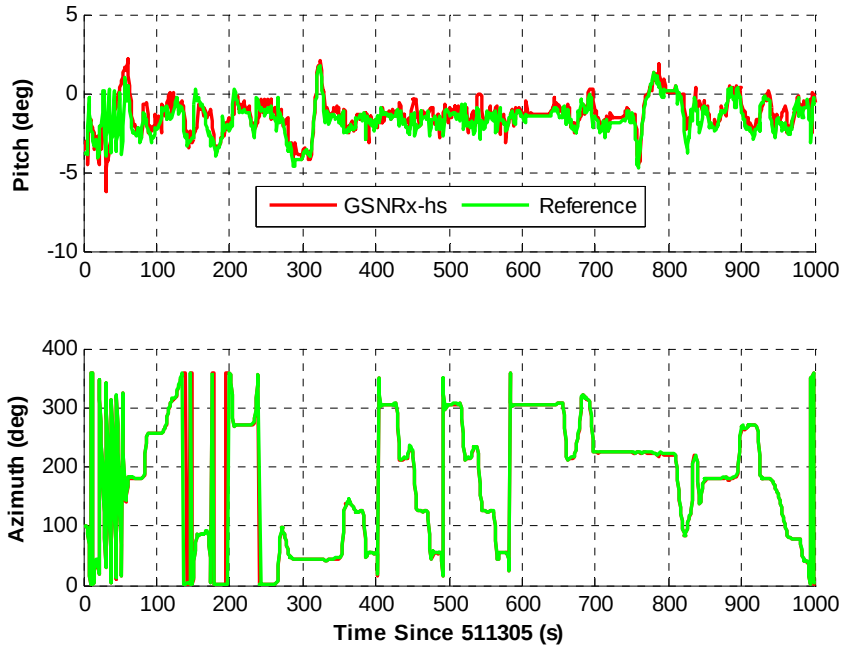

Figure 3.8: Attitude plots for the GSNRx-hs™/RWSS/1A1G in suburban and foliage test

Table 3.5: Summarized RMS position and velocity errors with loose integration of GPS/RWSS/1A1G in the suburban and foliage test

	Position (m)			Velocity (m/s)		
	East	North	Up	East	North	Up
Automotive	1.4	1.8	8.6	0.10	0.10	0.19
GSNRx™	2.6	3.7	5.2	0.11	0.12	0.11
GSNRx-hs™	1.4	1.1	5.4	0.09	0.09	0.09

Table 3.6: Summarized RMS attitude errors with loose integration of GPS/RWSS/1A1G in the suburban and foliage test

	Pitch (deg)	Azimuth (deg)
Automotive	1.15	0.92
GSNRx™	1.37	1.02
GSNRx-hs™	1.48	0.96

WSS/SAS/1A1G

When the front wheel speed sensors are used in the navigation system, the redundant sensor setup improves robustness of the system. Table 3.7 and Table 3.8 give the positioning and attitude errors for the GPS/WSS/SAS/1A1G sensor setup. As summarized in the two tables, there is no noticeable performance improvement when the front wheel speeds are used for the navigation updates. This is because the front wheel speeds obtained from the front wheel speed sensors have a similar accuracy to that of the rear wheel speeds. The contribution of the front wheel speed sensors is thus less influential to the navigation performance. However, the inclusion of the front wheel speed sensors still has a positive impact on the likelihood of sensor failure identification.

Table 3.7: Summarized RMS position and velocity errors with loose integration of GPS/WSS/SAS/1A1G in the suburban and foliage test

	Position (m)			Velocity (m/s)		
	East	North	Up	East	North	Up
Automotive	1.4	1.7	8.6	0.10	0.10	0.19
GSNRx™	2.5	3.7	5.1	0.11	0.12	0.11
GSNRx-hs™	1.4	1.1	5.4	0.09	0.09	0.09

Table 3.8: Summarized RMS attitude errors with loose integration of GPS/WSS/SAS/1A1G in the suburban and foliage test

	Pitch (deg)	Azimuth (deg)
Automotive	1.09	0.89
GSNRx™	1.37	1.02
GSNRx-hs™	1.48	0.96

WSS/SAS/2A1G

Previous sensor setups ignore the roll dynamics of the vehicle during the navigation processing. When a lateral accelerometer is used in the system, the roll can be estimated in this case. The consideration of roll dynamics may implicitly improve navigation performance, especially when vehicles are operating on unlevelled roads.

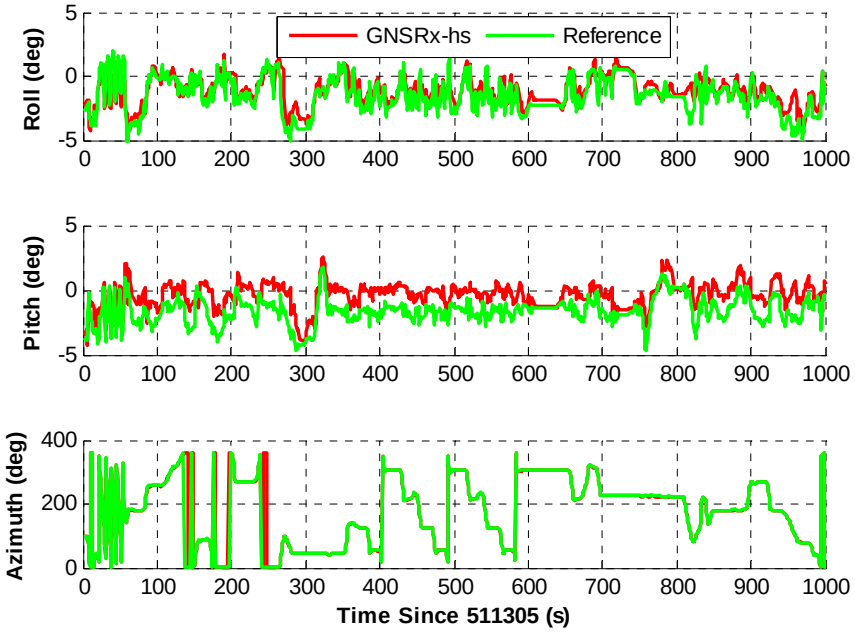

Figure 3.9: Attitude plots for the GSNRx-hs™/WSS/2A1G in suburban and foliage test

Figure 3.9 shows the attitude plots from the GSNRx-hs™/WSS/2A1G setup. As illustrated in Table 3.9 and Table 3.10, the inclusion of the roll angle does not improve the navigation performance compared to the case without pseudo-roll updates. It may result from the limited roll dynamics (within 5 deg) as shown in the reference solution. Similarly to the analysis for the pitch, a small roll angle has minimal impact on the rotation matrix from the body frame to the local level frame. Thus it has limited contribution to the navigation solution.

Table 3.9: Summarized RMS position and velocity errors with loose integration of GPS/WSS/SAS/2A1G in the suburban and foliage test

	Position (m)			Velocity (m/s)		
	East	North	Up	East	North	Up
Automotive	1.4	1.8	8.5	0.10	0.10	0.19
GSNRx™	2.4	3.7	5.1	0.11	0.12	0.11
GSNRx-hs™	1.4	1.0	5.4	0.09	0.09	0.09

Table 3.10: Summarized RMS attitude errors with loose integration of GPS/WSS/SAS/2A1G in the suburban and foliage test

	Pitch (deg)	Roll (deg)	Azimuth (deg)
Automotive	0.89	0.87	0.88
GSNRx™	1.31	0.87	1.02
GSNRx-hs™	1.44	0.87	0.89

Since the performance of GSNRx-hs™ and vehicle sensor integrated solution is the focus of the research, Table 3.11 and Table 3.12 summarize the positioning and attitude accuracies using different sensor setups with the GSNRx-hs™ receiver. Compared with the

GPS only solution, the GSNRx-hs^{TM}/DR system provides minimal improvement for the position accuracy but 47% improvement for the horizontal velocity.

Table 3.11: Summarized RMS position and velocity errors with loose integration of GSNRx-hs^{TM}/WSS/SAS/2A1G in the suburban and foliage test

	Position (m)			Velocity (m/s)		
	East	North	Up	East	North	Up
RWSS	1.4	1.1	5.4	0.17	0.16	0.13
RWSS/YRS	1.4	1.1	5.4	0.10	0.09	0.09
RWSS/1A1G	1.4	1.1	5.4	0.09	0.09	0.09
WSS/SAS/1A1G	1.4	1.1	5.4	0.09	0.09	0.09
WSS/SAS/2A1G	1.4	1.0	5.4	0.09	0.09	0.09

Table 3.12: Summarized RMS attitude errors with loose integration of GSNRx-hs^{TM} /WSS/SAS/2A1G in the suburban and foliage test

	Pitch (deg)	Roll (deg)	Azimuth (deg)
RWSS	1.94	N/A	2.16
RWSS/YRS	1.80	N/A	0.97
RWSS/1A1G	1.48	N/A	0.96
WSS/SAS/1A1G	1.48	N/A	0.96
WSS/SAS/2A1G	1.44	0.87	0.89

In summary, using the loose integration of GPS and vehicle sensors, the horizontal velocity accuracy can be improved by 35% to 91% compared to that of GPS only solutions. When GPS derived positions and velocities are of a relatively high quality, using vehicle sensors cannot improve the position accuracy significantly. However, when the position and velocity accuracy from the GPS receiver is relatively poor (e.g., when using GSNRx^{TM} for

the data analyzed here) under dense foliage areas, up to 65% position accuracy improvement can be obtained when using vehicle sensors. Furthermore, the RWSS/YRS sensor setup is sufficient to provide high accuracy positioning solutions in the suburban and foliage scenario. The inclusion of additional sensors to the RWSS/YRS does not improve the navigation solution noticeably.

Pseudo-signal Approach

For comparison purposes, the traditional INS mechanization based approach with 3D velocity updates is used for the performance analysis. The vehicle sensors used in this case include RWSS and 2A1G.

Table 3.13 and Table 3.14 summarize the position, velocity and attitude errors using the pseudo-signal approach for the GPS and vehicle sensor integration. Compared with GPS only solutions, the pseudo-signal approach provides a similar position accuracy and slightly improved velocity accuracy. However, compared with the DR based solutions (except for the RWSS setup), both the position and velocity accuracies from the pseudo-signal approach are slightly degraded. The reason is that the velocity estimates derived from the INS mechanization are vulnerable to the erroneous accelerometer bias induced by the biased GPS velocity updates in degraded signal environments. The velocity error accumulates quickly during the acceleration integration process for the pseudo-signal approach. However, the velocity derived from wheel speeds for the DR algorithms is less sensitive to the GPS velocity errors. Thus the DR based algorithms are more reliable than

the pseudo-signal based INS mechanizations, especially under degraded signal environments.

It is also noted that the pitch and roll estimates for the pseudo-signal approach rely heavily on the quality of the GPS solution. Thus, the pitch and roll estimates degrade quickly under dense foliage environments due to the degraded GPS solution. Therefore, the pitch and roll estimates from the pseudo-signal approach are slight worse than those from the DR based solutions.

Table 3.13: Summarized RMS position and velocity errors with loose integration using psedo-signal approach in the suburban and foliage test

	Position (m)			Velocity (m/s)		
	East	North	Up	East	North	Up
Automotive	1.4	1.8	6.1	0.20	0.20	0.16
GSNRx™	4.9	5.7	5.7	0.23	0.29	0.10
GSNRx-hs™	1.5	1.1	5.8	0.15	0.17	0.10

Table 3.14: Summarized RMS attitude errors with loose integration using pseudo-signal approach in the suburban and foliage test

	Pitch (deg)	Roll (deg)	Azimuth (deg)
Automotive	2.42	1.72	1.35
GSNRx™	2.09	1.90	1.94
GSNRx-hs™	2.02	1.89	1.10

Local Terrain Predictor Approach

Table 3.15 and Table 3.16 summarize the navigation accuracy of the LTP approach. The performance of the LTP is similar to that of pseudo-signal approach. However, improved pitch and roll estimates are obtained with LTP. This is due to the constrained pitch and roll dynamics used in the LTP algorithm (Sun et al 2008). The velocity accuracy of LTP is also inferior to the DR-based solutions. The main reason, which is similar to the pseudo-signal approach, is the use of accelerometers to generate velocity estimates rather than directly using wheel speeds.

Table 3.15: Summarized RMS position and velocity errors with loose integration using LTP approach in the suburban and foliage test

	Position (m)			Velocity (m/s)		
	East	North	Up	East	North	Up
Automotive	1.5	1.9	8.8	0.26	0.27	0.26
GSNRx^{TM}	3.5	4.8	4.5	0.22	0.28	0.20
GSNRx-hs^{TM}	1.5	1.1	4.6	0.22	0.20	0.20

Table 3.16: Summarized RMS attitude errors with loose integration using LTP approach in the suburban and foliage test

	Pitch (deg)	Roll (deg)	Azimuth (deg)
Automotive	0.80	0.91	1.78
GSNRx^{TM}	0.96	0.79	1.57
GSNRx-hs^{TM}	0.79	0.83	1.04

In summary, the DR-based algorithms outperform the INS mechanization based algorithms, especially when the quality of GPS signals is degraded under dense foliage. The INS

mechanization based algorithms rely on the GPS measurements to frequently correct the accelerometer bias for the system velocity estimates. However, the WSS derived velocity requires less frequent updates from GPS to maintain certain accuracy. Therefore the proposed DR-based algorithms provide higher reliability and improved navigation performance, and are used in the navigation system for land vehicle testing in the thesis.

3.4.1.2 Tight Integration Results

Having discussed the results from the loose integration of GPS and vehicle sensors, the performance evaluation of the tight integration results is conducted in this section. Similar to the data analysis strategy in the loose integration, the automotive grade GPS receiver, standard GSNRx™ and GSNRx-hs™ are used for the tight integration.

Table 3.17: Summarized RMS positioning error with tight integration using the automotive GPS receiver in the suburban and foliage test

	Position (m)			Velocity (m/s)		
	East	North	Up	East	North	Up
RWSS	1.7	1.2	5.1	0.20	0.22	0.19
RWSS/YRS	1.5	1.2	4.2	0.10	0.09	0.14
RWSS/1A1G	1.5	1.2	2.2	0.10	0.09	0.14
WSS/1A1G	1.5	1.2	2.2	0.09	0.08	0.14
WSS/2A1G	1.3	1.2	2.2	0.10	0.09	0.16

Table 3.18: Summarized RMS attitude errors with tight integration using the automotive grade GPS receiver in the suburban and foliage test

	Pitch (deg)	Roll (deg)	Azimuth (deg)
RWSS	2.23	N/A	2.51
RWSS/YRS	2.01	N/A	0.89
RWSS/1A1G	1.04	N/A	0.87
WSS/1A1G	1.03	N/A	0.87
WSS/2A1G	0.85	0.87	0.88

Table 3.19 and Table 3.20 list the results from the tight integration of the standard GSNRx^{TM} receiver and vehicle sensors. Unlike the tight integration with the automotive grade GPS receiver, the tight integration solution with GSNRx^{TM} provides improved position and velocity accuracy compared with the corresponding loose integration results. This is mainly due to the improved blunder detection reliability using tight integration.

Table 3.19: Summarized RMS position and velocity errors with tight integration using GSNRx^{TM} receiver in the suburban and foliage test

	Position (m)			Velocity (m/s)		
	East	North	Up	East	North	Up
RWSS	2.5	2.8	4.3	0.28	0.29	0.14
RWSS/YRS	1.8	2.2	4.4	0.09	0.10	0.14
RWSS/1A1G	1.8	2.2	3.4	0.09	0.08	0.14
WSS/1A1G	1.8	2.2	3.4	0.08	0.08	0.14
WSS/2A1G	1.7	2.1	3.6	0.07	0.07	0.16

Table 3.20: Summarized RMS attitude errors with tight integration using GSNRx™ in the suburban and foliage test

	Pitch (deg)	Roll (deg)	Azimuth (deg)
RWSS	1.75	N/A	3.11
RWSS/YRS	1.73	N/A	0.97
RWSS/1A1G	1.03	N/A	1.02
WSS/1A1G	1.03	N/A	1.02
WSS/2A1G	0.89	0.88	0.94

Table 3.21 and Table 3.22 summarize the results from the tight integration with GSNRx-hs™. Similar performance is obtained as that of the loose integration with GSNRx-hs™ when using tight integration. Compared with the tight integration solutions using the automotive grade GPS receiver and GSNRx™, the tight integration of GSNRx-hs™ and vehicle sensors provides the best performance. And it is also noted that the WSS/2A1G setup offers the best performance over the other sensor setup although its improvement is quite minimal.

Table 3.21: Summarized RMS position and velocity errors with tight integration using GSNRx-hs™ receiver in the suburban and foliage test

	Position (m)			Velocity (m/s)		
	East	North	Up	East	North	Up
RWSS	1.2	0.9	4.5	0.17	0.19	0.10
RWSS/YRS	1.2	0.8	4.5	0.10	0.09	0.09
RWSS/1A1G	1.2	0.8	3.8	0.10	0.08	0.09
WSS/1A1G	1.2	0.8	3.7	0.10	0.08	0.09
WSS/2A1G	1.0	0.6	3.8	0.08	0.08	0.10

Table 3.22: Summarized RMS attitude errors with tight integration using GSNRx-hs™ in the suburban and foliage test

	Pitch (deg)	Roll (deg)	Azimuth (deg)
RWSS	1.80	N/A	2.04
RWSS/YRS	1.76	N/A	1.21
RWSS/1A1G	1.33	N/A	1.02
WSS/1A1G	1.33	N/A	1.02
WSS/2A1G	1.22	0.89	1.02

In summary, the tight integration of standard GSNRx™ and vehicle sensor outperforms its corresponding loose integration solution. However, for the automotive grade GPS receiver and GSNRx-hs™, tight integrations yield minimum improvement over the loose integration solutions. Among the three receivers, the tight solution with the GSNRx-hs™ receiver provides the best performance in terms of positioning accuracy.

3.4.2 Urban Canyon Scenario

Having discussed the results from the suburban and foliage test, the performance analysis is conducted for the urban canyon test in this section. Similar to the suburban and foliage test, the results are analyzed for both the loose and tight integration.

3.4.2.1 Loose Integration Results

Similar to the foliage test analysis, the loose integration results presented are from the automotive grade GPS receiver, GSNRx™ and GSNRx-hs™ integrated with different sensor setups. However the focus is on the integration results using GSNRx-hs™ receiver.

Table 3.23 and Table 3.24 show the position, velocity and attitude error obtained from the loose integration of the automotive grade GPS receiver and vehicle sensors in the urban canyon environment. As shown in the two tables, the integrated solutions provide improved performance over the GPS only solution. WSS/2A1G provides the best performance although its improvement over other sensor setups is small in this case.

Table 3.23: Summarized RMS position and velocity errors with loose integration using automotive grade GPS receiver in the urban canyon test

	Position (m)			Velocity (m/s)		
	East	North	Up	East	North	Up
RWSS	9.0	10.2	21.6	0.19	0.29	0.09
RWSS/YRS	7.9	9.7	21.6	0.17	0.23	0.14
RWSS/1A1G	7.6	10.1	18.0	0.17	0.24	0.14
WSS/1A1G	7.6	10.1	18.0	0.17	0.24	0.14
WSS/2A1G	7.2	9.6	18.0	0.17	0.23	0.10

Table 3.24: Summarized RMS attitude errors with loose integration using automotive grade GPS receiver in the urban canyon test

	Pitch (deg)	Roll (deg)	Azimuth (deg)
RWSS	1.91	N/A	4.72
RWSS/YRS	2.18	N/A	4.11
RWSS/1A1G	0.52	N/A	4.12
WSS/1A1G	0.51	N/A	4.12
WSS/2A1G	0.67	0.64	3.54

The results from the loose integration of GSNRx^{TM} and WSS/2A1G are shown in Table 3.25. Due to the relatively poor GPS solution from GSNRx^{TM} in the urban canyon

environment, the loose integrated solution still provides poor performance in this case. It is noted that the results shown in the table are inferior to those of the automotive grade GPS receiver. This suggests that the loose integration of GSNRx^{TM} cannot meet the requirement of the application.

Table 3.25: Summarized RMS position and velocity errors with loose integration using GSNRx^{TM} receiver in the urban canyon test

Position (m)			Velocity (m/s)			Attitude (deg)		
East	North	Up	East	North	Up	Pitch	Roll	Azimuth
23.2	13.9	2.8	0.28	0.26	0.07	1.06	0.64	3.89

For the loose integration of GSNRx-hs^{TM}, results similar to those of the standard GSNRx^{TM} are obtained. Table 3.26 summarize the results from the loose integration of WSS/2A1G. Minimal improvement is obtained by using loose integration. Therefore this indicates that tight or ultra-tight integration is required for severely degraded signal environments such as urban canyons.

Table 3.26: Summarized RMS position and velocity errors with loose integration using GSNRx^{TM} receiver in the urban canyon test

Position (m)			Velocity (m/s)			Attitude (deg)		
East	North	Up	East	North	Up	Pitch	Roll	Azimuth
19.8	16.6	5.0	0.30	0.25	0.07	1.03	0.64	3.74

3.4.2.2 Tight Integration Results

Similar to the foliage test analysis, the loose integration results presented are from the automotive grade GPS receiver, GSNRx™ and GSNRx-hs™ integrated with different sensor setups. Again the focus is on the integration results using GSNRx-hs™ receiver.

Table 3.27: Summarized RMS position and velocity errors with tight integration using automotive grade GPS receiver in the urban canyon test

	Position (m)			Velocity (m/s)		
	East	North	Up	East	North	Up
RWSS	8.7	9.2	6.3	0.08	0.11	0.10
RWSS/YRS	5.1	9.7	7.6	0.07	0.10	0.10
RWSS/1A1G	4.8	7.1	7.7	0.07	0.10	0.09
WSS/1A1G	4.7	6.2	7.7	0.07	0.09	0.09
WSS/2A1G	4.5	6.3	7.0	0.09	0.10	0.09

Table 3.28: Summarized RMS attitude errors with tight integration using the automotive grade GPS receiver in the urban canyon test

	Pitch (deg)	Roll (deg)	Azimuth (deg)
RWSS	1.93	N/A	1.72
RWSS/YRS	1.91	N/A	1.51
RWSS/1A1G	0.71	N/A	1.22
WSS/1A1G	0.71	N/A	1.01
WSS/2A1G	0.67	0.53	1.35

Table 3.27 and Table 3.28 show the position, velocity and attitude error obtained from the loose integration of the automotive grade GPS receiver and vehicle sensors in the urban canyon environment. As shown in the two tables, the integrated solutions provide improved

performance over the GPS only solution. WSS/2A1G provides the best performance although its improvement over other sensor setups is small.

Table 3.29: Summarized RMS position and velocity errors with tight integration using GSNRx™ receiver in the urban canyon test

	Position (m)			Velocity (m/s)		
	East	North	Up	East	North	Up
RWSS	5.1	6.7	7.5	0.08	0.08	0.07
RWSS/YRS	4.8	6.7	7.5	0.07	0.08	0.07
RWSS/1A1G	5.0	6.7	8.7	0.07	0.08	0.08
WSS/1A1G	5.3	5.8	8.9	0.07	0.08	0.08
WSS/2A1G	2.7	4.4	2.7	0.07	0.08	0.09

Table 3.30: Summarized RMS attitude errors with tight integration using GSNRx™ in the urban canyon test

	Pitch (deg)	Roll (deg)	Azimuth (deg)
RWSS	1.93	N/A	1.56
RWSS/YRS	1.91	N/A	1.35
RWSS/1A1G	0.84	N/A	1.30
WSS/1A1G	0.83	N/A	1.02
WSS/2A1G	0.71	0.53	1.02

Table 3.29 and Table 3.30 show the results from the tight integration of the standard GSNRx™ receiver and vehicle sensors. The tight integration solution with GSNRx™ provides noticeably improved position and velocity accuracies compared with its loose integration results. This is mainly due to the improved blunder detection reliability using

the tight integration solution. It is also noted that the WSS/2A1G sensor setup provides the best performance and obtains within 5 m RMS error in this case.

Table 3.31: Summarized RMS position and velocity errors with tight integration using GSNRx-hs™ receiver in the urban canyon test

	Position (m)			Velocity (m/s)		
	East	North	Up	East	North	Up
RWSS	6.2	4.5	9.1	0.08	0.08	0.07
RWSS/YRS	5.2	3.5	9.2	0.07	0.08	0.07
RWSS/1A1G	6.2	2.5	9.8	0.07	0.07	0.07
WSS/1A1G	5.1	1.8	9.8	0.07	0.07	0.07
WSS/2A1G	5.0	1.7	3.8	0.07	0.07	0.07

Table 3.32: Summarized RMS attitude errors with tight integration using GSNRx-hs™ in the urban canyon test

	Pitch (deg)	Roll (deg)	Azimuth (deg)
RWSS	1.92	N/A	1.92
RWSS/YRS	1.90	N/A	1.37
RWSS/1A1G	0.91	N/A	1.32
WSS/1A1G	0.88	N/A	1.15
WSS/2A1G	0.76	0.54	1.15

Table 3.22 and Table 3.32 summarize the results from the tight integration with the GSNRx-hs™ GPS receiver. Similar to the tight integration with the automotive grade GPS receiver, noticeable improvement is achieved when using tight integration. And it is also

noted that the WSS/2A1G setup offers the best performance over the other sensor setup although its improvement is quite minimal.

In summary, the tight integration of the three receivers with vehicle sensor outperforms their loose integration solutions. The WSS/2A1G sensor setup provides the best performance among the all sensor setups. From the results described above, it is recommended to use the WSS/1A1G or WSS/2A1G sensor setup in the urban canyon environments to provide reliable navigation solution.

3.4.3 DR Only Operation

Finally, the performance of the DR based system is evaluated when GPS updates are not available. Figure 3.10 shows the horizontal position error as a function of travelled distance for DR based system with the WSS/1A1G sensor setup from 30 runs. After 6000 m of free running, the maximum horizontal position error is 153 m, which translates the accuracy 2.6% of distance travelled. It noted that errors are shown in this figure are systematic and correlated between runs, especially after 3000 m. This is mainly due to the fact that the 30 runs used the same data set except the start time was separated by 10 seconds.

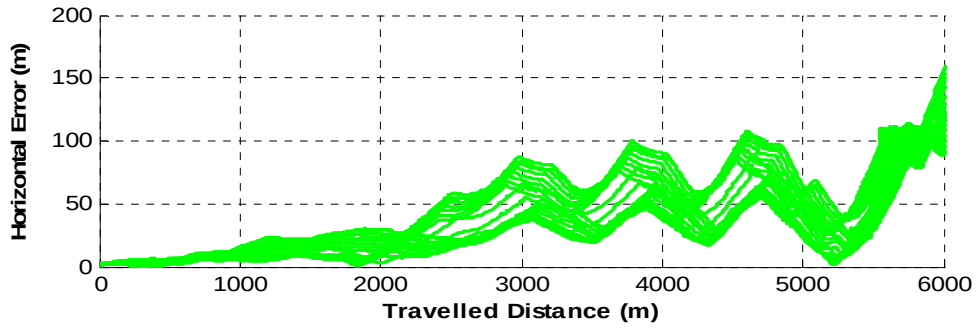

Figure 3.10: Horizontal position error as function of travelled distance

Table 3.33: Summarized maximum position errors as a function of travelled distance

	Horizontal (Percentage)	Vertical (Percentage)
RWSS	4.0%	0.2%
RWSS/YRS	3.1%	0.2%
RWSS/1A1G	2.6%	0.1%
WSS/1A1G	2.6%	0.1%
WSS/2A1G	2.4%	0.1%

Table 3.33 summaries the maximum horizontal and vertical position errors from 30 runs of different sensors. According to the results listed in the table, the DR algorithms with pitch and roll compensations provide improved navigation performance without GPS updates.

CHAPTER FOUR: IN-MOTION ALIGNMENT WITH LARGE HEADING UNCERTAINTY

The strapdown INS and DR require an initialization process that establishes the relationship between the vehicle body frame and the navigation frame. This process, called alignment, generally requires the vehicle to remain stationary for some period of time in order to establish this initial state (Rogers 2007). Its purpose is to bring the initial attitude error down to a magnitude that is adequate for free-inertial or free dead reckoning navigation or is consistent with the small error assumption used by an integrated Kalman filter. Since the pitch and roll of a vehicle are usually less than 5 degrees, the alignment process for the land vehicle applications is mainly focused on the heading alignment.

Traditional alignment requires that the vehicle should be stationary and the gyros have to sense the earth rotation rate (Rogers 2007). But in practice, it is not realistic to spend a couple of minutes on the system alignment. Furthermore, the low cost MEMS yaw rate sensors used in this work have relatively large bias and instability, which make it difficult to perform the alignment in a traditional way.

GPS information can be used to align the IMU without the static requirement, which is called in-motion alignment (Rogers 2007, Hong et al 2004). However, traditional in-motion alignment still requires the knowledge of heading within a 10-degree accuracy (Rogers 2007). This is not feasible for a land vehicle navigation application where the initial heading information is not available unless adding digital compasses, magnetometers or other sensors. However, augmenting the additional sensors (e.g. digital

compasses or magnetometers) not only increases the system cost but also increases the system complexity. Furthermore, digital compasses or magnetometers are vulnerable to magnet interference and would result in significant heading errors. Therefore, the in-motion alignment algorithm using GPS measurements without any initial heading information is proposed in this thesis. Instead of the small angle assumptions used in the traditional alignment algorithm, the large heading uncertainty model with two states representing the heading error is used. Thus the magnitude of the initial azimuth error could reach as much as 180 degrees compared with 5 to 10 degrees for a conventional INS or DR error model.

4.1 INS Mechanization based In-motion Alignment

Similar to the system models presented in Chapter 2, the error models used for the in-motion alignment can be categorized into the INS mechanization based and DR based models. This section starts with the INS mechanization based in-motion alignment algorithm. The sensor setup used herein is the 2A1G configuration. The alignment algorithm presented in this section applied pseudo-signal approach for the simplicity.

Generally the heading error is much larger than the leveling errors in the alignment process, thus the horizontal frame (h-frame) is used to separate the heading error and leveling error. For details of the frame definition refer to Appendix A. Assuming small pitch and roll angles and the large heading uncertainty, the estimated rotation matrix from the body frame to the navigation frame $\hat{R}_h^n$ can be expressed by

$$\hat{R}_b^h = \left[I + \langle \boldsymbol{\varepsilon}_L \times \rangle\right] R_b^h = \begin{bmatrix} 0 & 0 & \varepsilon_y \\ 0 & 0 & -\varepsilon_x \\ -\varepsilon_y & \varepsilon_x & 0 \end{bmatrix} R_b^h \tag{4.1}$$

where

$$R_b^h = R_1(-\theta)R_2(-\phi) = \begin{bmatrix} 1 & 0 & 0 \\ 0 & \cos\theta & -\sin\theta \\ 0 & \sin\theta & \cos\theta \end{bmatrix} \begin{bmatrix} \cos\phi & 0 & \sin\phi \\ 0 & 1 & 0 \\ -\sin\phi & 0 & \cos\phi \end{bmatrix}$$
$$= \begin{bmatrix} \cos\phi & 0 & \sin\phi \\ \sin\theta\sin\phi & \cos\theta & -\sin\theta\cos\phi \\ -\cos\theta\sin\phi & \sin\theta & \cos\theta\cos\phi \end{bmatrix}$$

$\boldsymbol{\varepsilon}_L$ is the leveling error.

The error of rotation matrix from h-frame to n-frame due to large heading error can be linearized as

$$\delta R_h^n = \begin{bmatrix} \delta\cos\psi & \delta\sin\psi & 0 \\ -\delta\sin\psi & \delta\cos\psi & 0 \\ 0 & 0 & 0 \end{bmatrix} \tag{4.2}$$

Thus, neglecting second order error terms, δR_b^n can be given by

$$\begin{aligned} \delta R_b^n &= \hat{R}_b^n - R_b^n = \hat{R}_h^n \hat{R}_b^h - R_b^n = (R_h^n + \delta R_h^n)[\mathbf{I} + \langle \boldsymbol{\varepsilon}_L \times \rangle] R_b^h - R_b^n \\ &\approx [R_h^n \langle \boldsymbol{\varepsilon}_L \times \rangle + \delta R_h^n] R_b^h = \mathbf{E} R_b^h \end{aligned} \tag{4.3}$$

The $\mathbf{E}$ matrix in Equation (6) is defined as

$$
\begin{aligned}
\mathbf{E} &= \delta R_h^n + R_h^n \langle \boldsymbol{\varepsilon}_L \times \rangle \\
&= \begin{bmatrix} \delta\cos\psi & \delta\sin\psi & 0 \\ -\delta\sin\psi & \delta\cos\psi & 0 \\ 0 & 0 & 0 \end{bmatrix} + \begin{bmatrix} \cos\psi & \sin\psi & 0 \\ -\sin\psi & \cos\psi & 0 \\ 0 & 0 & 1 \end{bmatrix} \begin{bmatrix} 0 & 0 & \varepsilon_y \\ 0 & 0 & -\varepsilon_x \\ -\varepsilon_y & \varepsilon_x & 0 \end{bmatrix} \\
&= \begin{bmatrix} \delta\cos\psi & \delta\sin\psi & \cos\psi\varepsilon_y - \sin\psi\varepsilon_y \\ -\delta\sin\psi & \delta\cos\psi & -\sin\psi\varepsilon_y + \cos\psi\varepsilon_x \\ -\varepsilon_y & \varepsilon_x & 0 \end{bmatrix}
\end{aligned} \tag{4.4}
$$

By differentiating Equation (4.4), the following equation can be obtained

$$
\delta\dot{R}_b^n = \dot{\mathbf{E}} R_b^h + \mathbf{E}\dot{R}_b^h = \dot{\mathbf{E}} R_b^h + \mathbf{E} R_b^h \boldsymbol{\Omega}_{hb}^b = \dot{\mathbf{E}} R_b^h + \mathbf{E} R_b^h \boldsymbol{\Omega}_{hb}^b R_h^b R_b^h = \dot{\mathbf{E}} R_b^h + \mathbf{E}\boldsymbol{\Omega}_{hb}^h R_b^h \tag{4.5}
$$

On the other hand, $\delta\dot{R}_b^n$ can be obtained by

$$
\begin{aligned}
\delta\dot{R}_b^n &= \dot{\hat{R}}_b^n - \dot{R}_b^n = \hat{R}_b^n \hat{\boldsymbol{\Omega}}_{nb}^b - R_b^n \boldsymbol{\Omega}_{nb}^b = \hat{R}_h^n \hat{R}_b^h \hat{\boldsymbol{\Omega}}_{nb}^b - R_b^n \boldsymbol{\Omega}_{nb}^b \\
&\approx (R_h^n + \delta R_h^n)[\mathbf{I} + \langle \boldsymbol{\varepsilon}_L \times \rangle] R_b^h (\boldsymbol{\Omega}_{nb}^b + \delta\boldsymbol{\Omega}_{nb}^b) - R_b^n \boldsymbol{\Omega}_{nb}^b \\
&= [R_h^n \langle \boldsymbol{\varepsilon}_L \times \rangle + \delta R_h^n] R_b^h \boldsymbol{\Omega}_{nb}^b R_h^b R_b^h + R_h^n R_b^h \delta\boldsymbol{\Omega}_{nb}^b R_h^b R_b^h \\
&= [R_h^n \langle \boldsymbol{\varepsilon}_L \times \rangle + \delta R_h^n] \boldsymbol{\Omega}_{nb}^h R_b^h + R_h^n \delta\boldsymbol{\Omega}_{nb}^h R_b^h \\
&= (\mathbf{E}\Omega_{nb}^h + R_h^n \delta\boldsymbol{\Omega}_{nb}^h) R_b^h
\end{aligned} \tag{4.6}
$$

Equating Equation (4.5) and Equation (4.6), we can obtain

$$
\dot{\mathbf{E}} + \mathbf{E}\boldsymbol{\Omega}_{hb}^h = \mathbf{E}\boldsymbol{\Omega}_{nb}^h + R_h^n \delta\boldsymbol{\Omega}_{nb}^h \tag{4.7}
$$

Thus

$$
\dot{\mathbf{E}} = \mathbf{E}\boldsymbol{\Omega}_{nb}^h - \mathbf{E}\boldsymbol{\Omega}_{hb}^h + R_h^n \delta\boldsymbol{\Omega}_{nb}^h = \mathbf{E}(\boldsymbol{\Omega}_{nb}^h - \boldsymbol{\Omega}_{hb}^h) + \delta\boldsymbol{\Omega}_{nb}^n R_h^n = \mathbf{E}\boldsymbol{\Omega}_{nh}^h + \delta\boldsymbol{\Omega}_{nb}^n R_h^n \tag{4.8}
$$

where

$$
\Omega_{nh}^h = \begin{bmatrix} 0 & \dot{\psi} & 0 \\ -\dot{\psi} & 0 & 0 \\ 0 & 0 & 0 \end{bmatrix};
$$

$$
\delta\omega_{nb}^n = R_b^n \delta\omega_{ib}^b - \delta\omega_{in}^n = \begin{bmatrix} \delta\omega_E & \delta\omega_N & \delta\omega_U \end{bmatrix}^T .
$$

$\delta\omega_{in}^n$ is given by (Jekeli 2002):

$$\delta\omega_{in}^{n}=\begin{bmatrix} 0 & 0 & \dfrac{\dot{\varphi}}{N+h} \\ -\omega_{ie}\sin\varphi & 0 & -\dfrac{\dot{\lambda}\cos\varphi}{N+h} \\ \omega_{ie}\cos\varphi+\dfrac{\dot{\lambda}}{\cos\varphi} & 0 & -\dfrac{\dot{\lambda}\sin\varphi}{N+h} \end{bmatrix}\begin{bmatrix}\delta\varphi\\ \delta\lambda\\ \delta h\end{bmatrix}+\begin{bmatrix} 0 & -\dfrac{1}{M+h} & 0 \\ \dfrac{1}{N+h} & 0 & 0 \\ \dfrac{\tan\varphi}{N+h} & 0 & 0 \end{bmatrix}\begin{bmatrix}\delta V_E\\ \delta V_N\\ \delta V_U\end{bmatrix}$$

Therefore, the attitude error matrix can be reformulated as

$$\begin{aligned}\dot{E} &= E\Omega_{nh}^{h}+\delta\Omega_{nb}^{n}R_{h}^{n}\\ &=\begin{bmatrix}\delta\cos\psi & \delta\sin\psi & \cos\psi\varepsilon_y-\sin\psi\varepsilon_x\\ -\delta\sin\psi & \delta\cos\psi & -\sin\psi\varepsilon_y+\cos\psi\varepsilon_x\\ -\varepsilon_y & \varepsilon_x & 0\end{bmatrix}\begin{bmatrix}0 & \dot{\psi} & 0\\ -\dot{\psi} & 0 & 0\\ 0 & 0 & 0\end{bmatrix}\\ &+\begin{bmatrix}0 & -\delta\omega_U & \delta\omega_U\\ \delta\omega_U & 0 & -\delta\omega_E\\ -\delta\omega_N & \delta\omega_E & 0\end{bmatrix}\begin{bmatrix}\cos\psi & \sin\psi & 0\\ -\sin\psi & \cos\psi & 0\\ 0 & 0 & 1\end{bmatrix}\end{aligned} \tag{4.9}$$

Finally, the attitude error equation can be given by

$$\delta\sin\psi'=\delta\cos\psi\dot{\psi}-\delta\omega_U\cos\psi \tag{4.10}$$

$$\delta\cos\psi'=-\delta\sin\psi\dot{\psi}+\delta\omega_U\sin\psi \tag{4.11}$$

$$\dot{\varepsilon}_x=-\varepsilon_y\dot{\psi}-\delta\omega_N\sin\psi+\delta\omega_E\cos\psi \tag{4.12}$$

$$\dot{\varepsilon}_y=-\varepsilon_x\dot{\psi}+\delta\omega_N\cos\psi+\delta\omega_E\sin\psi \tag{4.13}$$

Given the attitude error equations, the velocity error can be obtained by

$$\delta\dot{\mathbf{v}}^{n}=\mathbf{E}R_{b}^{h}\mathbf{f}^{b}+R_{b}^{n}\mathbf{b}-(2\boldsymbol{\Omega}_{ie}^{n}+\boldsymbol{\Omega}_{en}^{n})\delta\mathbf{v}^{n}-(2\delta\boldsymbol{\Omega}_{ie}^{n}+\delta\boldsymbol{\Omega}_{en}^{n})\mathbf{v}^{n}+\delta\mathbf{g}^{n} \tag{4.14}$$

where

$$\mathbf{ER}_b^h\mathbf{f}^b = \begin{bmatrix} \delta\cos\psi & \delta\sin\psi & \cos\psi\varepsilon_y - \sin\psi\varepsilon_x \\ -\delta\sin\psi & \delta\cos\psi & -\sin\psi\varepsilon_y + \cos\psi\varepsilon_x \\ -\varepsilon_y & \varepsilon_x & 0 \end{bmatrix}\begin{bmatrix} f_x^h \\ f_y^h \\ f_z^h \end{bmatrix}$$
$$= \begin{bmatrix} -f_z^h\sin\psi & f_z^h\cos\psi \\ -f_z^h\cos\psi & f_z^h\sin\psi \\ f_y^h & -f_x^h \end{bmatrix}\begin{bmatrix} \varepsilon_x \\ \varepsilon_y \end{bmatrix} + \begin{bmatrix} f_y^h & f_x^h \\ -f_x^h & f_y^h \\ 0 & 0 \end{bmatrix}\begin{bmatrix} \delta\sin\psi \\ \delta\cos\psi \end{bmatrix}$$

The loose integration of GPS/2A1G is used for the in-motion alignment in this case. Therefore the system error states can be expressed as,

$$\mathbf{dx} = \begin{bmatrix} \delta\mathbf{r}^n & \delta\mathbf{V}^n & \boldsymbol{\varepsilon}^h & \boldsymbol{\alpha} & \mathbf{b} & \mathbf{d} \end{bmatrix}^T \tag{4.15}$$

where $\boldsymbol{\alpha} = \begin{bmatrix} \delta\sin\psi & \delta\cos\psi \end{bmatrix}^T$. The corresponding error model for the local terrain predictor is given by

$$\begin{bmatrix} \delta\dot{\mathbf{r}}^n \\ \delta\dot{\mathbf{V}}^n \\ \dot{\boldsymbol{\varepsilon}}_L^h \\ \dot{\boldsymbol{\alpha}} \\ \dot{\mathbf{b}} \\ \dot{\mathbf{d}} \end{bmatrix} = \begin{bmatrix} 0_{3\times3} & \mathbf{I} & 0_{3\times2} & 0_{3\times2} & 0_{3\times3} & 0_{3\times3} \\ 0_{3\times3} & \mathbf{B} & \mathbf{F}_{v\varepsilon} & \mathbf{F}_{v\alpha} & R_b^n & 0_{3\times3} \\ 0_{2\times3} & \mathbf{F}_{\varepsilon v} & \mathbf{F}_{\varepsilon\varepsilon} & 0_{2\times2} & 0_{2\times3} & 0_{2\times3} \\ 0_{2\times3} & \mathbf{F}_{\alpha v} & 0_{2\times2} & \mathbf{F}_{\alpha\alpha} & 0_{2\times3} & \mathbf{F}_{\alpha d} \\ 0_{3\times3} & 0_{3\times3} & 0_{3\times2} & 0_{3\times2} & -\boldsymbol{\Lambda} & 0_{3\times3} \\ 0_{3\times3} & 0_{3\times3} & 0_{3\times2} & 0_{3\times2} & 0_{3\times3} & -\boldsymbol{\Gamma} \end{bmatrix}\begin{bmatrix} \delta\mathbf{r}^n \\ \delta\mathbf{V}^n \\ \boldsymbol{\varepsilon}_L^h \\ \boldsymbol{\alpha} \\ \mathbf{b} \\ \mathbf{d} \end{bmatrix} + \begin{bmatrix} 0_{3\times1} \\ 0_{3\times1} \\ 0_{2\times1} \\ 0_{2\times1} \\ \mathbf{W}_b \\ \mathbf{W}_d \end{bmatrix} \tag{4.16}$$

where

$$F_{v\varepsilon} = \begin{bmatrix} -f_z^h\sin\psi & f_z^h\cos\psi \\ -f_z^h\cos\psi & f_z^h\sin\psi \\ f_y^h & -f_x^h \end{bmatrix};$$

$$F_{v\alpha} = \begin{bmatrix} f_y^h & f_x^h \\ -f_x^h & f_y^h \\ 0 & 0 \end{bmatrix};$$

$$F_{\varepsilon v} = \begin{bmatrix} \dfrac{\sin\psi}{N+h} & \dfrac{\cos\psi}{M+h} & 0 \\ -\dfrac{\cos\psi}{N+h} & \dfrac{\sin\psi}{M+h} & 0 \end{bmatrix};$$

$$F_{\varepsilon\varepsilon} = \begin{bmatrix} 0 & -\dot{\psi} \\ \dot{\psi} & 0 \end{bmatrix}$$

$$F_{\varepsilon d} = \begin{bmatrix} \cos\psi & -\sin\psi \\ \sin\psi & \cos\psi \end{bmatrix} \begin{bmatrix} 1 & 0 & 0 \\ 0 & 1 & 0 \end{bmatrix} R_b^n$$

$$F_{\alpha v} = \begin{bmatrix} \dfrac{\tan\varphi\cos\psi}{N+h} & 0 & 0 \\ -\dfrac{\tan\varphi\sin\psi}{N+h} & 0 & 0 \end{bmatrix};$$

$$F_{\alpha\alpha} = \begin{bmatrix} 0 & \dot{\psi} \\ -\dot{\psi} & 0 \end{bmatrix};$$

$$F_{\alpha d} = \begin{bmatrix} 0 & 0 & -\cos\psi \\ 0 & 0 & \sin\psi \end{bmatrix} R_b^n;$$

$\mathbf{W}_d$ is the driving noise of the gyro drifts.

4.2 DR based In-motion Alignment

In order to perform in-motion alignment of the DR based system without knowing the initial attitude information, a new in-motion alignment algorithm is proposed. Similar as the INS mechanization based error model for the in-motion alignment, the DR based alignment also applies $\delta\sin\psi$ and $\delta\cos\psi$ to linearize the large heading error. For the simplicity, the DR based in-motion alignment applies WSS/SAS/2A1G sensor setup. Thus the system error state in this case is given by

$$\mathbf{dx} = \begin{bmatrix} \delta\mathbf{r}^n & \delta\mathbf{V}^b & \delta a_x^b & \delta a_y^b & \boldsymbol{\varepsilon}_L^h & \boldsymbol{\alpha} & \delta\mathbf{S} & b_x & \delta\mathbf{S}_{rl} & \delta\mathbf{S}_{rr} & b_y & d_{YRS} & \delta\psi_l & \delta\psi_r \end{bmatrix}^T \quad 4.17$$

where $\boldsymbol{\alpha} = \begin{bmatrix} \delta\sin\psi & \delta\cos\psi \end{bmatrix}$.

In this case, the position error states can be derived as

$$\delta\dot{\mathbf{r}}^n = R_b^n \delta\mathbf{V}^b + \delta R_b^n \mathbf{V}^b \quad 4.18$$

Substituting Equation (4.3) into the above equation,

$$\begin{aligned} \delta\dot{\mathbf{r}}^n &= R_b^n \delta\mathbf{V}^b + \mathbf{E} R_b^h \mathbf{V}^b \\ &= R_b^n \delta\mathbf{V}^b + \begin{bmatrix} -V_z^h \sin\psi & V_z^h \cos\psi \\ -V_z^h \cos\psi & V_z^h \sin\psi \\ V_y^h & -V_x^h \end{bmatrix} \begin{bmatrix} \varepsilon_x \\ \varepsilon_y \end{bmatrix} + \begin{bmatrix} V_y^h & V_x^h \\ -V_x^h & V_y^h \\ 0 & 0 \end{bmatrix} \begin{bmatrix} \delta\sin\psi \\ \delta\cos\psi \end{bmatrix} \end{aligned} \quad 4.19$$

where $\begin{bmatrix} V_x^h & V_y^h & V_z^h \end{bmatrix}^T = R_b^h \begin{bmatrix} V_x^b & V_y^b & V_z^b \end{bmatrix}^T$.

Similar derivation as the INS mechanization based in-motion alignment for the large heading uncertainty is used. Thus the attitude error states in this case can be expressed as

$$\begin{bmatrix} \dot{\boldsymbol{\varepsilon}}_L^h \\ \dot{\boldsymbol{\alpha}}^h \end{bmatrix} = \begin{bmatrix} \dot{\varepsilon}_x \\ \dot{\varepsilon}_y \\ d\delta\sin\psi \\ d\delta\cos\psi \end{bmatrix} = \begin{bmatrix} -\alpha_\theta & 0 & 0 & 0 \\ 0 & -\alpha_\phi & 0 & 0 \\ 0 & 0 & 0 & \dot{\psi} \\ 0 & 0 & -\dot{\psi} & 0 \end{bmatrix} \begin{bmatrix} \varepsilon_x \\ \varepsilon_y \\ \delta\sin\psi \\ \delta\cos\psi \end{bmatrix} + \begin{bmatrix} 0 \\ 0 \\ \cos\psi \\ -\sin\psi \end{bmatrix} \delta\ddot{\psi} \quad 4.20$$

The other states are the same as the error equations presented in Section 3.1.7, thus are not presented in detail here.

4.3 Processing Strategy

In order to verify the feasibility and analyze the performance of the in-motion alignment algorithm, the data collected under the suburban and foliage scenario were used here. The details of the equipment setup and test environment are described in Section 2.4.1.1 and 2.4.1.2. The accuracy of the reference solution has been also presented in Section 2.4.1.3.

To test the performance of the large heading uncertainty model, the initial heading is setup with the error of 0^o , 10^o , 90^o , 180^o respectively. Both the heading convergence speed and the estimated accuracy are considered as the criteria for the performance analysis. Since loose integration is used for the in-motion alignment algorithms, the 3D position and velocity from GSNRx-hs^{TM} is used to update the integration filter. Both the INS mechanization based and DR based in-motion alignment algorithms are used for the analysis. Furthermore, the results without using large heading uncertainty model are also used for the comparison purposes.

4.4 Results and Performance Analysis

In order to verify the feasibility and analyze the performance of the in-motion alignment algorithm, the field test under the suburban and foliage scenario were used here (see Sections 2.4.1.1 and 2.4.1.1). The first set of results is obtained when the initial azimuth error was set to zero degrees.

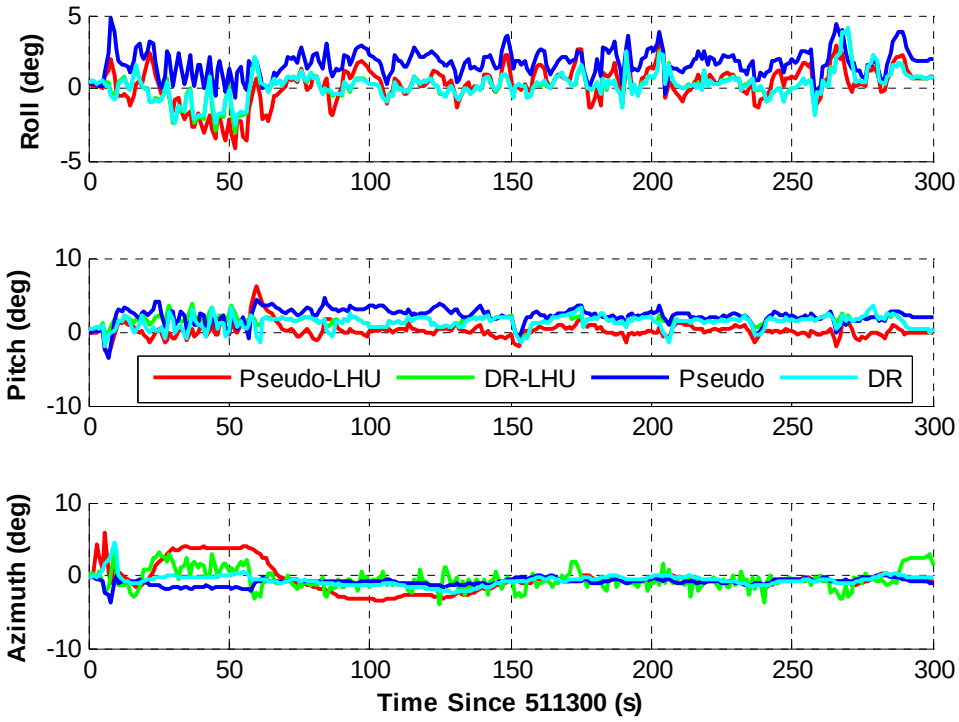

Figure 4.1: Attitude error plots for the in-motion alignment with 0 deg initial azimuth error

The initial 300 seconds results using in-motion alignment algorithms are shown in Figure 4.1. It is noted that the convergence of the in-motion alignment does not require 300 s. The figure plotted here merely shows the results during the initial 300 s period. For both the pseudo-signal with a large heading uncertainty model (denoted as "Pseudo-LHU") and DR with a large heading uncertainty model (denoted as "DR-LHU"), the attitude errors are within 5 deg during the test. However, compared with the results from the pseudo-signal and DR algorithms with a small attitude error model (denoted as "pseudo" and "DR" respectively), the in-motion alignment algorithms using large heading uncertainty model demonstrates relatively large variations for the azimuth error. Thus, after the in-motion

alignment procedure is complete, it is recommended to use the conventional small attitude error model as soon as possible thereafter.

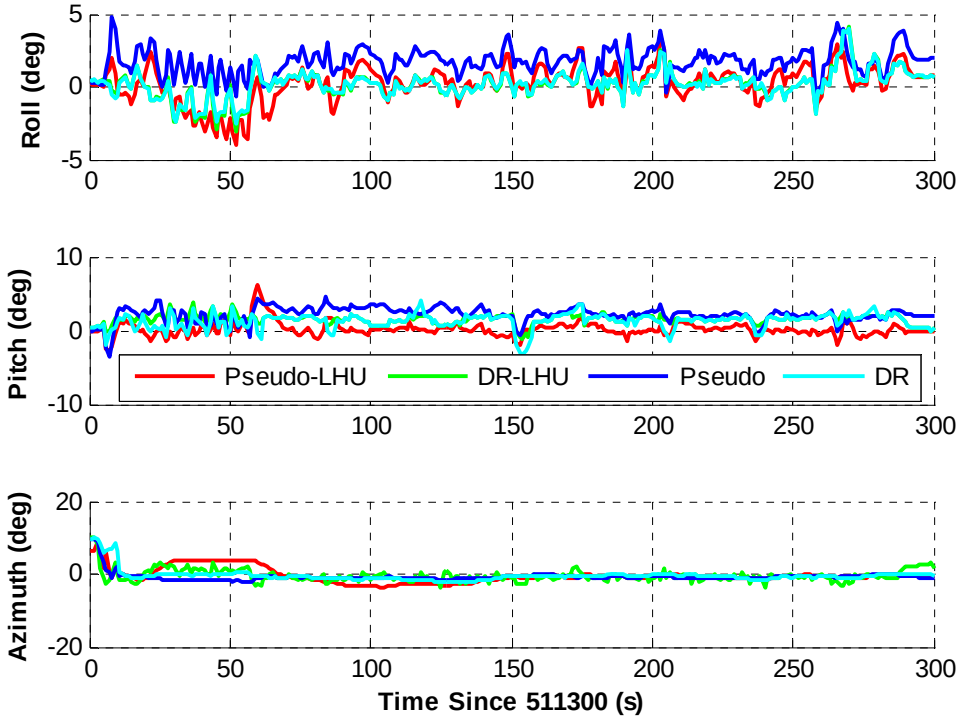

Figure 4.2: Attitude error plots for the in-motion alignment with a 10 deg initial azimuth error

Figure 4.2 shows the attitude error when the initial azimuth error is 10 deg. Results similar to that of the 0 deg initial azimuth error case were obtained. The pseudo-signal and DR based algorithms with a small attitude error model performs better than their large heading uncertainty versions in terms of the attitude error. It is expected as an initial 10 deg azimuth error still fits the small attitude error model very well. Therefore, the large heading uncertainty model does not have any advantages when the initial azimuth error is relatively small.

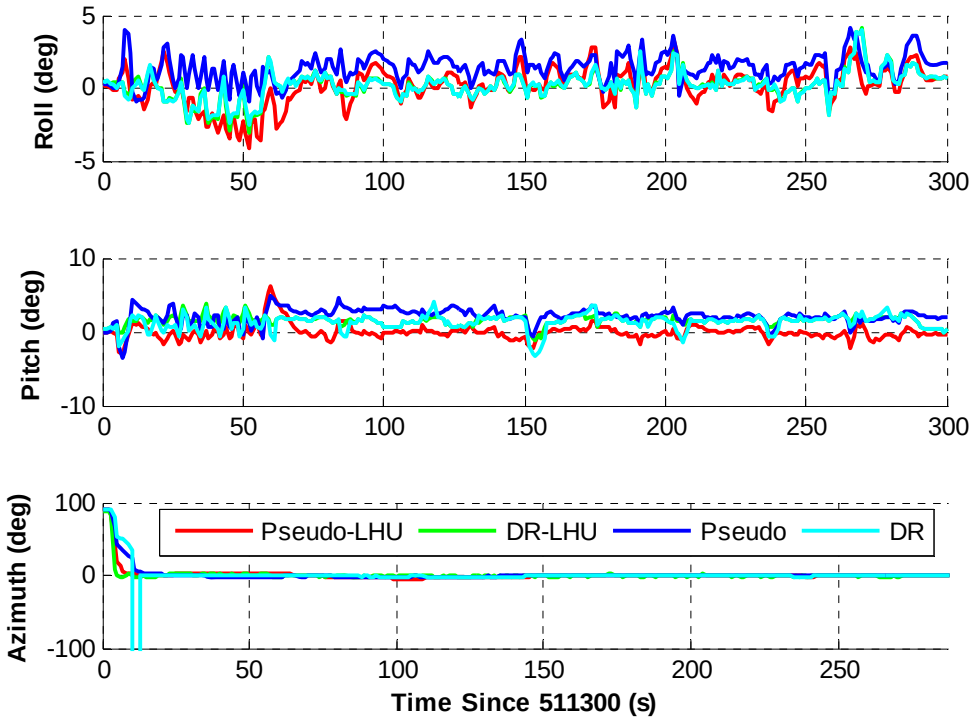

Figure 4.3: Attitude error plots for the in-motion alignment with a 90 deg initial azimuth error

When the initial azimuth error is as large as 90 deg, the benefits of using a large heading uncertainty model becomes noticeable. As shown in Figure 4.3, both Pseudo-LHU and DR-LHU converge to a 5 deg azimuth error after 5 seconds. However, the convergence speed for the algorithms with the small attitude error model is over 15 seconds. Thus over a 66% improvement can be obtained when using a large heading uncertainty model.

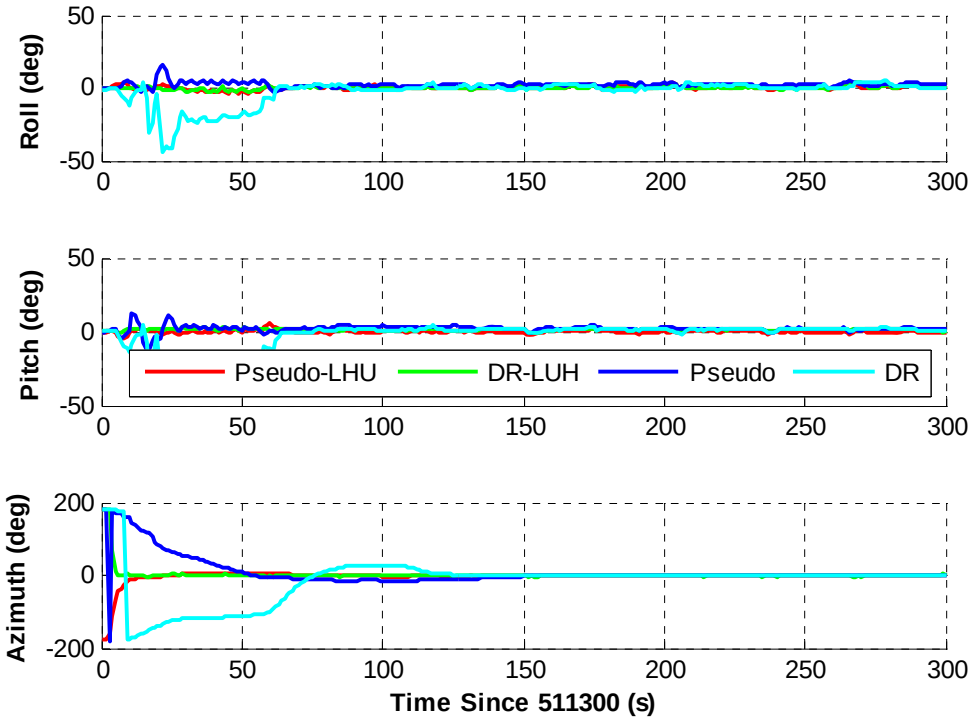

Figure 4.4: Attitude error plots for the in-motion alignment with a 180 deg initial azimuth error

Finally, the worst case is when the initial azimuth error is 180 deg. In this case, the true heading is completely opposite to the initial heading. As shown in Figure 4.4, it a takes a very long time for the pseudo-signal approach and DR with the small attitude error model to converge to the right azimuth. Furthermore, the pitch and roll estimates are also contaminated by the large azimuth error. However, when using the large heading uncertainty model, both the pseudo-signal and DR based algorithms quickly converge to the right attitude after 10 seconds.

In summary, both the pseudo-signal and DR based in-motion alignment algorithms with the large heading uncertainty model are feasible for the attitude alignment for low cost MEMS

IMUs. Field test results show that the proposed in-motion alignment algorithms take only 15 seconds to obtain azimuth estimates within a 5 deg accuracy regardless of the initial azimuth.

CHAPTER FIVE: ULTRA-TIGHT GPS AND VEHICLE SENSOR INTEGRATION USING DR

Having discussed the performance of the high sensitivity GPS receiver with block processing in Chapter 2 and the loosely and tightly coupled GPS and vehicle sensor integration in Chapter 3, this chapter takes a further step to discuss the ultra-tightly coupled GPS and vehicle sensor integration. As presented in Chapter 3, the proposed DR based algorithms provide more reliable and accurate navigation solutions in degraded signal environments. Thus the DR based integration algorithms is the focus of this chapter.

5.1 Ultra-tight GPS/DR Receiver Architecture

The ultra-tight GPS and vehicle sensor integrated system using DR algorithms is based on the vector based receiver architecture with the DR based GPS/vehicle sensor integration. Figure 5.1 shows the ultra-tight GPS receiver architecture. Compared with the vector based receiver shown in Figure 2.2, the red blocks highlight the differences. The measurements from the vehicle sensors are used in the integrated navigation solution. It is noted that different sensor configurations can be also used in the ultra-tight integration. The DR based integration filter is used to provide the navigation solution instead of the GPS only filter.

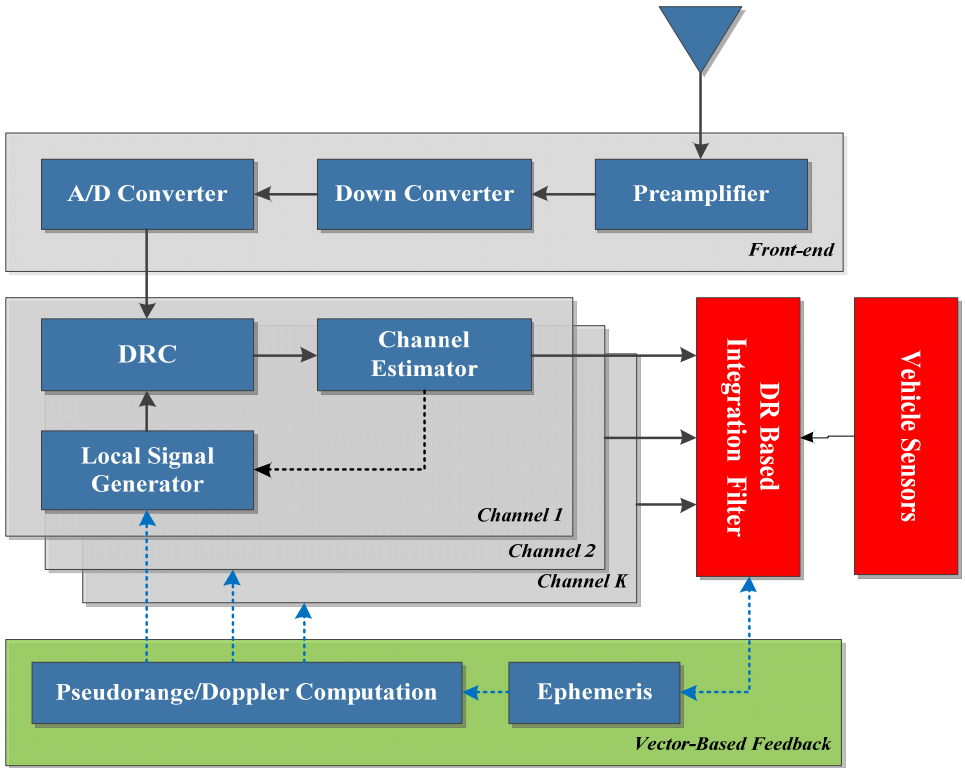

Figure 5.1: Ultra-tight GPS receiver architecture

The ultra-tight GPS receiver has better performance compared to a vector-based receiver because the high rate measurements from the vehicle sensors provides more precise information about the receiver dynamics between GPS measurement updates whereas the vector receiver would have to predict the navigation solution forward using past estimates, thus introducing additional errors. This is particularly important when coherently integrating over longer time intervals where predicting the navigation solution may introduce substantial attenuation.

It is also noted that different channel processing strategies can be used for the ultra-tight GPS receiver. Previous research used the Kalman filter processing strategy for the ultra-tight GPS/vehicle sensor integrated receiver (Li et al 2010). However, due to the

limitations of the Kalman filter based tracking strategy for high sensitivity applications as discussed in Section 2.2.2, block processing strategy is preferred here. Accordingly, the ultra-tight GPS / vehicle sensor integrated receiver using block processing strategy is proposed herein.

Figure 5.2 illustrates the block diagram of the proposed implementation of the ultra-tight GPS/DR integrated receiver using block processing strategy (GSNRx-hs-dr^{TM}). It is based on GSNRx-hs^{TM} with the DR based GPS/vehicle sensor integration filter. With the help of the DR based vehicle sensor integration, more accurate code phase and frequency can be determined for the block correlator. Reduced size of the search space can be obtained with the improved navigation solution feedback from the integration filter since the uncertainty then reduced compared to the GPS only case. Furthermore, the high rate vehicle sensor updates can be also beneficial for the possibility of using longer coherent integration time.

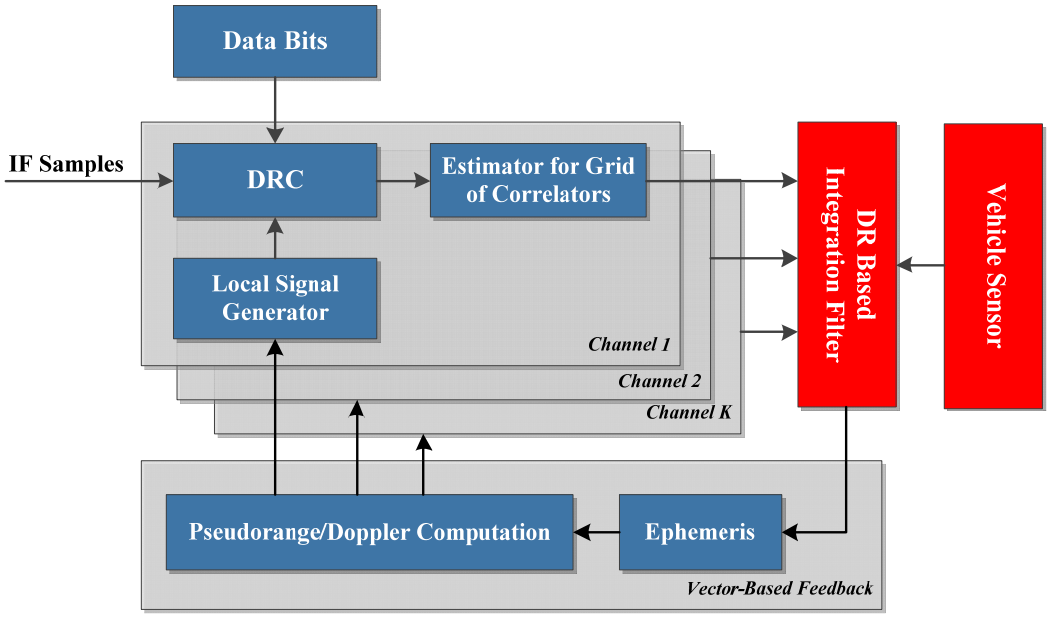

Figure 5.2: Block diagram of GSNRx-hs-dr^{TM} architecture

5.2 Field Test Results and Performance Analysis

Having explained the architecture of ultra-tightly coupled GPS/vehicle sensor integration using DR-based algorithms, two field tests were conducted to evaluate the performance of the proposed algorithms. The field tests were conducted under two scenarios: a suburban and foliage scenario and an urban canyon scenario. The test environments and equipment setup are the same as those presented in Section 2.4. Both the EKF based (GSNRx-eb-dr^{TM}) and block processing based (GSNRx-hs-dr^{TM}) ultra-tight receivers are used for the performance analysis. .

5.2.1 Foliage Scenario

The results from the foliage test are presented and evaluated in this section. The generation was described in Section 2.4.1.3 and was reported to have an accuracy of 0.5 m in position and 0.02 m/s in velocity. The performance analysis of the ultra-tight receivers will be performed in both the positioning and tracking domains.

5.2.1.1 Position Domain Performance Analysis

Firstly, the performance of the ultra-tight solutions is analyzed in the position domain. The position and velocity accuracy are used to assess the positioning performance of the various receivers.

Figure 5.3, Figure 5.4 and Figure 5.5 illustrate the position, velocity and attitude error of GSNRx-hs-dr^{TM} with the RWSS/1A1G sensor setup. Compared with the tight integration of GSNRx-hs^{TM} and RWSS/1A1G, the navigation accuracy improvement from ultra-tight

integration is unnoticeable in this test environment. In order to evaluate the performance of the ultra-tight block processing HSGPS receiver (GSNRs-hs-dr^{TM}) with different sensor setups, the RWSS, RWSS/YRS, RWSS/1A1G, WSS/SAS/1A1G and WSS/SAS/2A1G sensor setups were all used in the processing. Table 5.1 and Table 5.2 summarized the RMS positioning error and attitude error using GSNRx-hs-dr^{TM} with different sensor setups. Similar to the GSNRx-hs-dr^{TM}/RWSS/1A1G case, the results from the ultra-tight integration of other sensor setups are similar to those of tight solutions. Given the objective of the work is five metre accuracy all the sensor setups with GSNRx-dr-hs^{TM} meet the requirement. Balancing between the sensor costs and positioning accuracy, the RWSS/1A1G sensor setup is more appropriate since adding other sensors does not provide significant performance improvement in this case. It is also noted that the same number of satellites is used in GSNRx-hs-dr^{TM} as in GSNRx-hs^{TM}.

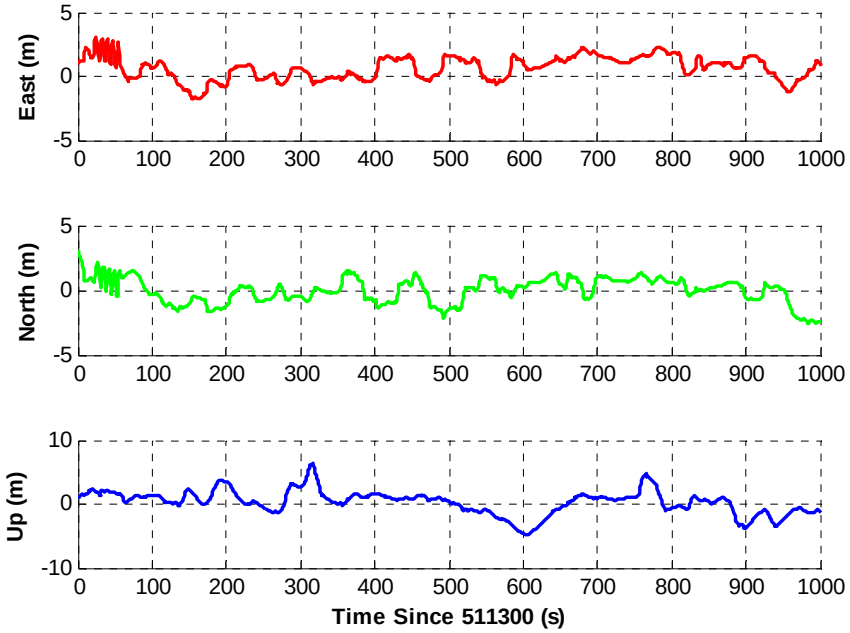

Figure 5.3: Position error plots for the GSNRx-hs-dr^{TM} in suburban and foliage test

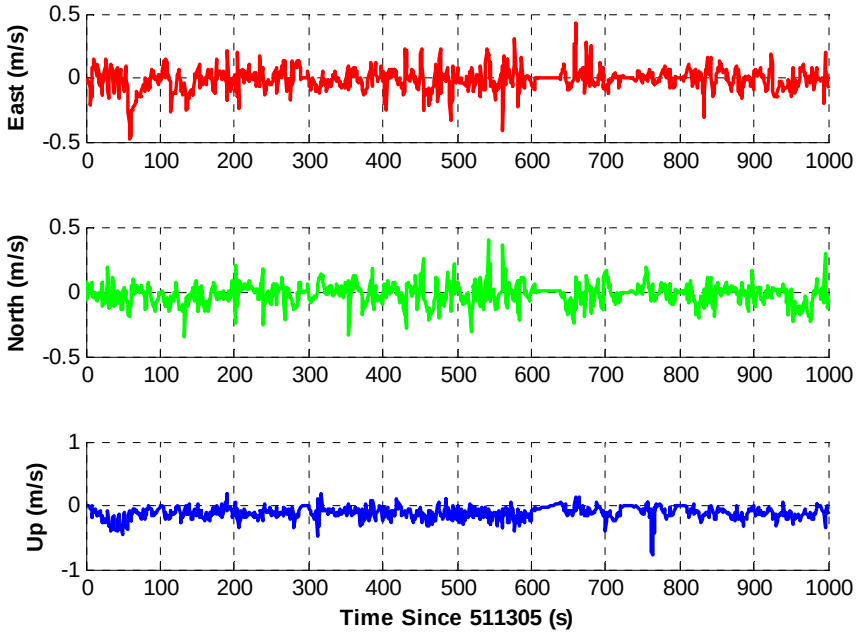

Figure 5.4: Velocity error plots for the GSNRx-hs-dr™ in suburban and foliage test

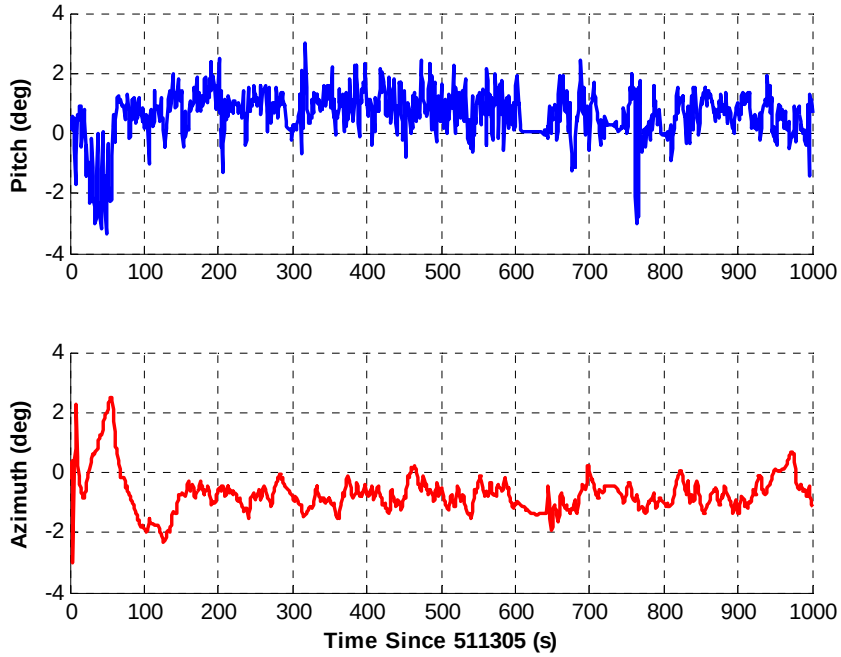

Figure 5.5: Attitude error plots for the GSNRx-hs-dr™ in suburban and foliage test

Table 5.1: Summarized RMS position and velocity errors with different sensor setup using GSNRx-hs-dr^{TM} in the suburban and foliage test

	Position (m)			Velocity (m/s)		
	East	North	Up	East	North	Up
RWSS	1.2	0.9	4.5	0.14	0.16	0.17
RWSS/YRS	1.2	0.9	2.0	0.10	0.09	0.14
RWSS/1A1G	1.2	0.9	1.6	0.10	0.08	0.12
WSS/1A1G	1.1	0.9	1.5	0.09	0.09	0.12
WSS/2A1G	1.0	0.7	1.5	0.08	0.09	0.11

Table 5.2: Summarized RMS attitudes errors with different sensors using GSNRx-hs-dr^{TM} in the suburban and foliage test

	Pitch (deg)	Roll (deg)	Azimuth (deg)
RWSS	1.71	N/A	2.64
RWSS/YRS	1.71	N/A	0.97
RWSS/1A1G	0.93	N/A	0.97
WSS/1A1G	0.93	N/A	0.97
WSS/2A1G	0.89	0.89	0.95

In order to analyze the navigation performance as the function of the search space for GSNRx-hs-dr^{TM}, the post-processing results using different search spaces were applied. In this case, the RWSS/1A1G sensor setup is used. Similar as the GPS only case, to begin with the analysis, the navigation performance using different frequency uncertainties is evaluated. Table 5.3 summarizes the RMS position and velocity errors as a function of the various frequency search spaces in the suburban and foliage scenario. As shown in this table, the GSNRx-hs-dr^{TM} with a 2 m/s frequency uncertainty offers the best position and

velocity accuracy. With an increase of the frequency search space, the navigation performance drops. Even though this performance degradation is minimal; it suggests that large frequency uncertainty increases the possibility of utilizing the erroneous correlation peaks (due to multipath or fading) for the final navigation solution. Therefore, given the reliable navigation solution from the DR algorithm in the suburban and foliage scenario and the vector based feedback mechanism used in the GSNRx-dr-hs^{TM}, the small frequency search space is desired in this case.

Table 5.3: Summarized RMS position and velocity errors as a function of frequency search uncertainties in the suburban and foliage test

	Position (m)			Velocity (m/s)		
	East	North	Up	East	North	Up
2 m/s	1.2	0.9	1.6	0.10	0.08	0.12
4 m/s	1.2	1.0	1.6	0.10	0.09	0.12
6 m/s	1.2	1.1	1.6	0.10	0.09	0.13
8 m/s	1.3	1.2	1.7	0.10	0.10	0.14

Similar analysis strategy as in the GPS only can be applied for the navigation performance as a function of the range uncertainties. Similar conclusions can be drawn as for the frequency uncertainty analysis, namely that the increased range uncertainty decreases the position and velocity accuracy, especially the position accuracy. Therefore, a 150 m range uncertainty is sufficiently large in this test scenario to provide a reliable navigation solution.

Table 5.4: Summarized RMS position and velocity errors as a function of range search uncertainties in the suburban and foliage test

	Position (m)			Velocity (m/s)		
	East	North	Up	East	North	Up
150 m	1.2	0.9	1.6	0.10	0.08	0.12
300 m	1.4	1.1	2.2	0.11	0.10	0.14
450 m	1.5	1.2	2.8	0.12	0.13	0.15

Finally, the navigation performance as a function of coherent integration time is presented. Three sets of coherent integration times namely 20 ms, 50 ms and 100 ms are used for the analysis. The 150 m and 8 m/s range and frequency uncertainties were applied in this case. Table 5.5 lists the positioning errors as the function of coherent integration time. As shown in this table, the higher the coherent integration time, the better navigation performance.

Table 5.5: Summarized RMS position and velocity errors as a function of coherent integration time in the suburban and foliage test

	Position (m)			Velocity (m/s)		
	East	North	Up	East	North	Up
20 ms	3.5	4.2	2.5	0.10	0.10	0.17
50 ms	2.0	2.2	1.9	0.10	0.10	0.15
100 ms	1.3	1.2	1.7	0.10	0.10	0.14

In summary, increasing the search space in the suburban and foliage environment generally decreases the positioning accuracy. This conclusion is similar to that of the GPS only case.

However, when vehicle sensors are integrated, the performance degradation resulting from the increased search space is relatively less as compared to the GPS only case.

Finally, the results from GSNRx-eb-dr ™ are presented for comparison purposes. A 20 ms coherent integration time is used in GSNRx-eb-dr ™ with an EKF based tracking strategy. The sensor setup used here is the RWSS/1A1G. The RMS position, velocity and attitude errors from GSNRx-eb-dr™ are summarized in Table 5.6. This solution provides slightly better performance as compared to that from GSNRx-hs-dr™ with a 20 ms coherent integration time. This is expected since GPS measurements from the EKF tracking are less noisy than those from the block estimator as long as the EKF tracking loop can maintain lock on the signals.

Table 5.6: Summarized RMS position and velocity errors as a function of range search uncertainties in the suburban and foliage test

Position (m)			Velocity (m/s)			Attitude (deg)	
East	North	Up	East	North	Up	Pitch	Azimuth
1.8	1.4	4.1	0.09	0.09	0.18	0.81	1.13

Compared with the results from GSNRx-hs-dr™ with a 100 ms coherent integration time, GSNRx-eb-dr™ provides a similar positioning accuracy. It suggested that in foliage areas, the EKF based ultra-tight GPS/DR integration with lesser correlators (eg. early, prompt and late correlators) can provide sufficient sensitivity and positioning accuracy. It can reduce the computation load thus decreasing the power consumption, which is important for portable vehicle/pedestrian navigators.

5.2.1.2 Tracking Domain Performance Analysis

Having discussed the performance of the ultra-tight receivers in the position domain, a similar tracking performance analysis as that of Section 2.4.1.5 is presented here. The estimated C/N_0 for PRN 17 with a high elevation angle (65 deg) is considered first. Figure 5.6 shows the estimated C/N_0 from the automotive grade HSGPS receiver, GSNRx-hs™, GSNRx-hs-dr™ and GSNRx-eb-dr™. The results from the automotive grade GPS receiver and GSNRx-hs™ are used for comparison purpose. Overall, the estimated C/N_0 values from these receivers are similar. It can be more clearly shown in Figure 5.7. The automotive grade GPS receiver applies highly filtered C/N_0 values and thus shows much less variations of C/N_0 compared to the others. The ultra-tight block processing receiver GSNRx-hs-dr™ provides slightly higher C/N_0 estimates compared to the conventional ultra-tight receiver GSNRx-eb-dr™. This may be due to different C/N_0 estimation algorithms being used by the different receivers, as mentioned in Section 2.4.1.5. It is also note that GSNRx-hs-dr™ and GSNRx-hs™ have exactly the same C/N_0 estimates in this case. Furthermore, GSNRx-hs-dr™ provides similar estimated Doppler accuracy as that of GSNRx-hs as shown in Figure 5.8. It indicates that ultra-tight integration with vehicle sensors does not provide noticeable tracking performance improvement for the high elevation satellites in this test environment.

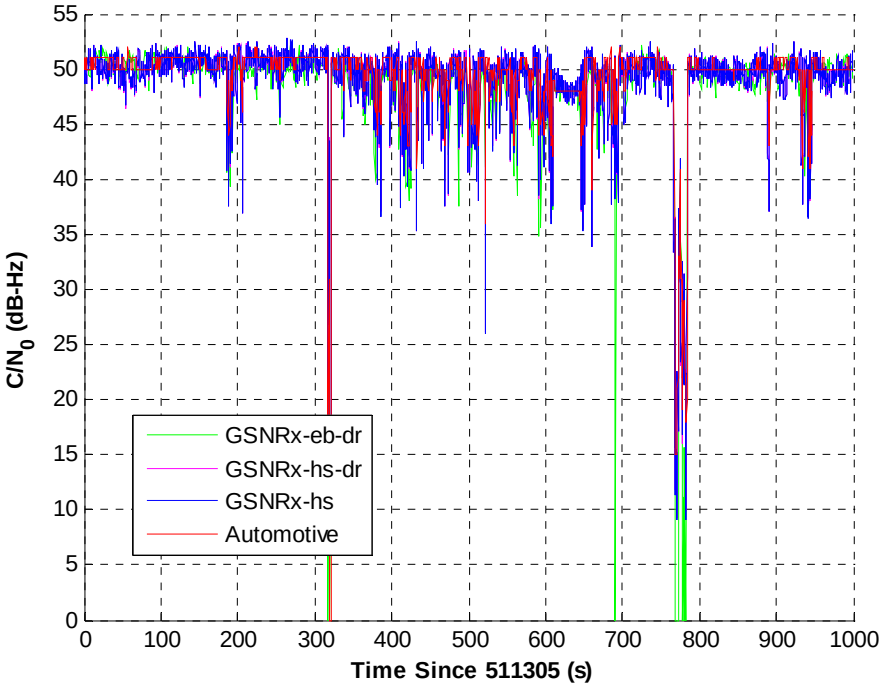

Figure 5.6: C/N_0 plots of PRN 17 in the suburban and foliage test

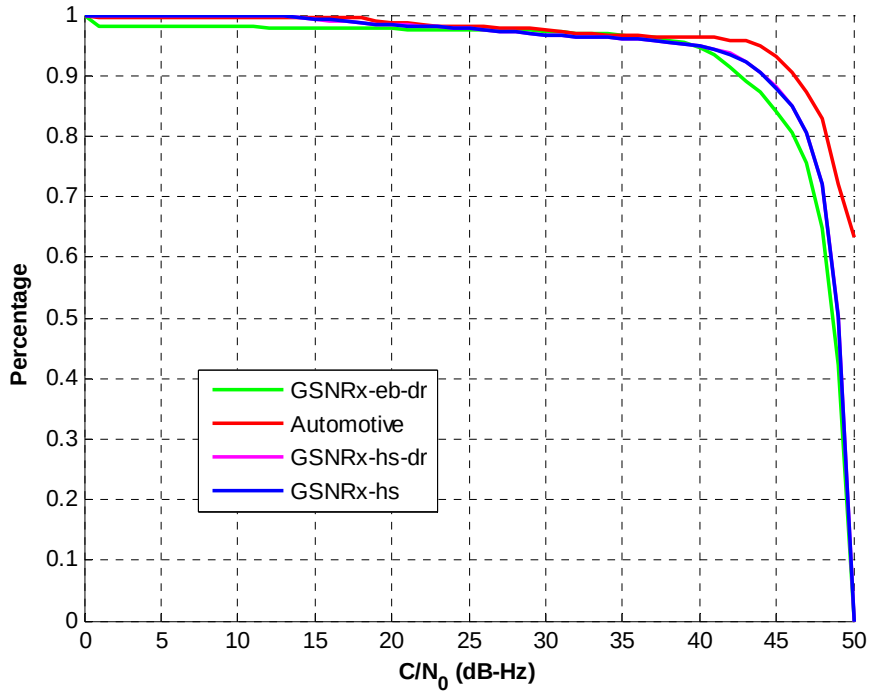

Figure 5.7: Cumulative C/N_0 plots of PRN 17 in the suburban and foliage test

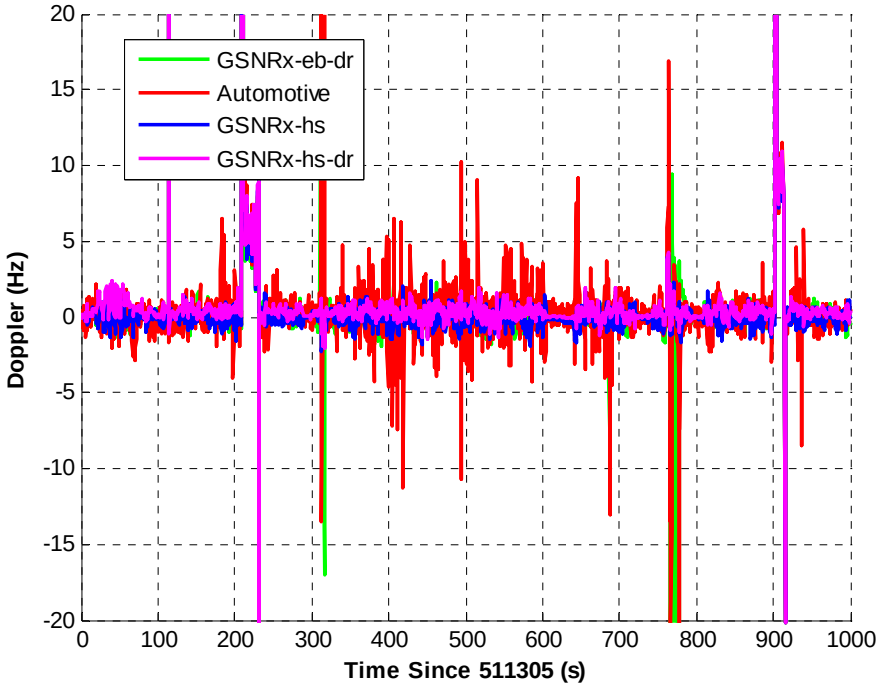

Figure 5.8: Doppler error of PRN 17 in the foliage test

Table 2.7: Summarized RMS Doppler errors with ultra-tight solutions in the suburban and foliage test

	PRN 17 (Hz)	PRN 32 (Hz)
Automotive	1.7	3.2
GSNRx-eb-dr™	5.0	26.3
GSNRx-hs™	1.2	1.0
GSNRx-hs-dr™	1.2	0.8

Next, the C/N_0 plots for the low elevation satellite PRN 32 (8 deg) are used for the analysis. In this case, GSNRx-eb-dr™ has poor C/N_0 estimates compared with other receivers as shown in Figure 5.9and Figure 5.10 and less accurate Doppler estimates as shown in Figure 5.11, which indicates a poor tracking performance of the EKF based ultra-tight receiver for the low elevation satellite with weaker signal strength. Similar as for the high

elevation angle case, GSNRx-hs-dr™ provides only a minimal performance improvement over GSNRx-hs™ in terms of the estimated C/N_0 and Doppler.

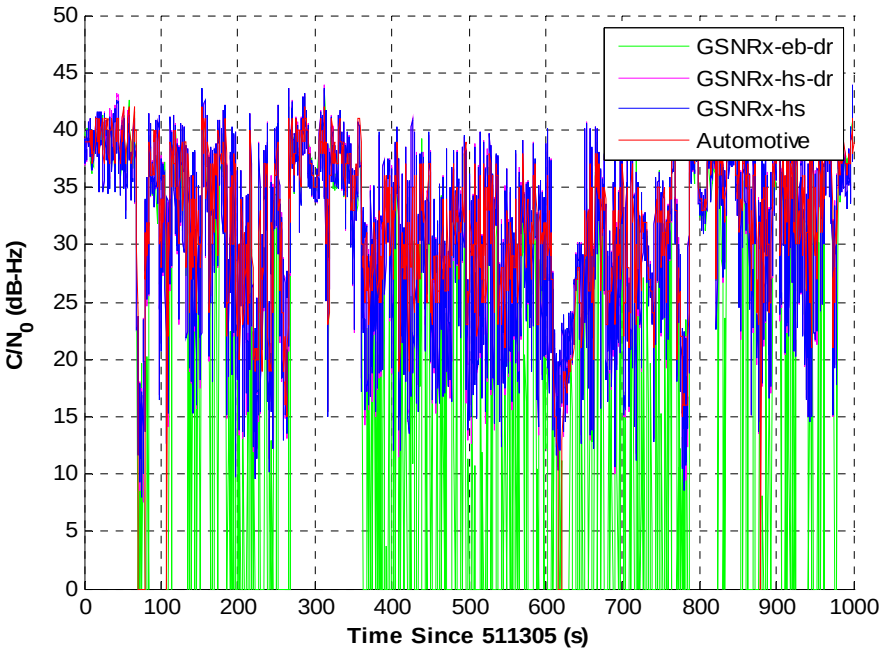

Figure 5.9: C/N_0 plots of PRN 32 in the suburban and foliage test

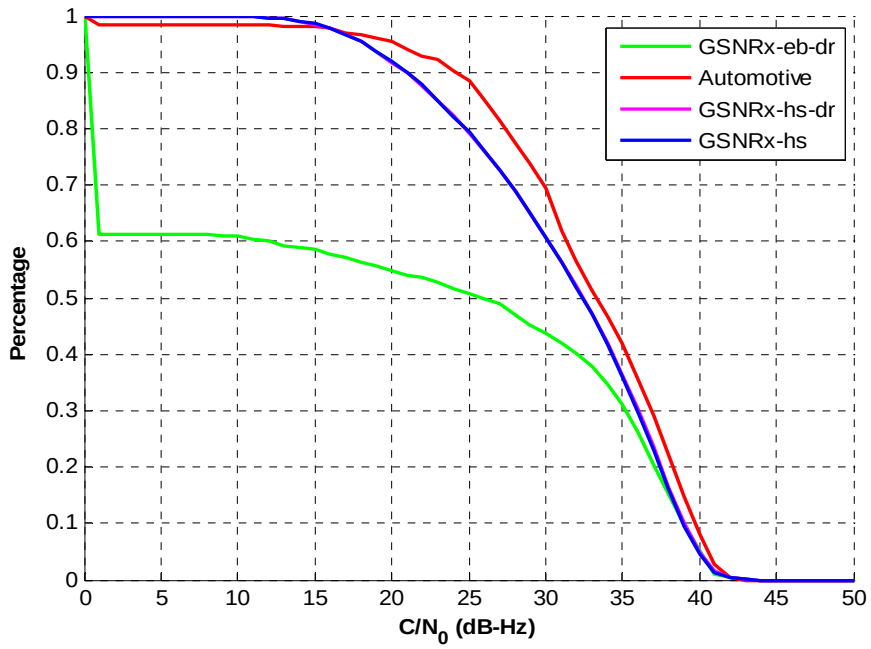

Figure 5.10: Cumulative C/N_0 plots of PRN 32 in the suburban and foliage test

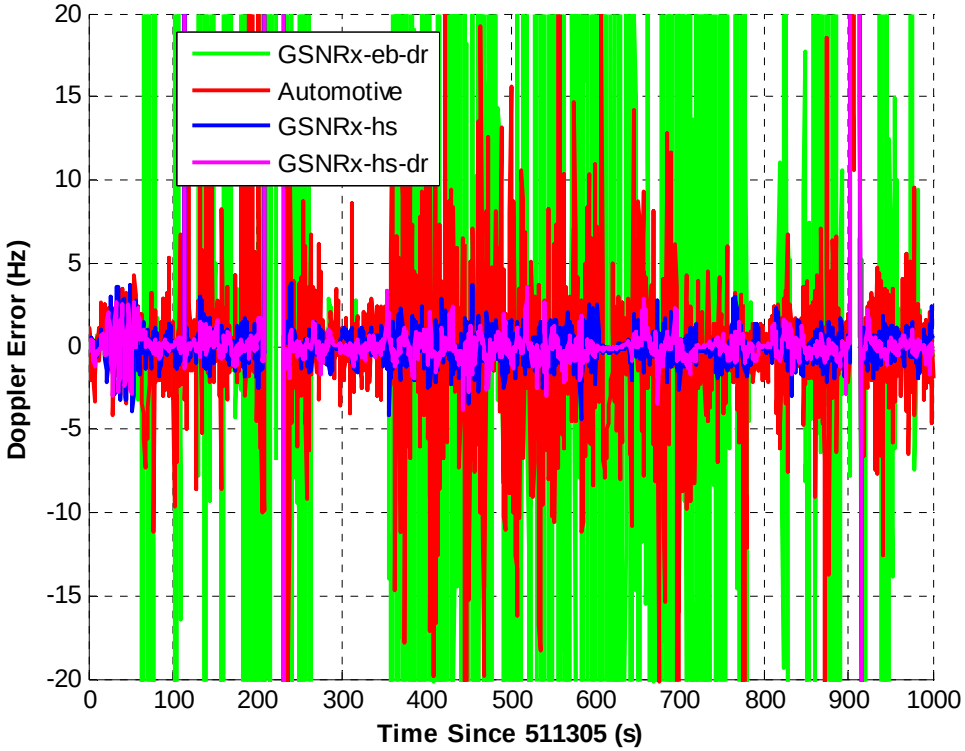

Figure 5.11: Doppler error of PRN 32 in the foliage test

According to the results from the foliage test, the high sensitivity block processing based ultra-tight GPS receiver has similar positioning performance as that from an EKF based ultra-tight receiver. However, with the increased coherent integration time, high sensitivity block processing based ultra-tight GPS receiver did provide improved tracking sensitivity compared with the EKF based ultra-tight receiver. Furthermore, the ultra-tight integration of vehicle sensors does not provide noticeable performance improvement in either positioning or tracking domain.

5.2.2 Urban Canyon Scenario

Having discussed the results from the foliage test, the performance analysis is conducted for the urban canyon test in this section. Similar to the suburban and foliage test, the results are analyzed in both positioning domain and tracking domain..

5.2.2.1 Position Domain Performance Analysis

Firstly, the performance of the ultra-tight solutions is analyzed in the position domain. The position and velocity accuracies are used to assess the positioning performance of the various receivers.

Figure 5.12, Figure 5.13 and Figure 5.14 illustrate the position, velocity and attitude errors of GSNRx-hs-dr^{TM} with the RWSS/1A1G sensor setup. Compared to the tight integration of GSNRx-hs^{TM} and RWSS/1A1G, the navigation accuracy from ultra-tight integration is slightly improved in this test environment. The RWSS, RWSS/YRS, RWSS/1A1G, WSS/SAS/1A1G and WSS/SAS/2A1G sensor setups are used for the performance analysis. Table 5.7 and Table 5.8 summarize the RMS positioning error and attitude errors using GSNRx-hs-dr^{TM} with different sensor setups. Except for the RWSS sensor setup, all the other sensor setup meets the 5 m positioning accuracy requirement. However, taken cost and reliability into the consideration of system design, RWSS/1A1G would be an appropriate candidate. It is also noted that GSNRx-hs-dr^{TM} has more satellites used in the navigation solution as compared to the GSNRx-hs^{TM} case shown in Figure 5.15.

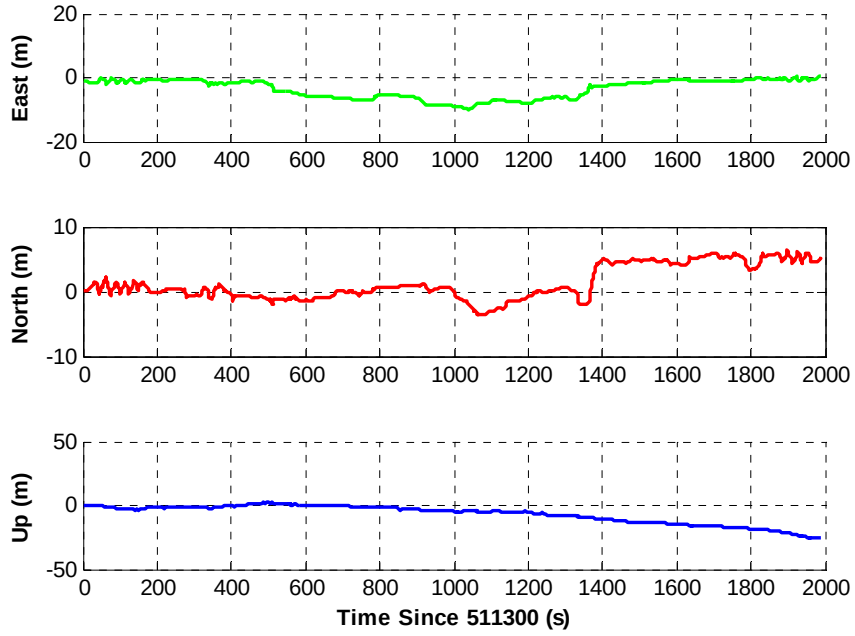

Figure 5.12: Position error plots for the GSNRx-hs-dr™ in urban canyon test

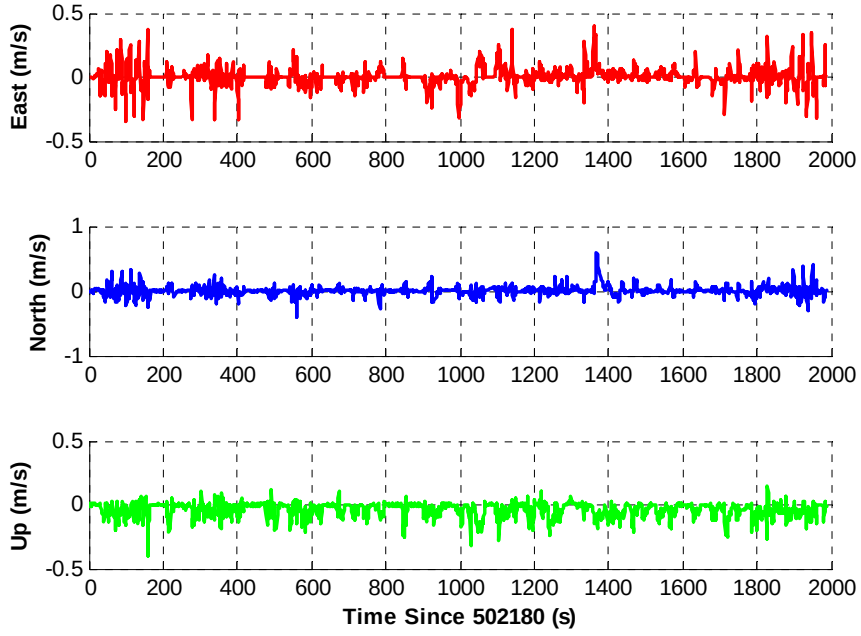

Figure 5.13: Velocity error plots for the GSNRx-hs-dr™ in urban canyon test

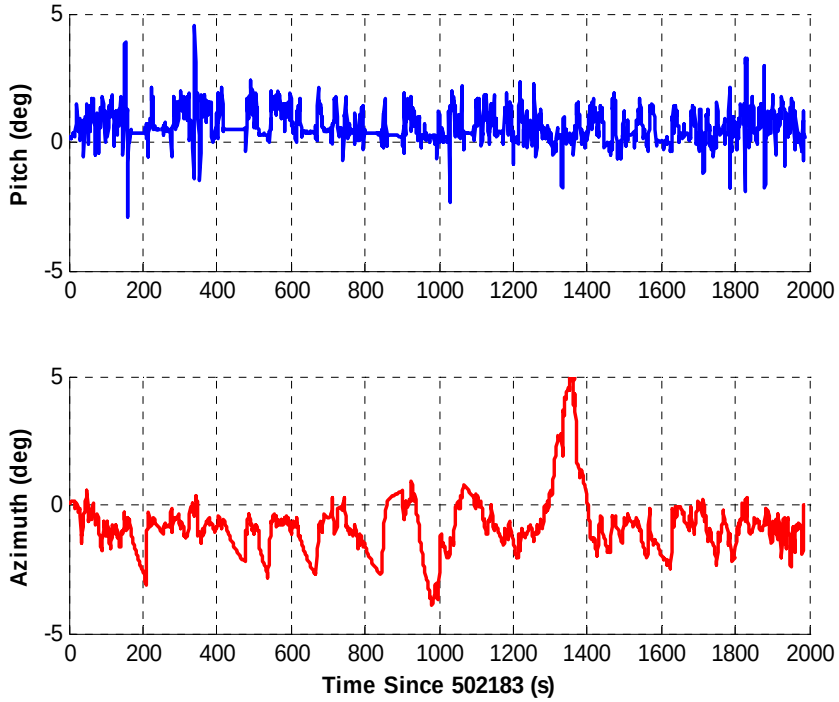

Figure 5.14: Attitude error plots for the GSNRx-hs-dr™ in urban canyon test

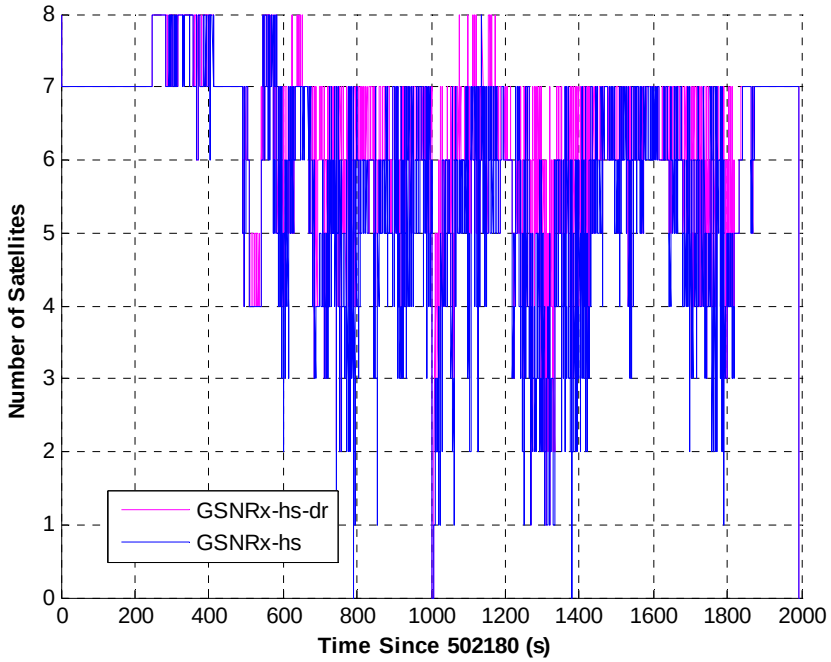

Figure 5.15: Number of satellites used in the navigation solution in urban canyon test

Table 5.8: Summarized RMS position and velocity errors with different sensor setups using GSNRx-hs-dr™ in the suburban and foliage test

	Position (m)			Velocity (m/s)		
	East	North	Up	East	North	Up
RWSS	5.1	3.9	9.1	0.07	0.08	0.07
RWSS/YRS	4.3	3.9	9.1	0.07	0.08	0.07
RWSS/1A1G	4.7	3.1	9.6	0.07	0.07	0.07
WSS/1A1G	4.6	2.9	9.6	0.07	0.07	0.07
WSS/2A1G	4.5	3.1	9.0	0.07	0.07	0.07

Table 5.9: Summarized RMS attitude errors with different sensors using GSNRx-hs-dr™ in the suburban and foliage test

	Pitch (deg)	Roll (deg)	Azimuth (deg)
RWSS	1.71	N/A	2.01
RWSS/YRS	1.71	N/A	1.61
RWSS/1A1G	0.89	N/A	1.41
WSS/1A1G	0.88	N/A	1.40
WSS/2A1G	0.89	0.89	0.95

In order to analyze the navigation performance as the function of the search space for GSNRx-hs-dr™, the post-processing using different search spaces was applied. In this case the RWSS/1A1G sensor setup is used. Similar to the GPS only case, to begin with the analysis, the navigation performance using different frequency uncertainties is evaluated. Table 5.9 summarizes the RMS position and velocity errors as a function of the various frequency search spaces in the suburban and foliage scenario. As listed in this table, the

GSNRx-hs-dr^{TM} using a 4 m/s frequency uncertainty offers the best position and velocity accuracies. When the either increasing or decreasing the frequency search space, the navigation performance drops. It suggests that a large frequency uncertainty increases the possibility of utilizing erroneous correlation peaks (due to multipath or fading) for the final navigation solution. But the search space should be sufficient large to improve the tolerance of the navigation error in degraded signal environments. Therefore, a 4 m/s frequency search space is used.

Table 5.10: Summarized RMS position and velocity errors as a function of frequency search uncertainties in the suburban and foliage test

	Position (m)			Velocity (m/s)		
	East	North	Up	East	North	Up
2 m/s	5.1	3.9	9.6	0.07	0.07	0.08
4 m/s	4.6	2.9	9.6	0.07	0.07	0.07
6 m/s	5.2	3.1	9.6	0.08	0.08	0.09
8 m/s	5.6	4.2	9.7	0.09	0.09	0.09

A similar analysis strategy as in the GPS only case can be applied for the navigation performance as a function of the range uncertainty in the urban canyon case. Similar conclusions can be drawn as for the GPS only case, namely that the appropriate range uncertainty is 300 m in this case. Furthermore, given the low signal strength as in the urban canyon environment case, the longer integration time is preferable. A 100 ms coherent integration time provides the best performance over 50 ms and 20 ms. The results are not listed herein.

It is noted that unlike in the suburban and foliage case, increasing the search space yields worse positioning errors, suggesting that an optimum search space neither too large nor too small should be carefully selected in the urban canyon environment. The size of the search space depends on both navigation solution accuracy and multipath signal strength (Xie & Petovello 2011).

Finally, the results from GSNRx-eb-dr^{TM} are presented for comparison purposes. A 20 ms coherent integration time is used in GSNRx-eb-dr ^{TM} with an EKF based tracking strategy. The sensor setup used here is the RWSS/1A1G. The RMS position, velocity and attitude errors from GSNRx-eb-dr^{TM} are summarized in Table 5.10. As listed in this table, GSNRx-eb-dr ^{TM} accuacy is still within 5 m RMS for the urban canyon test but with a slightly larger velocity error compared to use of GSNRx-hs-dr^{TM}.

Table 5.11: Summarized RMS position and velocity errors from GSNRx-eb-dr^{TM} in the urban canyon test

Position (m)			Velocity (m/s)			Attitude (deg)	
East	North	Up	East	North	Up	Pitch	Azimuth
3.9	2.8	3.4	0.08	0.11	0.12	0.54	2.27

5.2.2.2 Tracking Domain Performance Analysis

Having discussed the performance of the ultra-tight receivers in the position domain, a similar tracking performance analysis as that in Section 5.2.1.2 is presented here for the urban canyon test. The estimated C/N_0 for the PRN 28 with a high elevation angle (85 deg) is considered first. Figure 5.16 shows the estimated C/N_0 for the automotive grade GPS

receiver, GSNRx-hs™, GSNRx-hs-dr™ and GSNRx-eb-dr™. The results for the automotive grade GPS receiver and GSNRx-hs™ are used for comparison purpose. Overall, the estimated C/N_0 values from these receivers except the GSNRx-eb-dr™ are similar. It can be more clearly seen in Figure 5.17. The results from the GSNRx-eb-dr™ are slightly poorer which indicates limited tracking sensitivity in the urban canyon environment. It is also noted that the GSNRx-hs-dr™ and GSNRx-hs™ receivers have exactly the same C/N_0 estimation performance in this case.

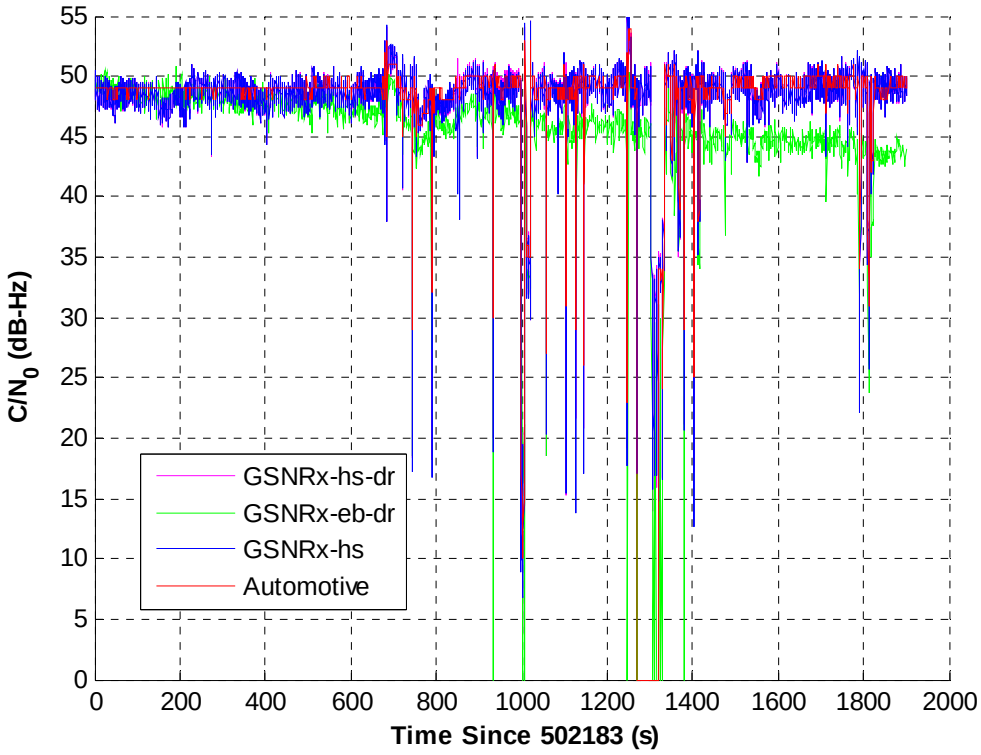

Figure 5.16: C/N_0 plots of PRN 28 in the urban canyon test

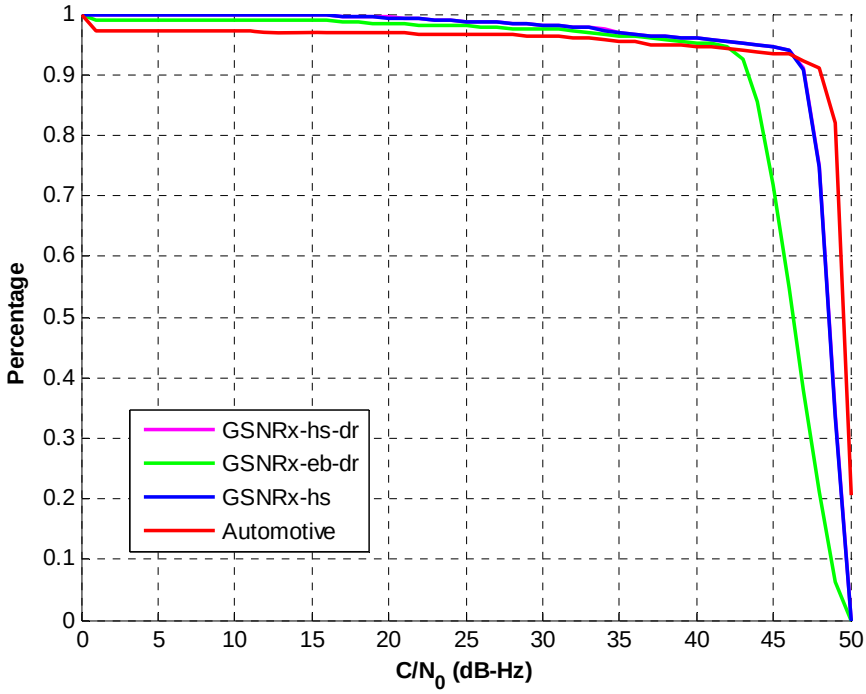

Figure 5.17: Cumulative C/N_0 plots of PRN 28 in the urban canyon test

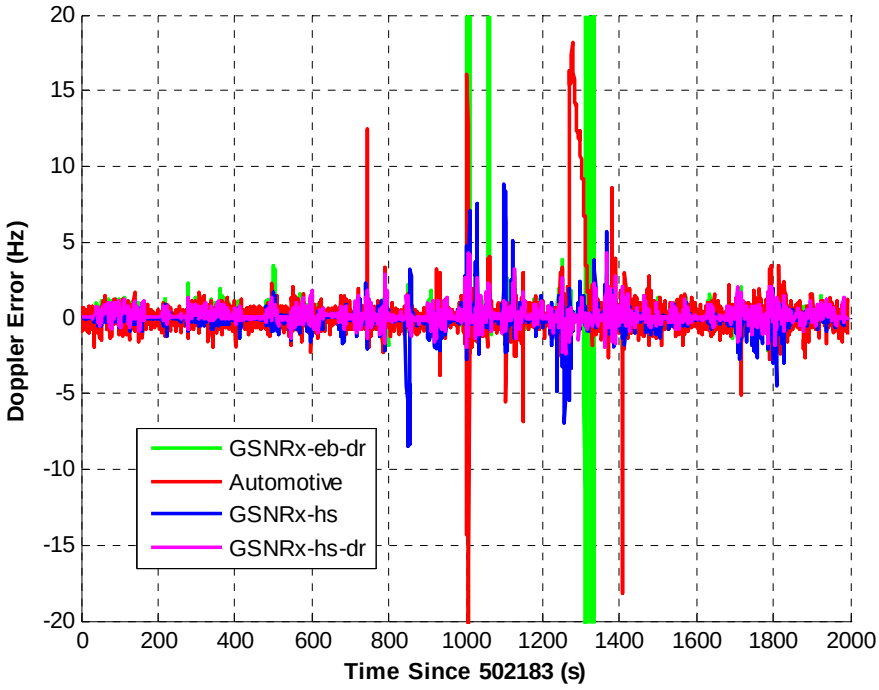

Figure 5.18: Doppler error of PRN 28 in the urban canyon test

Figure 5.18 shows the Doppler error for the four receivers. GSNRx-hs-dr™ provides the best performance and outperforms GSNRx-hs™ by 0.4 Hz in an RMS sense. It is also noted that GSNRx-eb-dr™ have a similar Doppler accuracy as that of the automotive HSGPS receiver except for those large spikes of errors when losing lock. The results indicate that ultra-tight integration with vehicle sensors does not provide noticeably improved C/N_0 estimates but slightly improved Doppler estimates for high elevation angle satellite.

Next, the C/N_0 plots for the lower elevation satellite PRN 24 (28 deg) are used for the analysis. In this case, GSNRx-eb-dr™ has noticeably poor C/N_0 and Doppler estimates as compared to the other receivers, as shown in Figure 5.19, Figure 5.20 and Figure 5.21, which indicates a poor tracking performance of the EKF based ultra-tight receiver for a low elevation satellite with a weaker signal strength. Similar to the high elevation angle case, GSNRx-hs-dr™ provides a minimal C/N_0 performance improvement over GSNRx-hs™. However, the Doppler accuracy is improved by 2.1 Hz for GSNRx-hs-dr™ as compared to GSNRx-hs™ in a RMS sense.

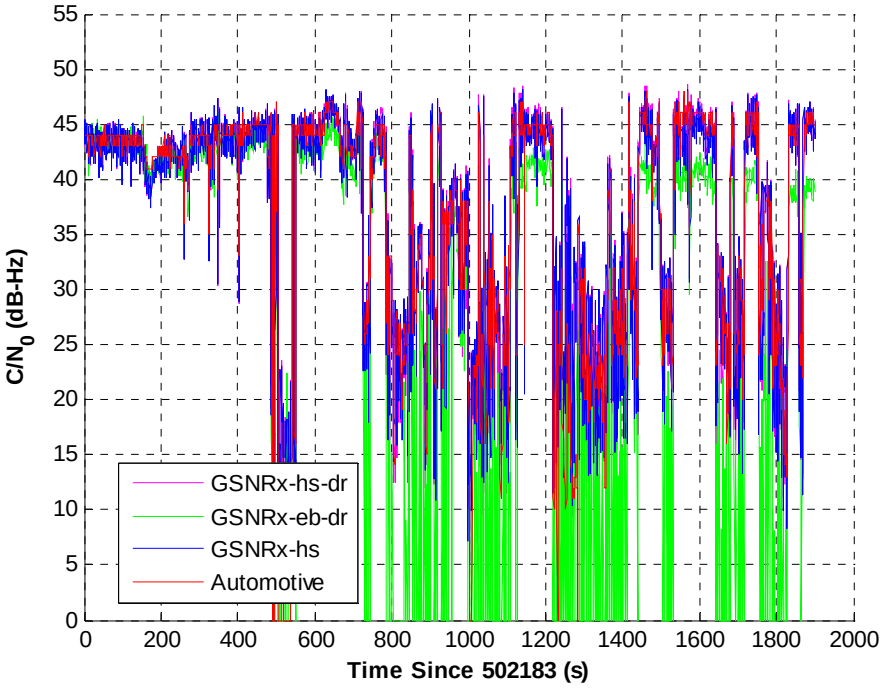

Figure 5.19: C/N_0 plots of PRN 24 in the suburban and urban canyon test

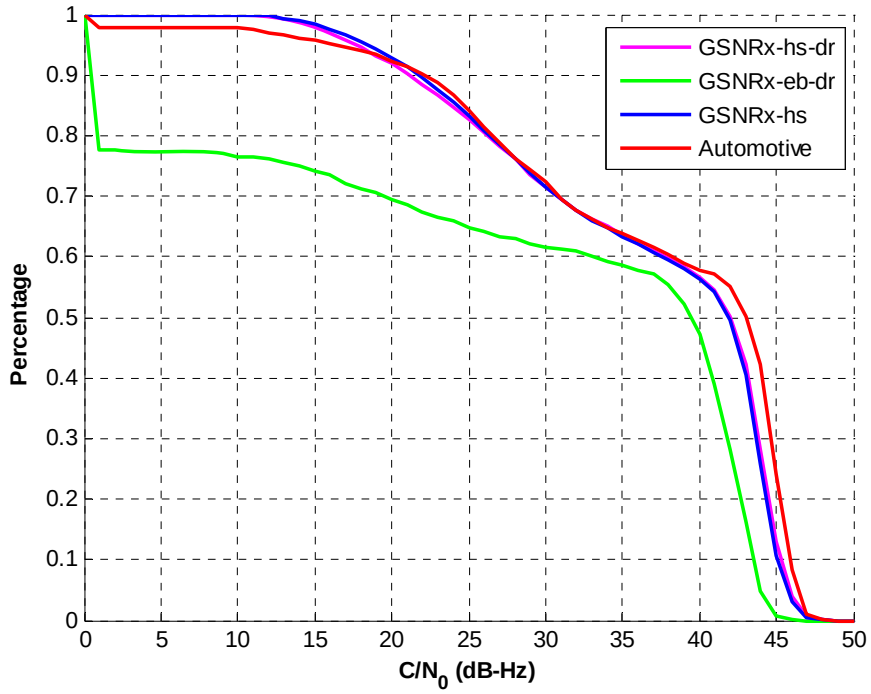

Figure 5.20: Cumulative C/N_0 plots of PRN 24 in the urban canyon test

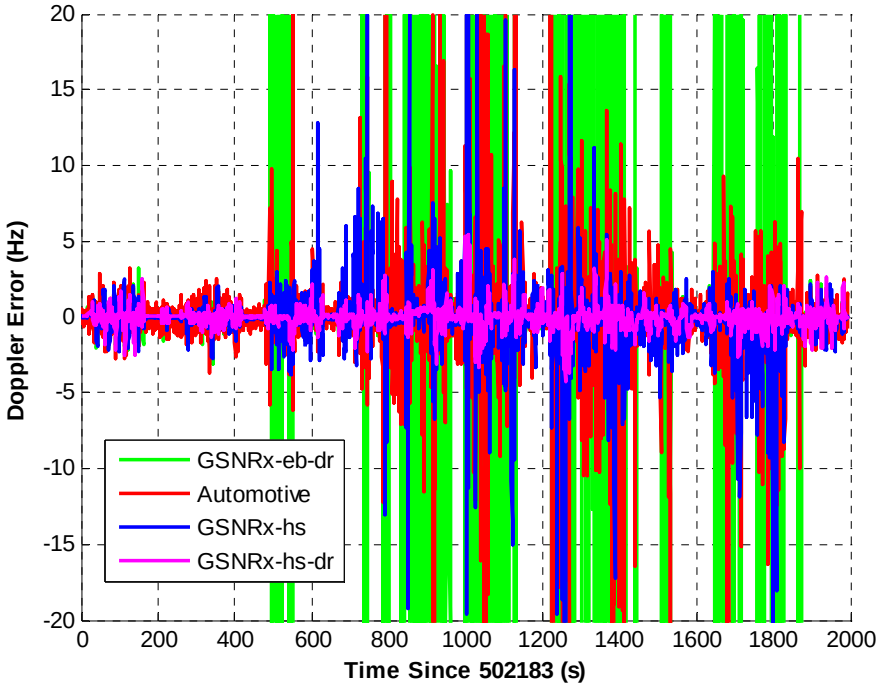

Figure 5.21: Doppler error of PRN 24 in the urban canyon test

Table 2.12: Summarized RMS Doppler errors with ultra-tight solutions in the urban canyon test

	PRN 28(Hz)	PRN 24 (Hz)
Automotive	2.3	5.9
GSNRx-eb-dr™	16.4	89.5
GSNRx-hs™	0.9	2.9
GSNRx-hs-dr™	0.5	0.8

According to the results from the urban canyon test, the high sensitivity block processing based ultra-tight GPS receiver has similar positioning performance as that of an EKF based ultra-tight receiver. However, with increased coherent integration time, a high sensitivity block processing based ultra-tight GPS receiver did provide improved tracking sensitivity

compared to the EKF based ultra-tight receiver with both improved C/N_0 and Doppler estimates. Furthermore, the ultra-tight integration of vehicle sensors provides slightly improved Doppler estimates as compared to the GSNRx-hs^{TM} in the tracking domain.

CHAPTER SIX: CONCLUSIONS AND FUTURE WORK

This chapter provides the conclusions of the research work presented in this thesis, which focused on efficiently taking advantage of high sensitivity block processing for improved GNSS signal processing and development of DR algorithms with vehicle sensors for improved navigation accuracy. Possible future directions that would enhance the proposed methodologies are also presented in this section.

6.1 Conclusions

The main goal of this research work was the development of a high sensitivity ultra-tight GPS receiver for vehicular applications. Towards this, the thesis research work was conducted in different stages with predefined objectives according to Section 1.3. The following sections provide the related research activities and their outcomes.

6.1.1 High Sensitivity Block Processing GPS Receiver

a) The developed high sensitivity algorithm performs in a manner comparable to that of a commercial high-sensitivity receiver when operating in suburban areas and under foliage. A comparison of the developed receiver with a "standard sensitivity" version, which can only provide reliable C/N_0 estimates above 34 dB-Hz. GSNRx-hs^{TM} shows considerable improvements by reliably providing C/N_0 estimates as low as 16 dB-Hz.

b) Compared to the automotive grade HSGPS, the proposed GSNRx-hs^{TM} shows improved Doppler estimates by 1-2 Hz in the RMS sense. It is mainly due to the

vector tracking strategy used in GSNRx-hs™ with compensated user motion dynamics.

c) For the suburban and foliage scenario tested, increasing the correlator search space in either the code phase (time) or Doppler (frequency) dimensions yielded worse results as compared with the initial 150 m and 2 m/s range.

d) The effect of integration time was also investigated. In this case, longer integrations (up to 100 ms) were found to produce better position and velocity solutions in the suburban and foliage scenario.

e) The optimum correlator search space in the urban canyon environment is 4 m/s and 300 m for the frequency and code respectively. Either increasing or decreasing the search space would degrade the system performance. This results from the high possibility of including multipath peaks in the navigation solution with extended search space.

6.1.2 Improved DR-based Vehicle Sensor Integration

a) The proposed DR-based algorithms outperform the INS mechanization based algorithms, especially when the quality of GPS signals is degraded under the dense foliage area. The INS mechanization based algorithms rely on the GPS measurements to frequently correct accelerometer biases for the system velocity estimates. However, the WSS derived velocity requires less frequent updates from GPS to maintain a certain accuracy. Therefore the proposed DR-based algorithms provide higher reliability and improved navigation accuracy. The position and velocity accuracies improvement is up to 50% and 60% respectively depending on the quality of GPS measurements. The

lower quality of GPS measurements, the more noticeable improvement is observed. Thus the DR based integration algorithms are used in the navigation system for land vehicles in the thesis.

b) In terms of the sensor configurations, the RWSS/YRS normally provided sufficient positioning accuracy. However, the pitch and roll information cannot be obtained using this sensor setup. When introducing the longitudinal accelerometer, the pitch can be estimated but without noticeable improvement of positioning accuracy. Similarly, the inclusion of the lateral accelerometer can provide roll information for the DR-based algorithm but with the minimal navigation performance improvement. Finally, the full sensor setup, namely WSS/2A1G provides similar performance with WSS/1A1G, and RWSS/1A1G sensor setup when GPS updates are available however it does show up to 30% position accuracy improvement over RWSS/YRS sensor setup. For velocity estimates, the improvement is still quite minimal. Furthermore, the full sensor setup improves the reliability of the system with the redundant sensor configuration.

c) Under degraded signal environments such as deep foliage areas and urban canyons, the tightly coupled DR solutions outperform the loose coupled solution by up to 70% in the position and 30% in the velocity. This is mainly due to the improved GPS measurements independency and better blunder detection capability.

d) Field test results indicate that the free running DR system can provide up to 2.4% accuracy with the WSS/2A1G sensor setup, which outperforms Somieski (2010)'s results by 3.8%.

6.1.3 DR-based In-motion Alignment Algorithm

a) The proposed DR-based in-motion alignment algorithm for MEMS reduced IMU demonstrates fast convergence speed when GPS and wheel speed sensor measurements are available without having any initial attitude information. Field test results show that the proposed in-motion alignment algorithms took only 15 seconds to obtain the azimuth estimates within a 5 deg accuracy regardless of the initial azimuth error.

b) Compared with the pseudo-signal based in-motion alignment algorithm using a large heading uncertainty model, the proposed DR-based in-motion alignment algorithms provided a slightly improved convergence speed with smaller azimuth variation during the alignment process.

6.1.4 Ultra-tightly Coupled HSGPS/DR-based Vehicle Sensor Integration

a) Compared with the conventional ultra-tight GPS/DR-based receiver, the use of a high sensitivity block processing technique did improve the tracking capability as indicated by the improved C/N_0 and Doppler estimates when signal strength is below 20 dB-Hz in the urban canyon environment. For the suburban and foliage environment, ultra-tight integration of vehicle sensors (GSNRx-hs-dr^{TM}) does not provide a noticeable Doppler estimate improvement (0.1 Hz) for both the high and low elevation satellites as compared with GSNRx-hs^{TM}. However, for the urban canyon environment, the use of ultra-tight integration improves the Doppler estimates by up to 2.1 Hz (RMS) compared to GSNRx-hs^{TM}.

b) Compared to the conventional ultra-tight receiver GSNRx-eb-dr^{TM}, the ultra-tight HSGPS/DR improved both the C/N_0 and Doppler estimates for the foliage and urban

canyon test. It indicates that the use of high sensitivity block processing tracking strategy improves the tracking performance of an ultra-tightly coupled GPS/vehicle sensor integrated receiver.

c) In terms of positioning accuracy, the ultra-tight HSGPS/DR provided minimal improvement over the tight GPS/DR and conventional ultra-tight/DR solutions. This is mainly due to the inclusion of NLOS signals into the navigation solution for the ultra-tight HSGPS/DR solution.

d) A 5 m positioning accuracy is achieved by using the proposed ultra-tightly coupled HSGPS with vehicle sensors under all the test environments.

6.2 Future Work

Based on the analysis and experimental results obtained in this research work, the following recommendations can be made:

a) Further investigation of road conditions on the performance of the DR algorithm should be conducted. The current DR results are from dry road conditions. With wet or icy road conditions, the parameters used for the wheel scale factor estimations and the criteria to determine the sideslip should be reevaluated.

b) Properly characterizing multipath including assessing the number of received signal (including whether the desired signal is present) as well as the offsets in time and frequency of the non-desired signals (relative to the desired signal) can be used as prior information for the receiver to adaptively tune the relevant parameters, such as the size of the search space and (ideal) required integration time.

c) Data bits estimation algorithm can be applied to extend the coherent integration time without data bits aiding. Especially in the real time applications, consistently transmitting data bits is not feasible due to the latency and errors in the data link. Thus the data bit estimation algorithm can be used to form a standalone system for such situations.

d) Further algorithms for the quality control of the navigation solution can be applied to determine the optimum search space selection. It is beneficial not only improving the computation efficiency but also isolating the NLOS signals from the navigation solution calculations during the multi-path environment.

e) Further analysis of the selection of the coherent and noncoherent combinations can be applied. Given the oscillator quality, vehicle dynamics, signal strength and the navigation solution accuracy, the optimum coherent integration time and the number of noncoherent integrations can be determined. The adaptive selection of the coherent and noncoherent integration scheme would improve both the reliability and positioning accuracy of the receiver.

f) Although the research presented in the thesis is focused on the vehicular navigation applications, it can be further extended to the robotic, automatic agriculture applications.

g) Optimization of the HSGPS receiver can be applied to achieve the real-time capability. The current results presented in this thesis were from the post processing, however, the structure of the code is readily available for the real-time implementation. With the aiding of the more powerful processer or FPGA, a real-time ultra-tight HSGPS/DR receiver is highly possible.

REFERENCE

Alban, S., D. Akos, S. Rock (2003) "Performance Analysis and Architectures for INS-Aided GPS Tracking Loops," in *Proceedings of ION NTM 2003*, 22-24 January, Anaheim CA, pp.611-622, U.S. Institute of Navigation, Fairfax VA.

Abbott, A.S. and W.E. Lillo (2003) "Global Positioning Systems and Inertial Measuring Unit Ultratight Coupling Method," Patent, US 6,516,021 B1, United States, 22 pages.

Anderson, R. and D. M. Bevly (2004) "Estimation of Slip Angles Using a Model Based Estimator and GPS," *in Proceedings of the American Control Conference*. Boston, Massachusetts, pp. 2122-2127.

Babu, R. and J. Wang (2006) "Ultra-Tight Integration of Pseudolites With INS," in *Proceedings of IEEE/ION PLANS 2006*, 25-27 April, San Diego CA, pp.705-713.

Bevly, D. M. (2004), "Global Positioning System (GPS): A Low-Cost Velocity Sensor for Correcting Inertial Sensor Errors on Ground Vehicles," *Journal of Dynamic Systems, Measurement, and Control*, JUNE 2004, Vol. 126, DOI: 10.1115/1.1766027.

Bevly, D. M. and B. Parkinson, (2007) "Cascaded Kalman Filters for Accurate Estimation of Multiple Biases, Dead-Reckoning Navigation, and Full State Feedback Control of Ground Vehicles," *IEEE Transaction On Control Systems technology*, VOL. 15, NO. 2, MARCH 2007.

Bevly, D.M., J.C.Gerdes and C. Wilson (2002), "The Use of GPS Based Velocity Measurements for Measurements of Sideslip and Wheel Slip," *Vehicle System Dynamics*, Vol. 38, No.2, 2002, pp.127-147.

Bevly, D.M., R.Sheridan, and J.C.Gerdes (2001), "Integrating INS Sensors with GPS velocity Measurements for Continuous Estimation of Vehicle Sideslip and Tire Cornering Stiffness," *Proceedings of the American Control Conference 2001*, Arlington, VA, June 25-27, 2001, pp.25-30.

Bonnifait, P. B. Pascal, C. Paul and M. Dominique (2001) "Data Fusion of Four ABS Sensors and GPS for an Enhanced Localization of Car-like Vehicles", *in Proceedings of the 2001 IEEE International Conference on Robotics & Automation*, Seoul, Korea.

Borio, D., N. Sokolova and G. Lachapelle (2009) "Memory Discriminators for Non-Coherent Integration in GNSS Tracking Loops". ATTI dellstituto Italiano di Navigazione, No 189, July Issue, 80-100.

Borio, D. (2008) “A Statistical Theory for GNSS Signal Acquisition”, Doctoral Thesis, Dipartimento di Elettronica, Politecnico di Torino, Italy.

Brandit, A., J. F. Gardner (1998) “Constrained Navigation Algorithm for Strapdown Inertial Navigation Systems with Reduced Set of Sensors,” in *Proceedings of the American Control Conference1998,* June, Philadelphia PA, pp. 1848-1852.

Brown, A., D. Nguyen, Y. Lu, and C. Wang (2005) “Testing of Ultra-Tightly-Coupled GPS Operation Using a Precision GPS/Inertial Simulator,” in *Proceedings of ION GNSS 2005*, 13-16 Sept., Long Beach CA, pp. 439-447, U.S. Institute of Navigation, Fairfax VA.

Carlson C.R. (2003) *Estimate with applications for automobile dead reckoning and control*, Ph.D Thesis, Stanford University, USA.

Chiou, T. (2005) “GPS Receiver Performance Using Inertial-Aided Carrier Tracking Loop,” in *Proceedings of ION GNSS 2005,* 13-16 Sept, Long Beach CA, pp. 2895-2910, U.S. Institute of Navigation, Fairfax VA.

Daum, P., J. Beyer, T. Köhler (1994) “Aided Inertial land navigation System (ILANA) with a Minimum Set of Inertial Sensors,” in *Proceedings of IEEE-IEE Vehicle Navigation & Information Systems Conference*, Yokohama-VNIS’94, pp. 284-291.

Dissanayake, G., S. Sukkarieh, E. Nebot and H. DurrantWhyte (2001) “The aiding of a Low Cost Strapdown Inertial Measurement Unit using Vehicle Model Constraints for Land vehicle Applications,” *IEEE Transactions on Robotics and Automation*, vol.17, no. 5, pp. 731-747.

Farrell.A.Jay (2008) *Aided Navigation: GPS with high rate sensors*, McGraw-Hill Comapany, USA

Fuke, Y. and K. Eric (1996), “Dead Reckoning for a Lunar Rover om Uneven Terrain,” in *Proceedings of the 1996 IEEE International Conference on Robotics and Automation*, Minneapolis, Minnesota -April 1996.

Hong,H.S., J. G. Lee, and C. G. Park (2004), "Performance improvement of in-flight alignment for autonomous vehicle under large initial heading error," *IEE Proc.-Radar Sonar Navigation*, vol. 151, pp. 57-62,

Gao, J., (2007) “Development of a Precise GPS/INS/On-Board Vehicle Sensors Integrated Vehicular Positioning System,” PhD Thesis, Published as Report No. 20255, Department of Geomatics Engineering, The University of Calgary.

Godha, S.(2006) *Performance Evaluation of Low Cost MEMS-Based IMU Integrated With GPS for Land Vehicle Navigation Application*, M.Sc. thesis, Department of Geomatics Engineering, University of Calgary, Canada (Available at http://www.geomatics.ucalgary.ca/research/publications/GradTheses.html)

Gebre-Egziabher, D., and A. Ravzi, P. Enge, J. Gautier, S. Pullen, B. Pervan, and A. Akos (2005) "Sensitivity and Performance Analysis of Doppler-Aided GPS Carrier-Tracking Loops," *Navigation*, vol 52, no 2, Summer 2005, U.S. Institute of Navigation, Fairfax VA, pp. 49-60.

Gernot, C., K. O'Keefe & G. Lachapelle (2011) "Assessing Three New Combined GPS L1 / L2C Acquisition Methods." *IEEE Transactions of Aerospace and Electronic Systems* 47(3): 2239 – 2247.

Gillespie, Thomas, *Fundamentals of Vehicle Dynamics*, Society of Automotive Engineers, Warrendale, PA, 1992. Gillespie, Thomas, Fundamentals of Vehicle Dynamics, Society of Automotive Engineers, Warrendale, PA, 1992.

Humphreys, T., M. Psiaki, P. Kintner, B. Ledvina (2005) "GPS Carrier Tracking Loop Performance in the Presence of Ionospheric Scintillations," in *Proceedings of ION GNSS 2005*, 13-16, Sept., Long Beach CA, pp. 156-167, U.S. Institute of Navigation, Fairfax VA.

Hurd, W.J., J.I.Statman, V.A.Vilnrotter (1987) "High Dynamic GPS Receiver using Maximum Likelihood estimation and frequency tracking," *IEEE Transaction on Aerospace and Electronic Systems,* Volume AES-23, Issue 4, pp. 425-437.

Jekeli, Christopher (2001) *Inertial Navigation Systems with Geodetic Applications*, Walter de Gruyter.

Jovancevic, A., A. Brown, S. Ganguly, J. Noronha and B. Sirpatil (2004) Ultra Tight Coupling Implementation Using Real Time Software Receiver, ION GNSS 2004, Long Beach, CA, Institute of Navigation, 1575-1586.

Kazemi, P. (2010) "Development of New Filter and Tracking Schemes for Weak GPS Signal Tracking," PhD Thesis, published as Report No. 20309, Department of Geomatics Engineering, The University of Calgary, Canada.

Kazuyuki, K., M. Fumio and W. Kajiro (1994), "Accurate Navigation via Differential GPS and Vehicle Local Sensors," in *Proceedings of the 1994 IEEE International Conference on Multisensor Fusion and Integration for Intelligent Systems* (MFI'94) La Vega, NV.

Kim, H.S., S.C. Bu, G.I. Jee and C.G. Park (2003) "An Ultra-Tightly Coupled GPS/INS Integration Using Federated Filtering," ION GPS/GNSS 2003, Portland, OR, Institute of Navigation, 2878-2885.

Kiesel, S., M. M. Held, G. F. Trommer (2007) “Realization of a Deeply Coupled GPS/INS Navigation System Based on INS-VDLL Integration,” in *Proceedings of ION NTM 2007*, 22-24 January, San Diego CA, pp.522-531, U.S. Institute of Navigation, Fairfax VA.

Kubo, J., T. Kindo, A. Ito and S. Sugimoto (1999) “DGPS/INS/Wheel Sensor Integration for High Accuracy Land-Vehicle Positioning” in *Proceedings of ION GPS 1999*, September, Nashville, TN, pp. 555-564.

Lahrech, A., C.Boucher and J.C.Noyer (2004), “Fusion of GPS and odometer measurements for map-based vehicle navigation”, in *2004 IEEE International Conference on Industrial Technology (IClT),* 944- 948 Vol. 2 .

Landis, D., T. Thorvaldsen, B. Fink, P. Sherman, S. Holmes (2006) “A Deeply Integration Estimator for Urban Ground Navigation” in *Proceedings of IEEE/ION PLANS 2006,*25-27 April, San Diego CA, pp. 927-932.

Lashley (2006), “Kalman filter tracking algorithm for software GPS receiver”, M.Sc. thesis, Department of Electrical and Computer Engineering, Auburn University, USA .

Lashley, M. and D. M. Bevly (2009) “Vector Delay/Frequency Lock Loop Implementation and Analysis”, *in Proceedings of ION NTM 2009*.

Lashley and D. M. Bevly (2006), "Analysis of Discriminator Based Vector Tracking Algorithms," in *ION National Technical Meeting*, San Diego, CA, 2007, pp. 570-576.

Li, D., J. Wang (2006) “System Design and Performance Analysis of Extended Kalman Filter-Based Ultra-Tight GPS/INS Integration,” in *Proceedings of IEEE/ION PLANS 2006*, 25-27 April, San Diego CA, pp.291-299.

Li, T., M. Petovello, G. Lachapelle and C. Basnayake (2010) “Ultra-tightly Coupled GPS/Vehicle Sensor Integration for Land Vehicle Navigation,” *NAVIGATION*, 57, 4, 263-274.

Li, T. (2009) *Use of Wheel Sensors to Enhance a Reduced IMU Ultra-Tight GNSS Receiver*, MSc Thesis, published as Report No. 20300, Department of Geomatics Engineering, The University of Calgary, Canada.

Li, T., M.G. Petovello, G. Lachapelle and C. Basnayake (2009) “Performance Evaluation of Ultra-tight Integration of GPS/Vehicle Sensors for Land Vehicle Navigation,” in *Proceedings of GNSS09* (Savannah, GA, 22-25 Sep, Session D2), The Institute of Navigation, 12 pp.

Lin, T., C. O'Driscoll and G. Lachapelle (2011a) "Development of a Context-Aware Vector Based High-Sensitivity GNSS Software Receiver," *Proceedings of International Technical Meeting*, Institute of Navigation, San Diego, 24-26 January, 13 pages.

Lin, T., J. Curran, C. O'Driscoll and G. Lachapelle (2011b) "Implementation of a Navigation Domain GNSS Signal Tracking Loop," *Proceedings of GNSS11* (Portland, OR, 20-23 Sep), The Institute of Navigation, 8 pages.

MacGougan G. (2003), "High Sensitivity GPS Performance Analysis in Degraded Signal Environments", M.Sc. thesis, UCGE Report No. 20176.

Niedermeier, H., H.Beckmann, B. Eissfeller and O.Pozzobon (2010), "Detection and Mitigation of GNSS Deception by Combination of Odometric Dead Reckoning and GNSS Observations for Vehicles", in *23rd International Technical Meeting of the Satellite Division of The Institute of Navigation*, Portland, OR, September 21-24, 2010.

Niu, X., Nassar, S. and El-Sheimy, N. (2007a) "An Accurate Land-Vehicle MEMS IMU/GPS Navigation System Using 3D Auxiliary Velocity Updates," in *Journal of the Institute of Navigation*, USA., vol 54, no 3, pp.177-188.

Niu, X., S. Nasser, C. Goodall, and N. El-Sheimy (2007b) "A Universal Approach for Processing any MEMS Inertial Sensor Configuration for Land-Vehicle Navigation," in *The Journal of Navigation*, vol 60, no 2, The Royal Institute of Navigation, pp.233-245.

O'Driscoll,C, M.G. Petovello and G.Lachapelle (2010) "Choosing the Coherent Integration Time for Kalman Filter Based Carrier Phase Tracking of GNSS Signals", internal communication.

Ohlmeyer, E. J. (2006) "Analysis of an Ultra-Tight Coupled GPS/INS System in Jamming," in *Proceedings of IEEE/ION PLANS 2006,* 25-27 April, San Diego CA, pp. 44-53

Pany, T., J. Winkel, B. Riedl, M. Restle, T. Worz, R. Schweikert, H. Niedermeier, G. Ameres, B. Eissfeller, S. Lagrasta and G. Lopez-Risueno (2009) "Performance of a Partially Coherent Ultra-Tightly Coupled GNSS/INS Pedestrian Navigation System Enabling Coherent Integration Times of Several Seconds to Track GNSS Signals Down to 1.5 dBHz,"*in Proceedings of GNSS09*, The Institute of Navigation, 16 pages.

Pany, T. and B. Eissfeller (2006) "Use of a Vector Delay Lock Loop Receiver for GNSS Signal Power Analysis in Bad Signal Conditions", *in ION Annual Meeting/IEEE PLANS*, San Diego, CA.

Pany, T., R. Kaniuth, and B. Eissfeller (2005) "Deep Integration of Navigation Solution and Signal Processing," in *Proceedings of ION GNSS 2005*, 13-16 Sept., Long Beach CA, pp. 1095-1102, U.S. Institute of Navigation, Fairfax VA.

Petovello, M.G., C. O'Driscoll, G. Lachapelle, D. Borio and H. Murtaza (2009) "Architecture and Benefits of an Advanced GNSS Software Receiver." *Positioning*, 1, 1, pp. 66-78.

Petovello, M., C. O'Driscoll and G. Lachapelle (2008a) Weak Signal Carrier Tracking of Weak Using Using Coherent Integration with an Ultra-Tight GNSS/IMU Receiver. Proceedings of European Navigation Conference (Toulouse, 23-25 April), 11 pages.

Petovello, M., C. O'Driscoll and G. Lachapelle (2008b) "Carrier Phase Tracking of Weak Signals Using Different Receiver Architectures," Proceedings of ION NTM08 (San Diego, 28-30 Jan, Session A4). The Institute of Navigation,11 pages.

Petovello, M., and G. Lachapelle (2006) "Comparison of Vector-Based Software Receiver Implementations with Application to Ultra-Tight GPS/INS Integration," in *Proceedings of ION GNSS 2006,* 26-29 Sept., Fort Worth TX, pp.2977-2989, U.S. Institute of Navigation, Fairfax VA.

Petovello, M. (2003) *Real-Time Integration of a Tactical-Grade IMU and GPS for High-Accuracy Position and Navigation*, Ph. D. Dissertation, Department of Geomatics Engineering, University of Calgary, Canada (Available at http://plan.geomatics.ucalgary.ca)

Psiaki, M., H. Jung (2002) "Extended Kalman Filter Methods for Tracking Weak GPS Signals," in Proceedings of ION GPS 2002, 24-27 Sept., Portland OR, pp. 2539-2553, U.S. Institute of Navigation, Fairfax VA.

Psiaki, M. (2001) "Smoother-Based GPS Signal Tracking in a Software Receiver," in *Proceedings of ION GPS 2001,* 11-14 Sept., Salt Lake City UT, pp. 2900-2913, U.S. Institute of Navigation, Fairfax VA.

Rogers R.M. (2007) *Applied Mathematics in Integrated Navigation Systems*. American Institute of Aeronautics and Astronautics, Inc., Reston, VA, USA

Sasse, A., T. Nothdurft and P. Hecker (2009), "Robust Car Localization for an Autonomous Vehicle in Urban Environments", *in 22nd International Meeting of the Satellite Division of The Institute of Navigation*, Savannah, GA, September 22-25, 2009.

Shanmugam, S. (2008) "New Enhanced Sensitivity Detection Techniques for GPS L1 C/A and Modernized Signal Acquisition", PhD Thesis, published as Report No. 20264, Department of Geomatics Engineering, The University of Calgary.

Soloviev, A, J. Dickman (2011) "Extending GPS Carrier Phase Availablity Indoors with a Deeply Integrated Receiver Architecture," *Wireless Communications, IEEE, 2011,* Vol 18, Issue 2, pp. 36-44

Soloviev, A., D. Bruckner, F. van Graas and L. Marti (2007) "Assessment of GPS Signal Quality in Urban Environments Using Deeply Integrated GPS/IMU," in *Proceedings of ION NTM 2007*, 22-24 January, San Diego, CA, pp. 815-828, U.S. Institute of Navigation, Fairfax VA

Soloviev, A., F. van Graas and S. Gunawardena (2004a) "Implementation of Deeply Integrated GPS/Low-Cost IMU for Reacquisition and Tracking of Low CNR GPS Signals," in *Proceedings of ION NTM* 2004, 26-28 January, San Diego CA, pp. 923-935, U.S. Institute of Navigation, Fairfax VA.

Soloviev, A., S. Gunawardena and F. van Graas (2004b) "Deeply Integrated GPS/Low-Cost IMU for Low CNR Signal Processing: Flight Test Results and Real Time Implementation," in *Proceedings of ION GNSS 2004*, 21-24 Sept., Long Beach CA, pp.1598-1608, U.S. Institute of Navigation, Fairfax VA.

Somieski, A., C. Hollenstein, E. Favey and C. Schmid, u-blox AG, Switzerland (2010), "Low-Cost Sensor Fusion Dead Reckoning using a Single-Frequency GNSS Receiver Combined with Gyroscope and Wheel Tick Measurements", 23rd *International Technical Meeting of the Satellite Division of The Institute of Navigation*, Portland, OR, September 21-24, 2010.

Spilker, Jr., J. J. (1996). Fundamentals of Signal Tracking Theory. In Parkinson, B.W., editor, Global Positioning System: Theory and Applications, Volume 1, volume 163 of Progress in Astronautics and Aeronautics, chapter 4. American Institute of Aeronautics and Astronautics, Washington, DC.

Stephen, J. and G. Lachapelle. (2001), "Development and Testing of a GPS-Augmented Multi-Sensor Vehicle Navigation System", *The Journal of Navigation* (2001), 54: 297-319, 2001, The Royal Institute of Navigation, DOI: 10.1017/S0373463301001357.

Stephens, S.A. and J.B. Thomas (1995) "Controlled-Root Formulation for Digital Phase-Locked Loops", in *IEEE Transactions on Aerospace and Electronic Systems*, Vol.31, No. 1 pp 78-95.

Sun, D., M.G. Petovello and M.E. Cannon (2009) "Use of a Reduced IMU to Aid a GPS Receiver with Adaptive Tracking Loops for Land Vehicle Navigation," *GPS Solutions*, 15(4): 403-414.

Sun, D., M. Petovello and M.E. Cannon (2008) "GPS/Reduced IMU with a Local Terrain Predictor in Land Vehicle Navigation," in International Journal of Navigation and Observation, Volume 2008

Tseng, H.E., X. Li and H. Davor (2007), "Estimation of land vehicle roll and pitch angles," *Vehicle System Dynamics*, Volume 45, Issue 5, 2007, DOI: 10.1080/00423110601169713

Umar, I., B. K. Tashfeen, F. O. Aime, and N. Aboelmagd (2009), "Experimental Results on an Integrated GPS andMultisensor Systemfor Land Vehicle Positioning", *International Journal of Navigation and Observation,* Volume 2009, Article ID 765010, 18 pages, doi:10.1155/2009/765010.

Umar, I., F. O. Aime and N. Aboelmagd, (2008), "An Integrated Reduced Inertial Sensor System RISS / GPS for Land Vehicle", *in Position, Location and Navigation Symposium, 2008 IEEE/ION*, 5-8 May 2008 On page(s): 1014 – 1021, Monterey, CA.

Van Graas, F., A. Soloviev, M. U. Haag, S. Gunawardena, M. Braasch (2005) "Comparison of Two Approaches for GNSS Receiver Algorithms: Batch Processing and Sequential Processing Considerations",*in ION GNSS 18th International Technical Meeting of the Satellite Division*, 13-16 September 2005, Long Beach, CA.

Ward, P.W., J.W. Betz and C.J. Hegarty (2006), "Satellite signal acquisition, tracking, and data demodulation," in *Understanding GPS* (E. D. Kaplan and C. J. Hegarty, eds.)

Wong, J.Y. (1993), *Theory of Ground Vehicles*, Wiley-Interscience Publication, New York, 1993.

Xie, P. and M.G. Petovello (2011), "Multipath Signal Assessment in the High Sensitivity Receivers for Vehicular Applications," *Proceedings of ION GNSS 2011*, The Institute of Navigation, 13 pages.

Ziedan, N.I. and J.L. Garrison (2004) Extended Kalman Filter-Based Tracking of Weak GPS Signals under High Dynamic Conditions, ION GNSS 2004, Long Beach, CA, Institute of Navigation, 20-31.

APPENDIX A: FRAME DEFINATION AND TRANSFORMATION

The following frames and the transformations that are used in this thesis are defined as follows.

Inertial Frame (i-frame)

Inertial frame is the frame in which Newton's first law of motion is valid. Since an ideal definition of the inertial frame is not practical, a quasi-inertial frame which is non-rotating and approximately non-accelerating is often used (Petovello 2003, Jekeli 2001). The inertial frame is defined as follows:

Origin : Earth's centre of mass

Z-Axis : Parallel to the spin axis of the Earth

X-Axis : Pointing towards the mean vernal equinox

Y-Axis : Orthogonal to X and Z completing a right-handed system

Earth Centred Earth Fixed Frame (ECEF or e-frame)

The Earth-fixed frame is defined as follows:

Origin : Earth's centre of mass

Z-Axis : Parallel to the Earth's mean spin axis

X-Axis : Pointing towards the mean meridian of Greenwich

Y-Axis : Orthogonal to the X and Z axes to complete a right-handed frame

Local Level Frame (LLF or n-frame)

The Local level frame is a local geodetic frame defined as follows:

Origin : Coinciding with sensor/body frame

Z-Axis : Orthogonal to the reference ellipsoid pointing Up

X-Axis : Pointing towards geodetic East

Y-Axis : Pointing toward geodetic North

Body Frame (b-frame)

The body frame represents the orientation of the IMU axes. For strapdown inertial systems, as used here, the IMU is rigidly mounted to the platform.

Origin : Centre of IMU

X-Axis : Pointing towards the right of the platform

Y-Axis : Pointing towards the front of the platform

Z-Axis : Orthogonal to the X and Y axes to complete a right-handed frame

Vehicle Frame (v-frame)

The vehicle frame (v-frame) is an orthogonal axis set that is aligned with the roll, pitch and heading axes of a vehicle. This frame is used because sometimes the IMU's body frame is not parallel to the v-frame, for example, because of mounting errors. The frame is defined as follows:

Origin : Mass centre of the vehicle

X-Axis : Pointing towards the right of the vehicle

Y-Axis : Pointing towards the front of the vehicle

Z-Axis : Orthogonal to the X and Y axes to complete a right-handed system

Horizontal Frame (h-frame)

Origin : Coinciding with sensor frame

Z-Axis : Orthogonal to reference ellipsoid pointing Up

X-Axis : Pointing to X –Axis after rotating Z-Axis of n-frame by an azimuth angle

Y-Axis : Pointing to X –Axis after rotating Z-Axis of n-frame by an azimuth angle

The transformation between e-frame and n-frame can be performed by two consecutive rotations around the X and Z axes of the ECEF frame, and is given by (Godha 2006) as

$$R_e^n = R_1(\frac{\pi}{2} - \varphi)R_3(\frac{\pi}{2} + \lambda) \qquad \text{A.1}$$

where

φ is the latitude;

λ is the longitude;

R_e^l is the rotation matrix from e-frame to l-frame;

R_1, R_3 are the rotation matrixes about x and y axis respectively.

The transformation between b-frame and n-frame can be performed by three consecutive rotations around the Y, X and Z axes, and is given by (Godha 2006)

$$R_b^n = R_3(\psi)R_1(-\theta)R_2(-\phi) = R_h^n R_b^h \qquad \text{A.2}$$

where

ψ is the azimuth angle;

θ is the pitch angle;

ϕ is the roll angle;

R_b^n is the rotation matrix from the b-frame to the n-frame.

It is noted that, usually the body frame is aligned with the vehicle frame or it can be rotated to the vehicle frame. Thus the azimuth, pitch and roll angles at this time represent the orientation of the vehicle. It is noted that the horizontal frame (h-frame) is a local level frame (n-frame) that rotates with the heading angle.

The transformation between the b-frame and e-frame can be obtained by consecutive rotations as

$$R_b^e = R_n^e R_b^n = (R_e^n)^T R_b^n \quad \text{A.3}$$

APPENDIX B: GAUSS-MARKOV PROCESS

The first order Gauss-Markov process for a random variable can be presented by

$$\dot{X} = -\alpha_X X + w_X \tag{B.1}$$

where, α_x is the reciprocal of the correlation time of the state "X", w_X is the driving noise of a Gauss Markov process with spectral density q_X, which can be determined as

$$q_X = \sqrt{2\sigma_X^2 \alpha_X} \tag{B.2}$$

where σ_X is the temporal standard deviation of the process.